INFORMATION TO USERS

This manuscript has been reproduced from the microfilm master. UMI films the text directly from the original or copy submitted. Thus, some thesis and dissertation copies are in typewriter face, while others may be from any type of computer printer.

The quality of this reproduction is dependent upon the quality of the copy submitted. Broken or indistinct print, colored or poor quality illustrations and photographs, print bleedthrough, substandard margins, and improper alignment can adversely affect reproduction.

In the unlikely event that the author did not send UMI a complete manuscript and there are missing pages, these will be noted. Also, if unauthorized copyright material had to be removed, a note will indicate the deletion.

Oversize materials (e.g., maps, drawings, charts) are reproduced by sectioning the original, beginning at the upper left-hand corner and continuing from left to right in equal sections with small overlaps. Each original is also photographed in one exposure and is included in reduced form at the back of the book.

Photographs included in the original manuscript have been reproduced xerographically in this copy. Higher quality 6" x 9" black and white photographic prints are available for any photographs or illustrations appearing in this copy for an additional charge. Contact UMI directly to order.

UMI

A Bell & Howell Information Company
300 North Zeeb Road, Ann Arbor MI 48106-1346 USA
313/761-4700 800/521-0600

Université d'Ottawa · University of Ottawa

A FUNDAMENTAL STUDY OF STARLING FLOW AND PROTEIN REDISTRIBUTION WITHIN A CELL-FREE RECTILINEAR MEMBRANE FLOW DEVICE

RICHARD POMALIS

APRIL 28, 1997

A thesis submitted to the School of Graduate Studies and Research in partial fulfillment of the requirements for the degree of **Master of Applied Science** in the Department of Chemical Engineering, University of Ottawa.

National Library of Canada Abstract

Please note that a CD ROM is provided with the bound version of this thesis. A CD ROM can be obtained by contacting the author.

Richard Pomalis
726-9368
947-2469

ABSTRACT

The efficiency of hollow fiber bioreactors depends on design and operating parameters. Protein redistribution, a consequence of Starling flow, can result in poor cell distribution and reductions in performance. Hydrodynamic investigations require consideration of design and sampling. A simplified rectilinear flow system was developed and modeled. A 2D (SIMPLER) model incorporating gravity, and correlations for density, viscosity, diffusivities, and osmotic pressures was coded in FORTRAN 77. Experiments with bovine serum albumin (BSA) and a cellulose acetate membrane were carried out to validate the model. Further validation was obtained with a 1D simulator. Simulations show the effects of run duration, initial BSA concentration, channel velocity, and Dextran 70 loading on BSA polarization. The results indicate noticeable BSA polarization only in long duration runs, BSA redistribution in the transverse direction, and the importance of buoyancy. Simulations with fluid flowing against gravity suggest that this orientation can be used to eliminate protein polarization.

ABSTRACT

Hollow fiber bioreactors (HFBRs) have been used for cell culture and biomolecule production. The functionality and efficiency of these units are dependent on their design as well as operating parameters. Protein redistribution within the reactor, a direct consequence of Starling flow, is particularly problematic. Protein polarization can result in poor cell distribution and subsequent reductions in bioreactor performance. However, investigation of the effects of bioreactor hydrodynamics requires that design and sampling considerations be taken into account. The impact of fiber-fiber interactions and header design is difficult to model and to measure accurately. Consequently, in this study a simplified rectilinear flow system was developed and modeled.

A two-dimensional control volume model using a modified form of S. V. Patankar's SIMPLER algorithm was constructed and coded in FORTRAN 77. The model allows for the presence of multiple solutes and incorporates adaptive time stepping, gravity, and empirical correlations for density, viscosity, diffusivities, and osmotic pressures.

A rectilinear flow cell device was also redesigned and rebuilt, and several experiments with bovine serum albumin (BSA) and a cellulose acetate membrane were carried out in an effort to validate the numerical model. Additional validation of the two-dimensional (2D) model and its simulator was obtained through comparison against a simulator based on a one-dimensional (1D) model. Experimental and numerical results demonstrate that noticeable BSA polarization in the existing system occurs only in long duration runs (7 days). To allow for more practical run times, it is recommended that either the lower channel height be reduced or the flow rates be increased, and that a more permeable membrane be used in the future.

Additional numerical simulations assuming a higher fluid flow rate through the lower channel and transport properties characteristic of a polysulfone membrane were obtained to show the effects of run duration, initial BSA concentration, average lower channel velocity, and Dextran 70 loading on BSA polarization. The results indicate that, along with longitudinal polarization, significant BSA redistribution occurs in the transverse direction, and that concentration-dependent buoyancy effects may also be significant. Preliminary simulations with the lower channel fluid flowing against gravity suggest that this flow cell orientation can be used to effectively eliminate protein polarization. Furthermore, model studies of this sort can be used to develop strategies for reducing Starling flow and protein polarization through judicious selection of operating parameters and conditions.

RESUME

Les bioréacteurs à fibres creux sont souvent utilisés lors de la production de biomolécules et de culture cellulaires. Leurs fonctionnement et efficacités dépendent grandement de leurs conceptions et des conditions opératoires. La redistribution des protéines à l'intérieur du réacteur, un résultat de la recirculation Starling, est particulièrement problématique. La polarisation des protéines peut entraîner une distribution cellulaire inefficace, réduisant la performance du réacteur. Afin d'étudier le comportement hydrodynamique d'un bioréacteur, if faut tenir compte de la fabrication de l'unité et de l'échantillonnage. L'interaction entre les fibres adjacentes ainsi que l'impact de l'entrée du réacteur sont difficiles à prédire et mesurer. Dans le but d'éliminer ces influences, une cellule rectangulaire a été fabriquée.

Une analyse numérique bi-dimensionnelle a été appliquée au système. Le model est dérivé de la méthode à volume discret SIMPLER développé par S. V. Patankar et l'algorithme a été écrit en FORTRAN 77. Le modèle peut prédire la distribution de plusieurs composés et incorpore l'effet de la gravité, des pas temporels auto-ajustables, ainsi que des corrélations empiriques pour la densité, viscosité, les diffusivités et les pressions osmotiques.

Une cellule rectangulaire a été redessinée et reconstruite. Plusieurs expériences mesurant la distribution de concentration d'albumine bovine, retenue par une membrane d'acétate de cellulose, ont été effectuées afin de vérifier les résultats de l'analyse mathématique. Les résultats du model ont aussi été comparés à ceux d'un model uni-dimensionel qui avait préalablement été développé. Les résultats numériques et expérimentaux démontrent une polarisation de l'albumine seulement après une longue durée (7 jours). Afin de réduire cette durée, il est recommendé de réduire la hauteur du compartiment inférieur, ou d'augmenter le débit. Une membrane plus perméable devrait aussi être utilisée.

Des analyses numériques à haut débit, à travers le compartiment inférieur, en présence d'une membrane polysulfonique ont démontré l'effet de la durée de l'expérience, de la concentration initiale de l'albumine, de la vitesse moyenne dans le compartiment inférieur et de la présence du Dextran 70, sur la polarisation de l'albumine. Les résultats indiquent qu'en plus d'une polarisation longitudinale, une redistribution transversale de l'albumine est aussi présente. Les résultats indiquent aussi que la flottabilité semble jouer un rôle important et qu'elle dépend de la concentration d'albumine. Les études préliminaires semblent aussi indiquer que la polarisation peut-être éliminée en obligeant le liquide dans le compartiment inférieur à voyager contre la gravité. En révélant des conditions d'opérations optimales, des analyses mathématiques de ce genre peuvent s'avérer très utiles lorsqu'il est temps de développer des stratégies qui ont pour but d'éliminer la polarisation des protéines.

ACKNOWLEDGEMENTS

This work was sponsored by the Natural Sciences and Engineering Research Council of Canada and the University of Ottawa. I am grateful to Dr. D.G. Taylor for assistance with the experimental and modeling work. Extensive technical help was provided by Dr. A. Y. Tremblay, Mr. G. Nina, Mr. L. Tremblay, and Mr. F. Ziroldo. Mr. K. Lacki's assistance with Millennium software and the HPLC system is also appreciated. In addition, I wish to thank Mr. D. F. Boukouris and Mr. M. Paris for useful and often entertaining discourse, as well as confirmatory numerical data. This thesis is dedicated to my wife, Joanne.

NOMENCLATURE

Notation

a	discretization equation coefficient, g/s
b	discretization equation term
A_p	chromatogram peak area, μV·s
$A_{i,1}$	first virial coefficient for species i (osmotic pressure equation)
$A_{i,2}$	second virial coefficient for species i (osmotic pressure equation), ml/g
$A_{i,3}$	third virial coefficient for species i (osmotic pressure equation), ml^2/g^2
$A(\lvert P\rvert)$	interpolation function
C	concentration, g/ml
D	species diffusivity, cm^2/s, or diffusive conductance (numerical procedure)
f	weighting factor
F	mass flow rate through control volume face, g/s
g	acceleration due to gravity, cm/s^2
H_m	membrane thickness, cm
H	channel height, cm
J	flux component
J	total diffusion flux, $g \cdot cm^{-2} \cdot s^{-1}$
L_E	entrance or exit length, cm
L_C	channel length, cm
L_p	hydrodynamic membrane permeability, cm
m	mass fraction
M	molecular weight, Da
n	number of species
N	number of nodes

p	hydrostatic pressure, dyne/cm^2
$\bar{p}$	cross-cut averaged pressure, dyne/cm^2
Δp	transmembrane pressure drop, dyne/cm^2
P	Peclet number
Q	volumetric flow rate, ml/s
R_i	rate of generation of species i per unit volume, g·cm^{-3}·s^{-1}
$\Re$	universal gas constant, g·cm^2/(mol·K·s^{-2})
S	total source term
S_C	linearized source term component
S_P	linearized source term component coefficient
t	time, s
Δt	time step, s
T	Temperature, K or °C as defined
u	x-velocity component, cm/s
$\bar{u}$	average x-velocity, cm/s
v	y-velocity component, cm/s
v_m	membrane fluid velocity, cm/s
$\bar{v}$	total velocity vector, cm/s
V	additional viscous contributions, g·cm^{-2}·s^{-2}
w	z-velocity component, cm/s
W	channel width, cm
x	longitudinal distance, cm
δx	x-direction distance between nodes, cm
Δx	control volume width, cm
y	transverse distance, cm
δy	y-direction distance between nodes, cm
Δy	control volume height, cm
z	cross-cut distance, cm

Greek Letters

$\alpha, \alpha', \alpha''$	curve-fitting coefficients
β, β', β''	curve-fitting coefficients
$\gamma, \gamma', \gamma''$	curve-fitting coefficients
$\delta, \delta', \delta''$	curve-fitting coefficients
ε	convergence tolerance
ζ	geometric factor for a rectangular duct
Γ	diffusion coefficient (numerical procedure)
θ	angle above the horizontal, rad
κ	Darcy permeability, cm^2
μ	fluid viscosity, poise
Π	osmotic pressure, $dyne/cm^2$
ρ	fluid density, g/ml
σ	relaxation factor
ϕ	an arbitrary dependent variable

Subscripts

0	initial value
e	east face of control volume
E	east node
i	species
L	lower channel
m	membrane
n	north face of control volume
N	north node
nb	neighbouring
P	control volume node
s	south face of control volume
S	south node
U	upper channel
w	west face of control volume
W	west node
x	*x*-direction
y	*y*-direction
z	*z*-direction

Superscripts

0	value at beginning of time step
'	correction field
*	imperfect 'starred' field
#	'pseudo' field

CONTENTS

LIST OF TABLES

LIST OF FIGURES

Chapter 1

Introduction

1.1 Bioprocessing and Membrane Technology

A wide range of cell lines and biomolecules are routinely produced through synthetic chemical and bioprocessing methods. The cell types and viruses, as well as complex plant and animal proteins, hormones and antibodies so derived are used in fields ranging from diagnostics, prevention and treatment of diseases to fermentation [1, 2, 3, 4]. The traditional sources of mammalian proteins have been blood donor plasma, cadavers, and the placenta. Because these sources are limited and prone to viral contamination, large scale industrial production of biomolecules is highly desirable [5]. Furthermore, *in vitro* cell culture offers an attractive alternative to animal experiments [6].

Bioprocessing affords certain advantages over synthetic processing methods. Traditional catalytic methods typically employ high pressure and temperature reaction conditions. Biological processes require much milder conditions and, consequently, can have lower associated costs. Recombinant DNA technology can make bioprocessing more competitive by increasing product yields through the use of promoters and by reducing recovery costs through selective biomolecule excretion from microorganisms [1].

Bioprocessing methods based on membrane technologies can be particularly advantageous for a number of reasons. Firstly, membrane systems provide a barrier between the flowing medium and cells, thereby reducing contamination and the damaging effects of fluid shear stress on cell membranes. Secondly, the large surface area to volume ratios of these systems lead to high cell densities, product concentrations, and productivities [2, 7, 8]. In fact, tissue-like cell densities have been reported for hollow fiber bioreactor (HFBR) units [9]. Lastly, membrane systems can be operated in continuous or recycle modes. This capability, combined with the separation of the catalyst and product, leads to reduced product purification costs [2].

Of course, a number of difficulties are associated with bioprocessing. Inherent to most bioprocessing methods is the high cost of energy intensive sterilization of the biocatalyst suspension, nutrient feed medium, reactor and transfer equipment. The addition of growth inhibitors such as bacteriostatic agents tends to augment costs [5]. Furthermore, the addition of such compounds may have deleterious effects on the proliferation of desired cells and, ultimately, on reactor productivity [10, 11]. Another issue is the production of metabolic byproducts. Byproduct separation from the desired compound may be difficult and costly. Additionally, the presence of certain byproducts may result in product inhibition and/or reduced cell growth [5].

Other problems encountered in bioprocessing methods are dependent on the reactor design and operating conditions. These are discussed after the following description of one of the more popular reactor designs, the closed shell mode HFBR [7, 12].

1.2 The Hollow Fiber Bioreactor

The typical HFBR configuration (Fig. 1.2.1) is much like that of a shell-and-tube heat exchanger. The reactor consists of hundreds to thousands of hollow fiber membranes arranged in parallel and encased in a cylindrical shell. The semi-permeable membrane fibers are connected to manifolds at either end of the reactor by potting material [13]. Fibers are commonly made of polysulfone, cellulose acetate, or polypropylene, and have inner diameters of approximately 200 μm and lengths ranging from a few centimeters to several meters [5]. During typical closed shell operation, cells are transferred into the extra-capillary space (ECS), the regions surrounding the fibers, while a nutrient solution is fed through the fiber lumens. The nutrients cross the membrane walls and are used by growing cells. Concomitantly, cellular wastes such as CO_2 and lactic acid move from the ECS into fiber lumens where they are swept away. Other wastes which cannot pass through the membrane accumulate in the ECS.

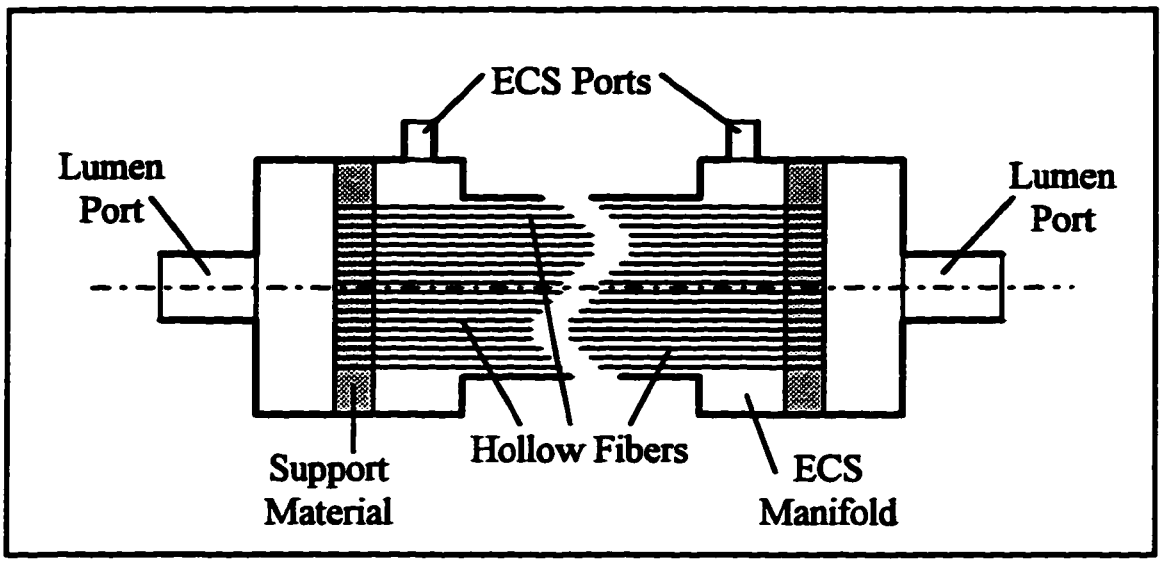

Figure 1.2.1. Schematic diagram of a hollow fiber module.

Hollow fiber reactors are not limited to cell culture and biomolecule production. Open shell operation is employed in the ultrafiltration of macromolecular solutions. Ultrafiltration may be used to concentrate, as in hemoconcentration [14], or to purify solutions [4, 5]. Hollow fiber membranes are also used in several bioartificial organs, currently a field of intense study. The devices cited in literature are the artificial lung [15], kidney [16], pancreas [7, 17, 18, 19, 20], and liver [14, 21, 22, 23, 24, 25].

1.3 Design and Operational Considerations

A number of hollow fiber module design and operational variables can, in practice, be manipulated. These include membrane thickness, permeability and material, fiber geometry and spacing, module geometry, packing density, substrate concentration, feed flow rate, and run time [2, 12]. It is the particular application for which the unit is to be used which dictates the optimum values of these variables. For example, optimum fiber

densities for cell-filled reactors are considerably lower than those for separation applications [12]. The primary focus of this work is the characterization of several of the operational challenges associated with cell cultivation and biomolecule production in closed shell HFBRs.

Suboptimal design and operation of HFBRs can lead to membrane fouling, clogging of fibers, and fiber disruption due to excessive gas production or cell growth [1]. Membrane fouling results in reduced permeability and lower transmembrane mass transfer. Consequently, inhibitory metabolite build-up and reduced nutrient flow can lead to regions of low cell density. Conversely, nonuniform fluid flows in the fibers caused, for example, by poor header design and fiber-fiber interactions, can result in high cell density zones which may restrict nutrient transport and lead to the development of necrotic regions [1]. Another phenomenon giving rise to poor cell distributions is Starling flow, a consequence of the pressure drop associated with the flow of fluid through the fiber lumens.

1.4 Starling Flow and Solute Polarization

Starling flow, described in capillary-tissue systems in 1896 [26], is characterized by the recirculation of fluid within the ECS of hollow fiber bioreactors. It is the lumen pressure drop that generates the secondary flow field in which fluid moves from the upstream end of the reactor towards its downstream regions (Fig. 1.4.1). The presence of fluid recirculation within the ECS has been confirmed experimentally by pressure measurements [27] and magnetic resonance imaging [2].

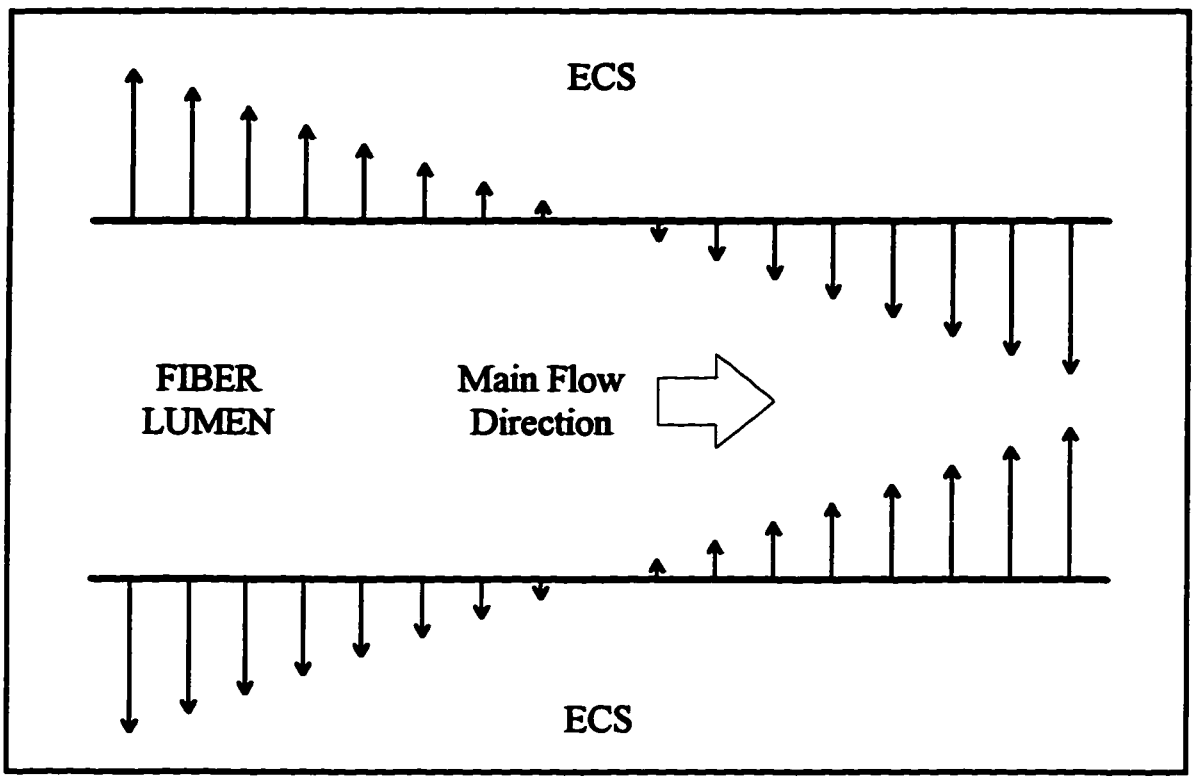

Figure 1.4.1. Schematic diagram of Starling flow in a hollow fiber.

As indicated by their low radial Peclet numbers, the transport of low molecular weight substrates, such as oxygen and glucose, to cells is primarily by means of diffusion within the ECS. On the other hand, convective transport predominates for high molecular weight species: the radial and axial Peclet numbers for bovine serum albumin are typically up to 5 orders of magnitude greater than those of low molecular weight species [5]. The implications of this 'order of magnitude' analysis are profound. It infers that Starling flow should sweep high molecular weight molecules of the ECS downstream. Since the hollow fibers are normally impermeable to such large molecules, these species will accumulate near the downstream end of the HFBR. This phenomenon is termed species concentration redistribution or polarization. It should not, however, be confused with the more established definition of concentration polarization used in the field of membrane

technology: the concentration polarization exists on the side of the membrane with the highest chemical activity and is the gradient between the more concentrated boundary layer and the less concentrated bulk solution [28, 29, 30].

The complexities of modeling the hydrodynamics and solute redistribution in HFBRs are beyond the scope of this work. Instead, a cell-free rectilinear geometry, in which the lower and upper channels are analogous to the fiber lumen and ECS, respectively, is modeled here. Clearly, the findings of such a study are expected to shed light on the effects of similar design and operating variables within HFBRs.

1.5 The Importance of Numerical Modeling

Numerical modeling is routinely used to solve problems in such fields as heat transfer, fluid dynamics, reaction kinetics, and process control. The development of a numerical model tends to lead to a better understanding of the underlying principles of the problem at hand. Complex problems, for which analytical solutions cannot be derived, require the use of computational methods. Traditionally, experimental and empirical approaches have been employed to investigate such problems. This is particularly true of fields like biology. Experimentalists often argue that certain problems are far too complex to be modeled adequately and, hence, models based on simplifications are unlikely to give meaningful results.

Even simple models can yield useful information and can be gradually extended. Under some conditions, a numerical solution which deviates from reality can be much more interesting than one which accurately models the phenomena in question. Imperfect solutions can lead to further problem investigation and characterization and, ultimately, a better grasp of the fundamentals of the problem.

Of course, the intention here is not necessarily to replace experimentation with numerical modeling. Rather, experimentation can be used to validate a model. However, the use of a verified model can curb the costs and time expenditures of subsequent experimentation.

Modeling work can reveal certain details that may otherwise be obscured during experimentation. Additionally, the use of numerical models allows for the investigation of experimental design and operational variables. Lastly, the nature of many problems precludes the use of anything but computational methods in obtaining solutions. For example, computational fluid dynamics is the only viable tool for the design of hypersonic aircraft and spacecraft [31]. The numerical model developed for the rectilinear flow cell predicts that under certain conditions, very small degrees of protein polarization can occur. Furthermore, the model offers insight as to how such phenomena might arise.

1.6 Previous Experimental and Modeling Work

In the past, most of the hydrodynamic models for hollow fiber systems have been based on the Krogh cylinder approximation (see, for example, references [2, 7, 9, 12, 13, 17, 32, 33, 34, 35]). In the Krogh cylinder approach, it is assumed that the flow and solute transport with the HFBR can be analyzed by considering a cylindrical unit consisting of a single hollow fiber and its surrounding fluid annulus. Apelblat *et al.* [32] were amongst the first to use the Krogh cylinder geometry in their theoretical analysis of flow within a permeable thin-walled capillary surrounded by tissue. For HFBR analyses, the mass transport in cell-filled [2, 12, 34] and cell-free [7, 9, 13, 17, 33] reactors has been considered. In most of the cases addressing Starling flow, the ECS velocity field was assumed to be solely due to the lumen hydrostatic pressure gradient. Investigations of the effects of osmotic pressures generated by ECS species on system hydrodynamics have been carried out only recently [9, 13, 35]. The results of these studies confirmed the

experimental findings of Piret and Cooney [3] in which significant downstream polarization of antifibronectin antibody and cells was attributed to Starling flow. Furthermore, it was shown that Starling flow can be strongly influenced by the presence of osmotically active species. Taylor *et al.* [13, 35] have shown that sufficiently high bovine serum albumin concentrations in the ECS can eliminate transmembrane fluid transfer and protein polarization. These results were later confirmed experimentally by Patkar *et al.* [9].

The primary weakness in numerical models based on the Krogh cylinder approximation is that they cannot account for the pressure gradients and interfiber flows that arise from less-than-optimum header design and fluid introduction and removal through the circumferential ECS ports [36]. Additional transverse effects can arise due to the presence of osmotically active species; for example, experimental results have shown that buoyancy-induced movement of polarized protein solutions may occur in HFBRs [3]. Another limitation of the above models is that the expansion of hollow fibers, in both the axial and radial directions, has not been considered. This phenomenon, reported in the literature [9], and can lead to a 'wavy' fiber appearance. The Krogh cylinder approximation cannot be used to adequately model such nonuniform geometries. To deal with these difficulties, a novel approach was recently developed: the porous medium model (PMM) includes all fibers and has a computational domain that corresponds to the dimensions of the entire module [36]. The PMM assumes that the shell and lumen sides are interpenetrating porous regions, each acting as a continuous fluid source or sink. The PMM has generated two-dimensional protein polarization fields which are in good agreement with the results of freeze-sectioning experiments [37]. Lastly, a limitation of all numerical models noted thus far is their failure to include gravity effects.

Modeling of HFBR systems is beyond the scope of this investigation. Rather, a simpler approach is taken. The use of a rectilinear geometry greatly simplifies the development of a numerical model. The main advantage, though, is that the hydrodynamics and solute transport in such a relatively simple system should be readily

characterizable. That is, such phenomena as fiber-fiber interactions will not cloud the interpretation of experimental and numerical results pertaining to protein polarization. Furthermore, the use of rectilinear geometry avoids many of the experimental design and sampling difficulties associated with a cylindrical geometry.

1.7 Scope of the Current Work

The primary objectives of the work conducted are to develop a two-dimensional (2D) numerical model for the hydrodynamics and solute redistribution within a cell-free rectilinear flow cell, and to conduct bovine serum albumin polarization experiments in the device. The model, based on a control volume approach, uses a modified form of S. V. Patankar's SIMPLER algorithm. The model allows for the presence of multiple solutes and incorporates gravity and empirical correlations for density, viscosity, diffusivities, and osmotic pressures. Primary validation of the model is accomplished through comparison of 2D numerical results and experimental data. Additional model verification is obtained by comparison with the results obtained with a simplified 1D model.

In the chapters that follow, the experimental, theoretical, and numerical aspects of the investigation are presented. The effects of several design and operational variables are studied in the context of Starling flow and protein redistribution. The results obtained are discussed subsequently. It is expected that the results obtained here will fundamentally apply to HFBRs.

Chapter 2

Experimental Aspects

The following two sections describe the materials and equipment used to conduct the protein polarization studies. The experimental methodology, meanwhile, is presented in detail in the third section.

2.1 Reagents

Formalin, or 2 % formaldehyde solution, can be used to disinfect flow surfaces. To prepare 1000 ml of a formalin solution, 54 ml of stock (37.1 %) formaldehyde is made up to 1000 ml with deionized 18 MΩ water.

Methanol was the solvent of choice for the initial cleaning of flow cell surfaces. Other solvents, such as ethanol and acetone, should not be used for this purpose as they degrade Plexiglas®.

A 10 % methanol solution was used as the high performance liquid chromatography (HPLC) autosampler syringe rinse. HPLC grade methanol is diluted with deionized water to a final concentration of 10 % by volume.

The HPLC mobile phase was prepared by mixing 700 ml of HPLC grade acetonitrile with 300 ml of deionized water and 1 ml of trifluoroacetic acid.

A stock phosphate buffer, pH 7.4, was prepared by mixing 39.1 ml of 0.1 N sodium hydroxide (NaOH) with 50.0 ml of 0.1 M potassium dihydrogen phosphate (KH_2PO_4) and adding deionized water to make up a final volume of 100 ml.

The stock buffer solution was diluted 100-fold with deionized water. To 1000 ml of this dilute buffer, 1 g of 95 % pure sodium azide (NaN_3) was added to impart anti-bacterial properties. This final mixture is henceforth referred to as the dilute buffer. The viscosity of the dilute buffer was reported to be 8.61×10^{-3} poise [5].

99 % pure lyophilized bovine serum albumin (BSA), prepared by initial fractionation by cold alcohol precipitation, was used in the preparation of the BSA solution. BSA, stored at approximately 4 °C, was dissolved in dilute buffer to the desired concentration. The properties of BSA are given in **Table 2.1.1.**

Table 2.1.1. Properties of bovine serum albumin **[13, 38]**.

Molecular Weight	69000 Da
Diffusivity	7×10^{-7} cm^2/s
Isoelectric Point	5.1
Solubility in Water	0.585 g/ml
Denaturation Temperature	50 to 60 °C

2.2 Equipment

Investigation of protein polarization within a hollow fiber bioreactor (HFBR) requires that several factors be taken into account. These include design and sampling considerations.

The design of an HFBR includes the physical dimensions and configuration of the device. The design has profound consequences on the unit's performance. From a modeling point of view, fiber-fiber interactions and header design are particularly problematic. Cross-flow between neighbouring fibers may be promoted by buoyancy effects **[35]**. Furthermore, local fiber-fiber interactions are likely to differ throughout the device as a consequence of less-than-optimum header design. Uneven flow distribution to individual fibers, alone, is difficult to predict accurately.

Sampling in an HFBR must be carried out in such a manner that it does not interfere with the hydrodynamics of the device. Additionally, sampling must preserve solute or cell distributions throughout the reactor, or at least have a negligible effect. A practical sampling method has been used by several investigators [3, 39]: at the end of each experiment, hollow fiber cartridges are frozen and sectioned. This technique, however, leads to significant sampling error and is costly since cartridges are sacrificed.

2.2.1 Rectilinear Flow Cell

In this simplified study of Starling flow, the complicating issues noted above were eliminated through the use of a rectilinear flow cell. The device, as described by Bhola [5], was redesigned and rebuilt to correct a number of its shortcomings.

The redesigned rectilinear flow cell, mounted on its stand, is shown in **Fig. 2.2.1.1**. The stand permits full motion in three dimensions, facilitating the purging of air from the cell and allowing for experiments to be carried out in any orientation. The main components of the flow cell are the two 66 cm × 10.16 cm × 1.8 cm Plexiglas® plates sandwiched between 0.635 cm thick stainless steel plates; a close-up view of the outlet end is shown in **Fig. 2.2.1.2**. A 60 cm × 10.16 cm × 1.8 cm channel, connected to inlet and outlet ports at the ends, is cut in each of the Plexiglas® plates. Between the Plexiglas® plates is a Parafilm®-sealed, Osmonics SEPA-SG13 cellulose acetate membrane. This polyester-backed membrane has a reported molecular weight cutoff between 1000 and 5000 Da. The whole assembly is held together with 5.715 cm long, 0.635 cm NPT bolts. 25 μl Hamilton syringes, with blunt tips, are inserted through 0.635 cm outer diameter glass capillaries and 0.635 cm diameter gas-tight septa located in the sampling ports. The capillaries protrude above the Plexiglas® surface by about 6×10^{-3} cm and compress the septa, ensuring a tight seal when the top stainless steel plate is bolted on. In **Fig. 2.2.1.3**, a syringe needle is shown inserted into a blue capillary and a red septum. The membrane separates the upper and lower channels, and is bordered by the magenta gasket.

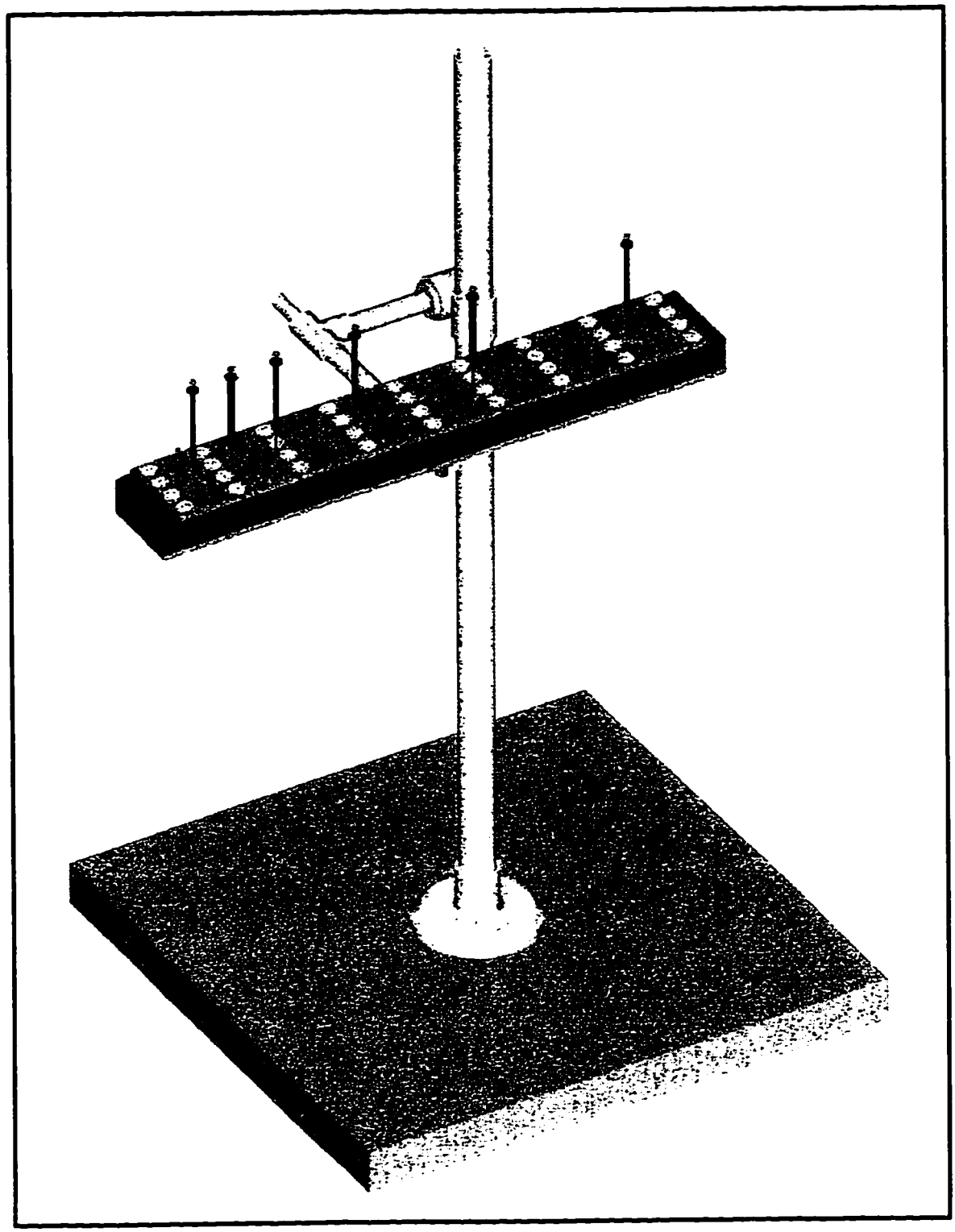

Figure 2.2.1.1. Rectilinear flow cell.

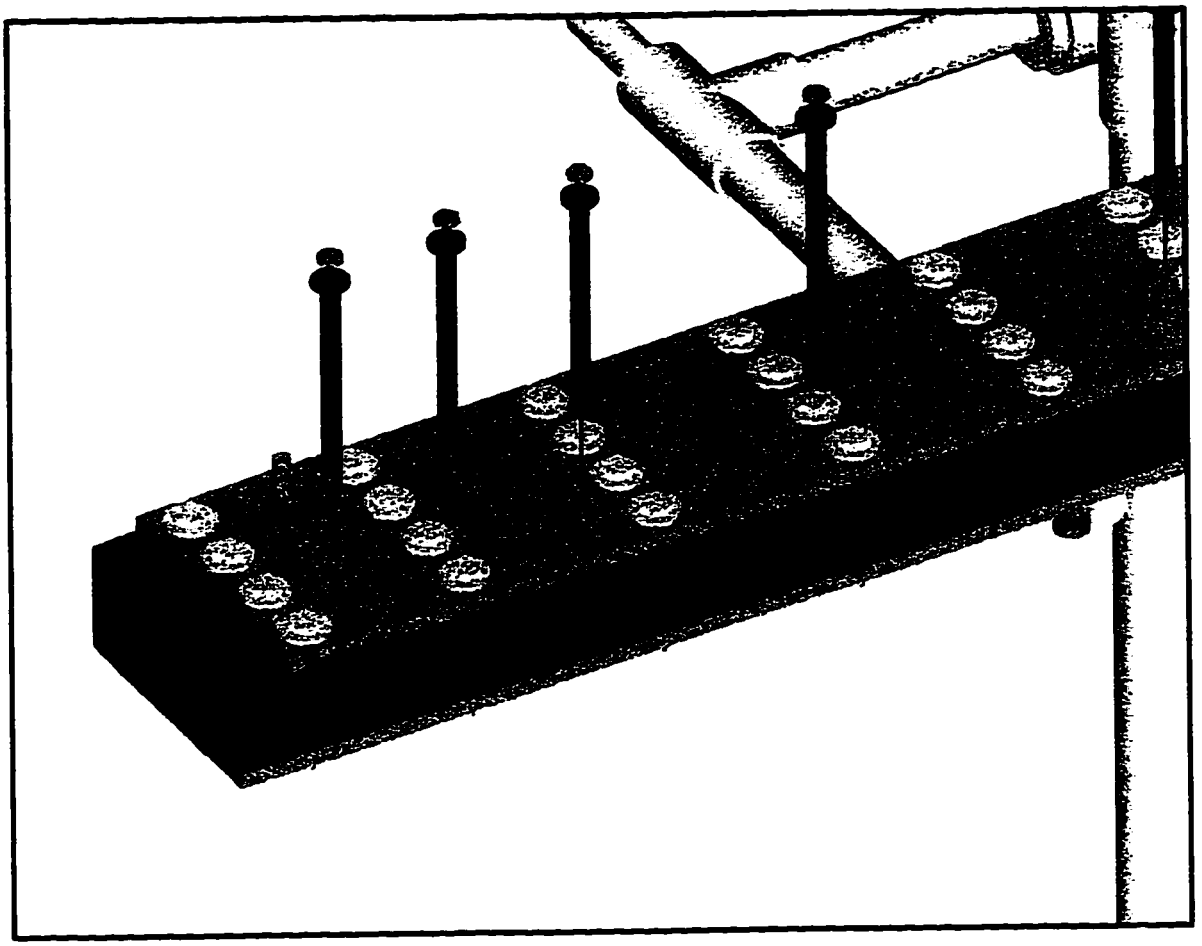

Figure 2.2.1.2. Close-up view of outlet end of rectilinear flow cell.

To minimize the disruption of the concentration field at the end of a trial, only six sampling ports are used. The total sample volume, when six 20 μl samples are withdrawn, represents 3.2 % of the channel volume. Furthermore, the sampling ports are spaced such that they are closest together nearest the outlet end of the flow cell. This ensures better curve-fitting when significant protein polarization occurs because of the non-linear nature of the concentration profile nearest the downstream end. The positions of the sampling ports relative to the inlet end of the channel are given in **Table 2.2.1.1.**

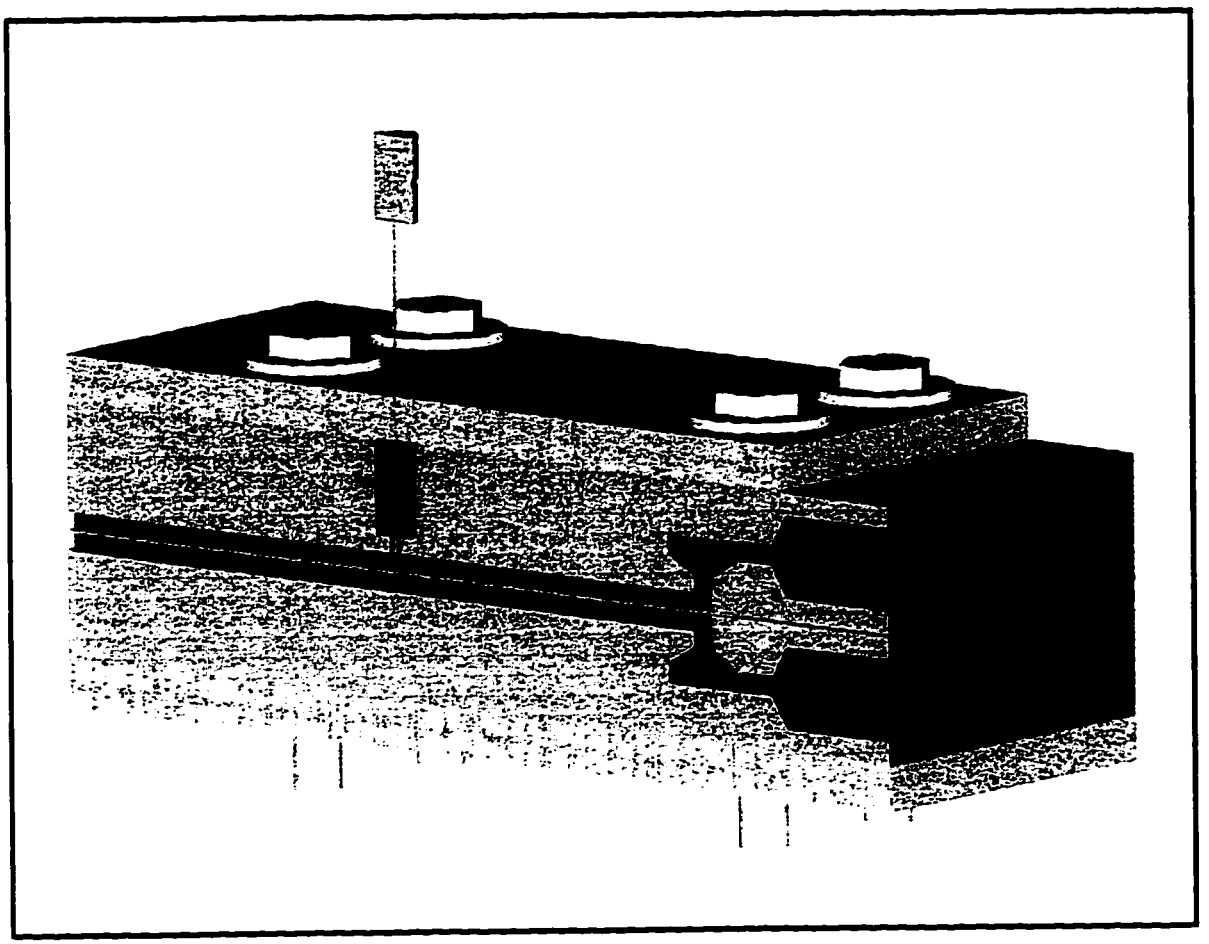

Figure 2.2.1.3. Cross-sectional view of flow cell inlet end.

Table 2.2.1.1. Flow cell sampling port positions.

Sampling Port Number	Position (cm)
1	6.68
2	24.92
3	38.60
4	47.76
5	53.06
6	57.56

2.2.2 Pump

A Pro-Spense® microprocessor controlled pump equipped with a pressure-loaded pump head is used to circulate fluid through the flow cell. This magnetically coupled gear pump has a maximum flow rating of 100 ml/min. The design of the pump head requires that the outlet pressure be greater than that of the inlet. The controller accepts serial (RS-232-C), TTL, and analog inputs allowing for remote pump control, as well as operation of other laboratory devices [40].

2.2.3 Flow Transfer Equipment and Valves

Flow transfer is accomplished through the use of semi-rigid 0.635 cm outer diameter polyethylene tubing and 0.635 cm polypropylene compression fittings. Valves were constructed with 0.635 cm inner diameter Tygon® tubing, copper wire and clamps.

2.2.4 Precision Balance

An Ohaus TP200 balance is used weighing of chemicals as well as for the *in situ* membrane permeability determination. This 200 g capacity balance has a reproducibility of ±0.001 g, and is equipped with a bi-directional RS-232-C interface [41].

2.2.5 Pressure Transducer

A Validyne P305D pressure transducer, also equipped with an RS-232-C interface, is used for the *in situ* membrane permeability determination. The pressure transducer accepts an excitation voltage of 10 to 32 VDC, and has a reproducibility of about ±70 Pa (±0.01 psi).

2.2.6 High Performance Liquid Chromatography System

Protein concentrations are determined using a Waters HPLC system. The main components of the system are a system controller, pump, autosampler, column, differential refractometer, and photodiode array detector (**Fig. 2.2.6.1**). Separations are achieved by

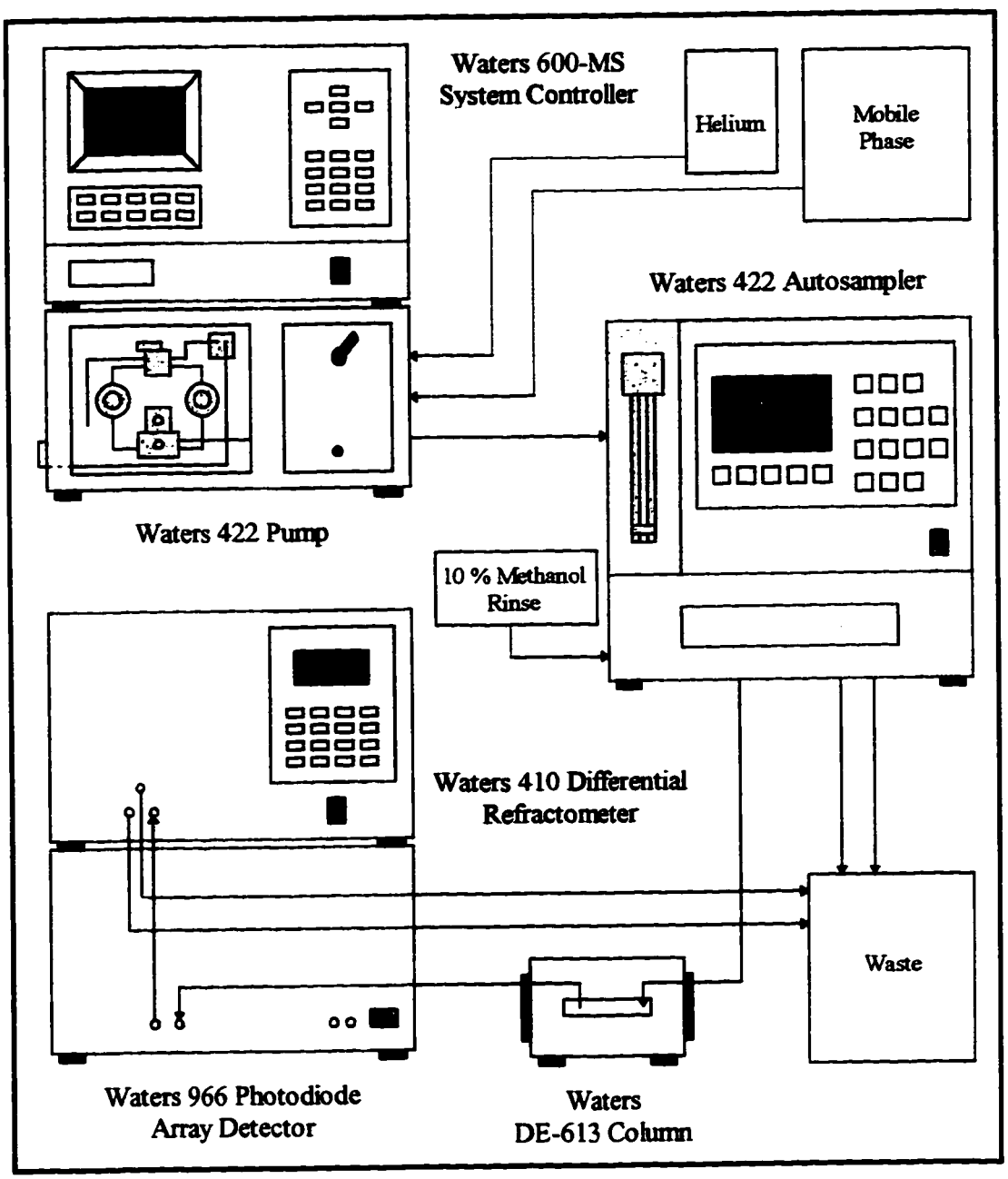

Figure 2.2.6.1. Waters high performance liquid chromatography system.

reversed-phase chromatography. This hydrophobic separation technique is based on the interaction between protein non-polar amino acid side chains with the packing surface. The Waters Shodex Rspak DE-613 column has a wide pore, polymethacrylate packing that is stable in the pH range of 2 to 12, and can be cleaned using caustic solutions [42]. Although only one species was quantitated in this work, a column was required to reduce injector noise. 700 µl plastic shell conical vials having a maximum residual volume of 50 µl are used to hold samples within a 90 vial autosampler carousel.

2.2.7 Data Acquisition and Control System

The *in situ* membrane permeability determination employed an IBM-compatible 486DX computer to acquire pressure readings and permeate weights, and to control the pump. RS-232-C cheater cables were built to communicate between the computer and devices (**Figs. 2.2.7.1 through 2.2.7.3**) with a Visual BASIC program. The computer, equipped with a proprietary input/output board, was used to control the HPLC system via a GPIB interface and to analyze chromatograms with Waters Millennium software.

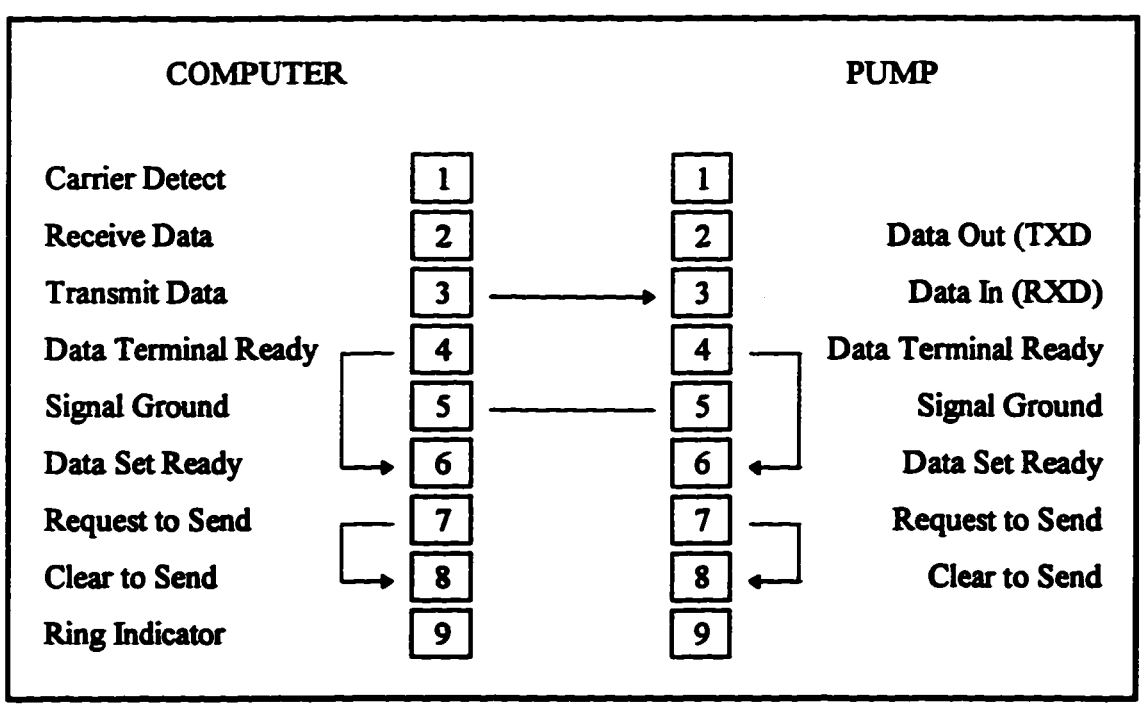

Figure 2.2.7.1. RS-232-C cheater cable for pump control.

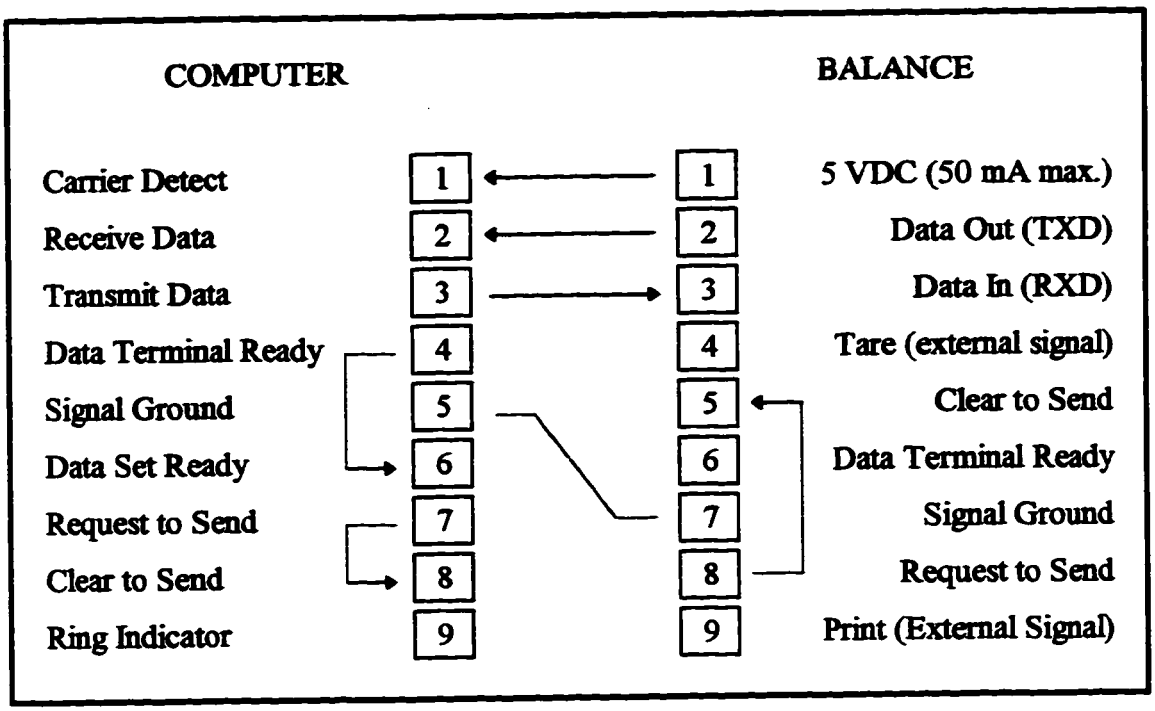

Figure 2.2.7.2. RS-232-C cheater cable for balance control and acquisition.

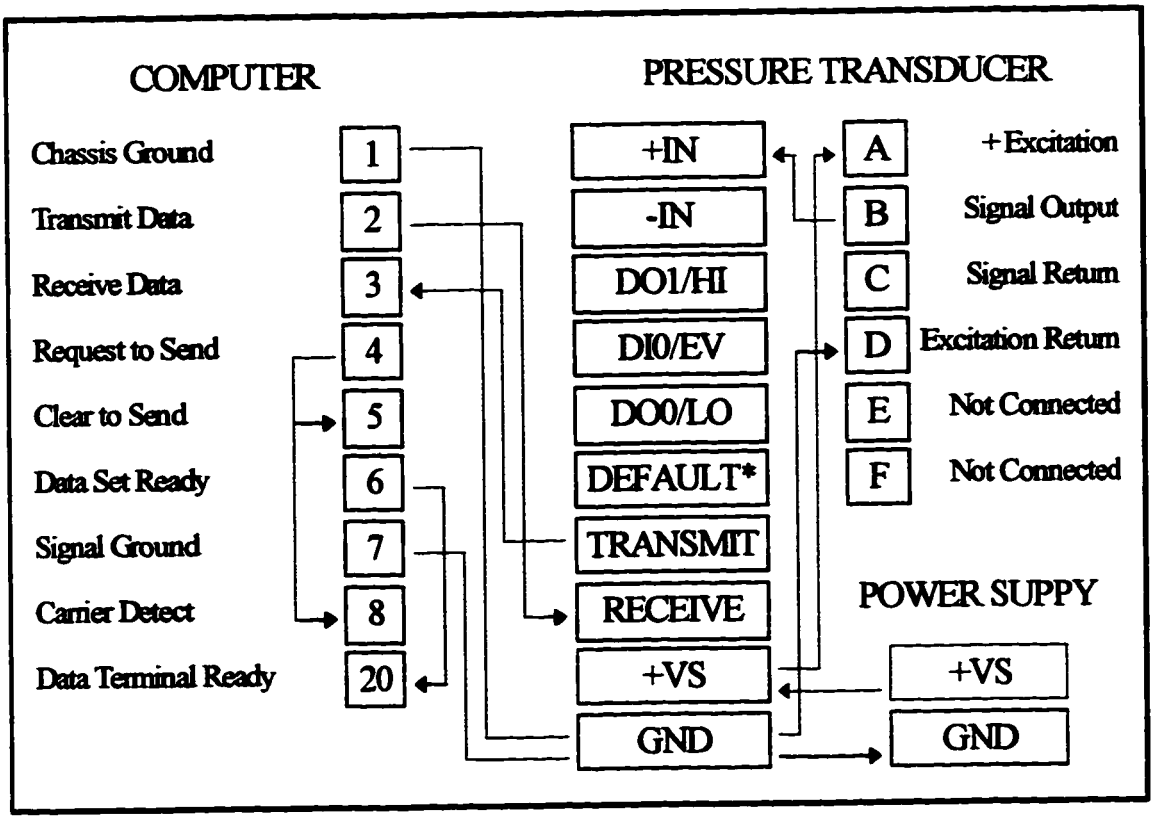

Figure 2.2.7.3. 25-pin serial port connector and pressure transducer connections.

2.3 Methodology

The following subsections describe in detail the procedures carried out in the protein polarization study.

2.3.1 Flow Cell Assembly

Prior to assembly of the flow cell, all surfaces are swabbed clean with methanol and deionized water. A 61.0 cm by 1.27 cm rectangular piece is cut from the cellulose acetate membrane sheet. Next, a 63.5 cm by 5.08 cm piece of Parafilm® is cut. Using the rectangular membrane as a template, the inside of the Parafilm® is cut out. The outer

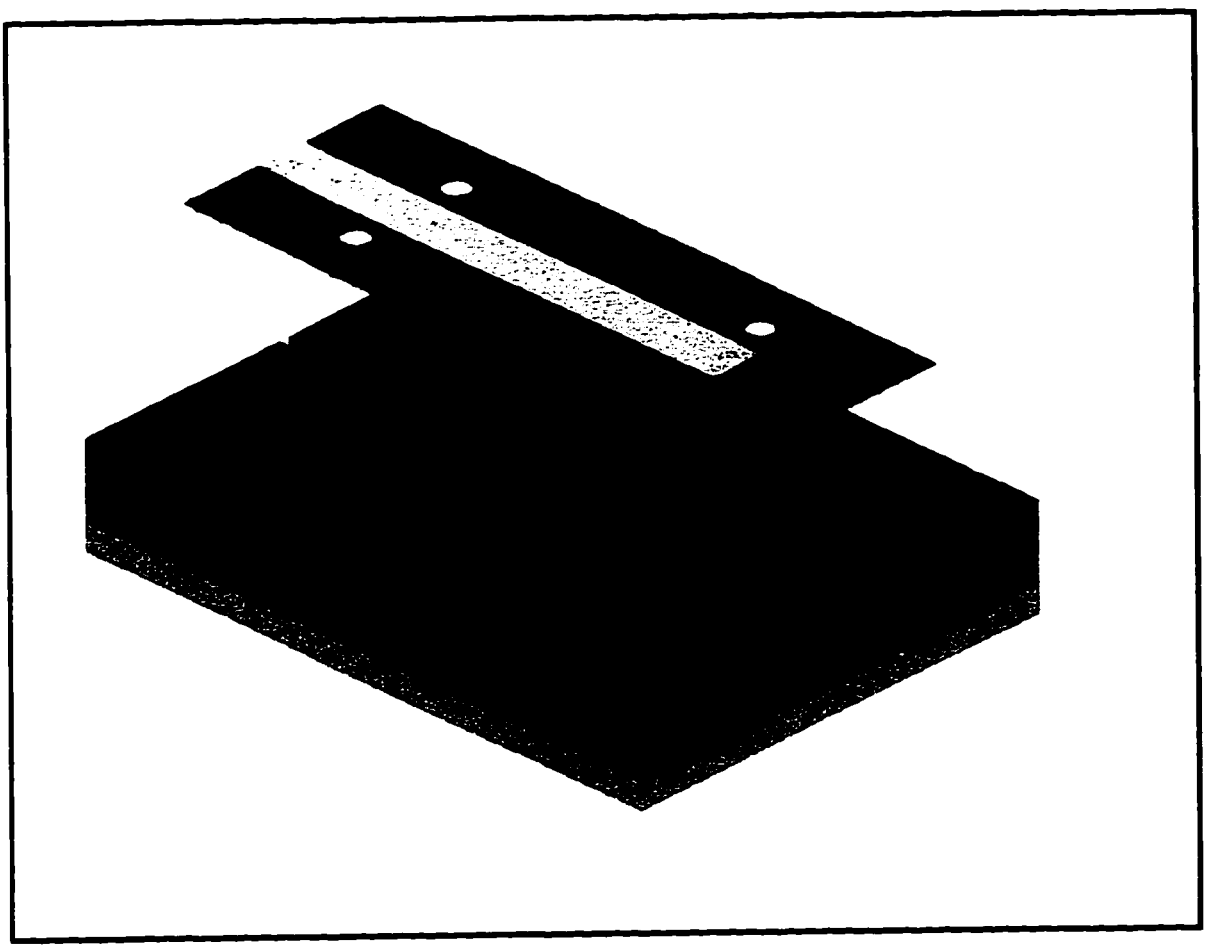

Figure 2.3.1.1. Membrane and gasket positioning over lower chamber of the flow cell.

portion of the Parafilm® is slit such that two similar L-shaped pieces remain. These L-shaped gasket pieces are annealed to the shiny polyester backing of the membrane by pressure. This can be accomplished by overlapping the gasket and membrane by 0.2 cm and carefully pressing the Parafilm® against the membrane with a smooth, hard object. At this point, the flow cell can be assembled as follows:

1. The lower stainless steel plate is placed on a flat surface.
2. The lower Plexiglas® plate is placed on the stainless steel plate and the two alignment pins (0.635 cm in diameter each) are inserted.
3. The membrane and gasket assembly is positioned symmetrically over the channel in the lower Plexiglas® plate (**Fig. 2.3.1.1**), with the cellulose acetate side up. The membrane and gasket must be as smooth as possible: Bubbles and ripples can be lightly pressed out, but excessive compression of the gasket will result in a poor seal.
4. The upper Plexiglas® plate is aligned with the pins and placed on the lower plate.
5. Septa are inserted into the six sampling ports. The numbered capillaries are inserted into their respective ports (*nota bene*, since the ports vary slightly in depth, the capillaries are of different lengths).
6. The upper stainless steel plate is aligned with the pins and placed over the upper Plexiglas® plate.
7. The plates are bolted together. Beginning from the central portion of the flow cell and working outwards, bolts are finger tightened and then successively tightened with a ratchet wrench. Care must be taken not to strip the bolts. Additionally, undue deformation of the Parafilm® gasket must be avoided. In the holes where the gasket obstructs the passage of bolts, bolts gently heated with a propane torch can be used to melt the Parafilm®.

Once the flow cell is assembled, the support rod can be affixed. Alternatively, if the support rod is affixed to the lower stainless steel plate first, supports can be placed under the plate during assembly of the flow cell. An exploded view of the flow cell components is given in **Fig. 2.3.1.2.**

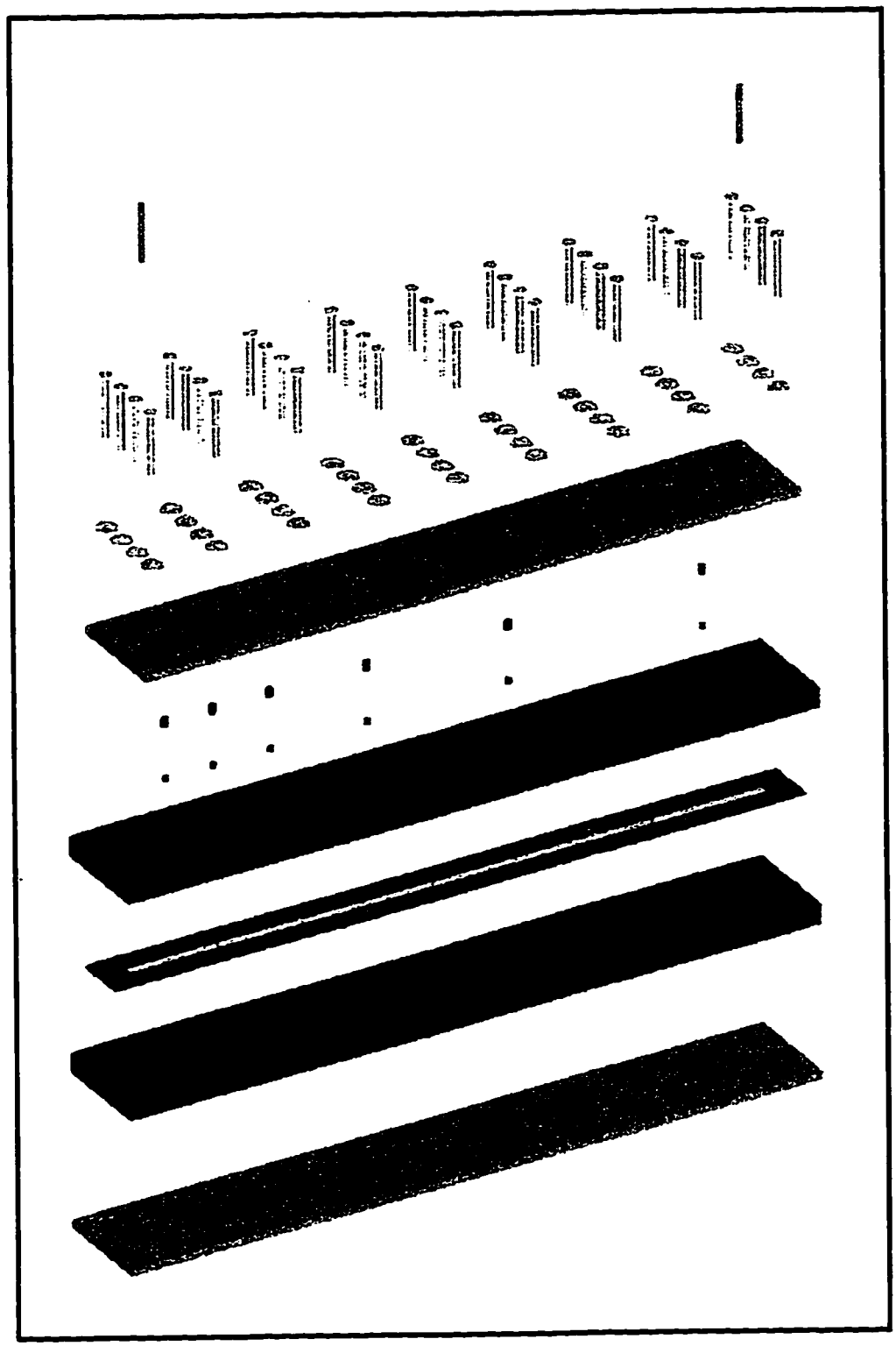

Figure 2.3.1.2. Exploded view of the rectilinear flow cell.

2.3.2 Leak Test

The upper and lower channel inlets are joined with a T-connector, making a common inlet for both channels. A similar connection is made at the outlet end. A 172 kPa (25 psi) pressure gauge and valve are connected to the downstream end. The flow cell is submerged in a water bath and pressurized with helium to approximately 140 kPa (20 psi). If a leak is detected at a fitting, the connector is tightened or replaced as required. A leak between the Plexiglas® plates may be eliminated by tightening bolts in the region of the leak. If this fails to stop the leak, a new membrane and gasket assembly must be installed in the flow cell. Because of vibration and wear, leaks may appear at a later time. It is recommended that leak tests be performed periodically, and especially when fluid loss is suspected.

2.3.3 Flow Configuration

For the circulation of fluid in the lower channel of the flow cell, the upper and lower channel inlets and outlets are uncoupled. Suction on the downstream end of the lower channel is reduced by leaving the outlet open to the atmosphere. This is accomplished by ensuring that the tubing is at the same height as the outlet and fluid flows into a small open funnel. The fluid in the funnel then returns to a reservoir which must be well below the pump inlet. This configuration must not be changed after pump calibration.

2.3.4 Pump Calibration

The pump is calibrated by passing deionized water through the lower channel. The flow configuration must be as described above with the exception that permeate flowing from the lower channel is collected in a container placed on the balance. Initially, the pump is calibrated with its built-in software. Precise volumetric flow is obtained by applying a temperature dependent density correction to the mass of fluid collected and

dividing by the total time of flow. In practice, however, it was found that only part of the pump output range is accurately calibrated in this manner. Furthermore, repositioning of the fluid reservoir or the flow cell outlet necessitates recalibration.

If calibration of the full output range is desired, replicate measurements must be carried out at a number of pump settings. Since the average velocity through the lower channel is desired, the calculated volumetric flow rates can be converted and plotted against the pump settings (apparent flow) to give a calibration curve. A sample plot is shown in **Fig. 2.3.4.1.** Linear regression is used to obtain a correlation for setting the pump. Sample calculations are given in **Appendix B.**

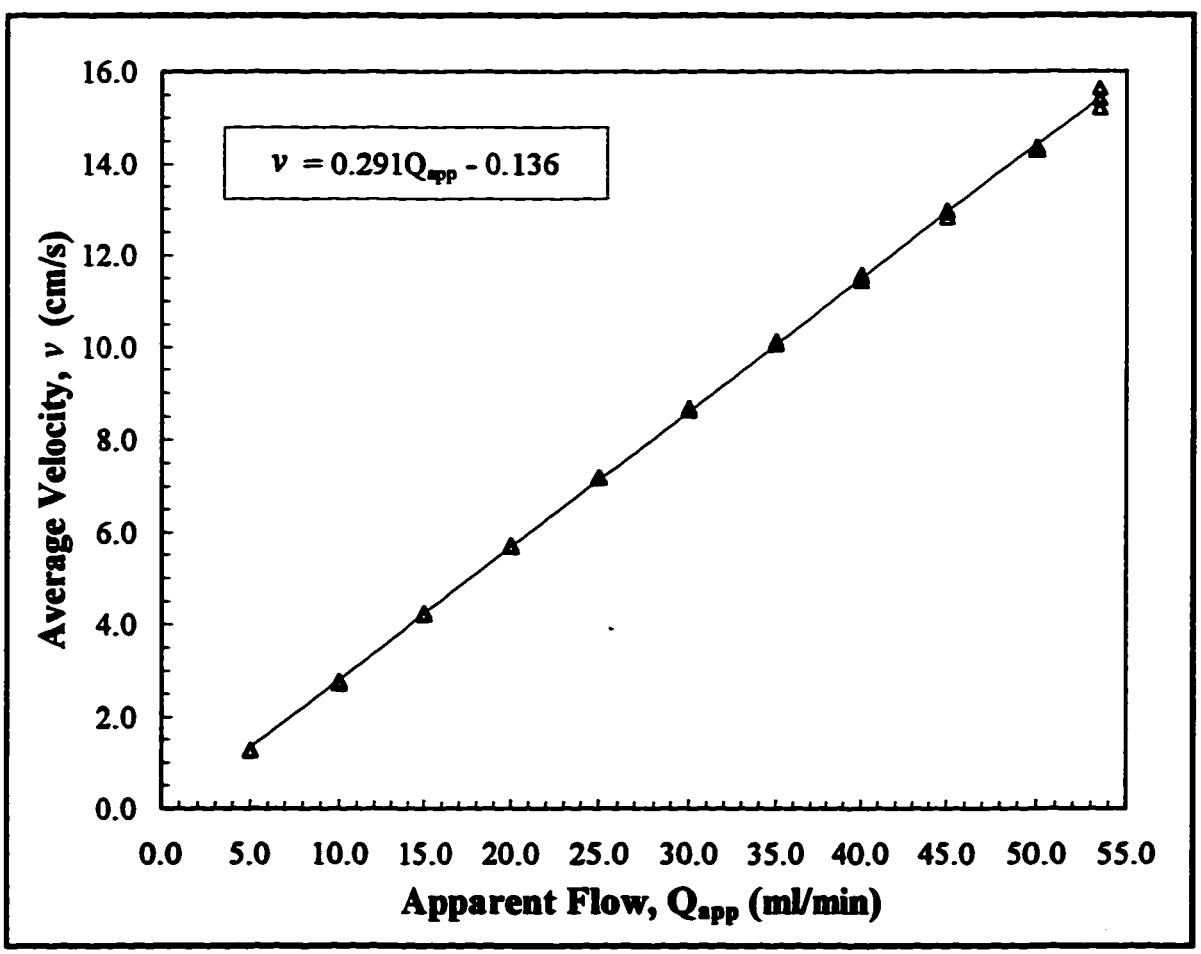

Figure 2.3.4.1. Sample pump calibration curve.

2.3.5 Flow Surface Disinfection

Although 0.1 % sodium azide was used in the dilute buffer and protein solutions, bacterial fouling may occur after prolonged polarization trials. The likelihood of this occurring is greatly diminished through the use of aseptic techniques. To further reduce the chances of bacterial growth, the flow cell, fluid reservoir and all tubing are filled with formalin and allowed to sit overnight. The formalin can then be rinsed out of the system with copious quantities of sterilized water. If at any point bacterial fouling is suspected, the procedure may be repeated and fresh solutions should be made up.

2.3.6 Flow Surface and Membrane Conditioning

Protein adsorption on flow surfaces and the membrane has two important implications on the polarization trials. Firstly, it may result in significant protein loss from solution and hence a lower starting concentration. Secondly, adsorption on the membrane may reduce its permeability substantially [5]. To correct for adsorption, the protein solution is slowly circulated (at approximately 5 ml/min) through the upper channel of the flow cell for 24 hours. The protein solution can then be tested for the true initial concentration. *In situ* membrane permeability determinations were conducted prior to conditioning and after all polarization trials were completed.

2.3.7 Protein Polarization Trials

The steps required to conduct successful protein polarization trials are as follows.

1. The six Hamilton syringes are inserted into the flow cell sampling ports to a depth just above the upper channel wall. This reduces the chance of leakage through septa.
2. The protein solution is slowly loaded into the upper channel of the flow cell. The first 20 to 30 ml of fluid exiting the cell are discarded in order to reduce the chance of

dilution with residual buffer or water in the pump head. The flow cell is oriented and re-oriented until all air bubbles are worked out of the inlet, upper channel, and outlet. Once all air bubbles are purged, the protein solution is circulated through upper channel, with magnetic stirring in the external reservoir, for 2 hours.

3. At the end of the 2 hour circulation period, the upper channel inlet and outlet are closed. The tubing connected to the upper channel is disconnected and the outlet is briefly opened to allow for pressure equilibration. Air must not be allowed into the outlet end. The outlet is then closed and the flow cell is allowed to equilibrate for an additional 2 hours.
4. The pump head is then rinsed by passing approximately 500 ml of deionized water through it. The pump is assumed to be free of protein contamination when no foam forms on the outlet side under high flow conditions (approximately 40 ml/min).
5. The reservoir is filled with dilute buffer and connected to the pump and lower channel as described in the flow configuration section. The pump is set to the desired apparent volumetric flow rate.
6. At the end of the 2 hour equilibration period, the inlet and outlet of the lower channel are opened and the pump is turned on. The dilute buffer is circulated through the lower channel, with magnetic stirring in the reservoir, until a desired run time has elapsed.
7. At the end of the trial, the pump is turned off and the lower channel's inlet and outlet ports are closed.
8. The syringes are inserted into the channel, about mid way between the membrane and the center of the channel, and six 20 μl samples are withdrawn. In addition, 20 μl samples of the dilute buffer and the protein solution are obtained to check for cross-contamination and protein loss, respectively.
9. Each sample is transferred to an autosampler vial containing 100 μl of dilute buffer. Also, a 100 μl uncirculated dilute buffer blank can be prepared. The autosampler vials are refrigerated at approximately 4°C until protein determination can be carried out.
10. The process is repeated for subsequent polarization trials.

2.3.8 Protein Determination

Protein concentrations are determined by HPLC using Waters Millennium software. For best results, calibration standards should be treated similarly to samples. Cost-effective preparation of standards can be carried out by beginning with a small volume (20 to 50 ml) of concentrated solution, and diluting several times. Mixing flasks of 20 to 50 ml capacities are ideal for preparation of standards. To obtain accurate results, sufficient time must be allowed for the dissipation of foam. A 20 µl aliquot of each standard is then mixed with 100 µl of dilute buffer in an autosampler vial. Standards and samples in autosampler vials are agitated thoroughly before the vials are loaded into the carousel. A standard curve can be constructed by plotting concentration against chromatogram peak area at 280 nm. A sample standard curve is plotted in **Fig. 2.3.8.1**. Details of the preparation of the HPLC system, data acquisition, and data analysis with Waters Millennium software are presented in **Appendix C**.

2.3.9 *In Situ* Membrane Permeability Determination

In the past, membrane permeability was determined by testing several coupons, or sample pieces, and averaging the permeabilities of the individual coupons [5]. The accuracy of this procedure is questionable since the membrane sheet is nonhomogeneous and only a small number of coupons can practically be tested. Consequently, an *in situ* method for determining the average membrane permeability was devised. The salient features of the experimental set up (refer to **Fig. 2.3.9.1**) are as follows:

1. The fully assembled flow cell is placed in the horizontal orientation. The pressure transducer is connected to the inlet of the lower channel and the outlet of the upper channel. In this configuration, the pressure transducer measures the approximate average pressure drop across the membrane.

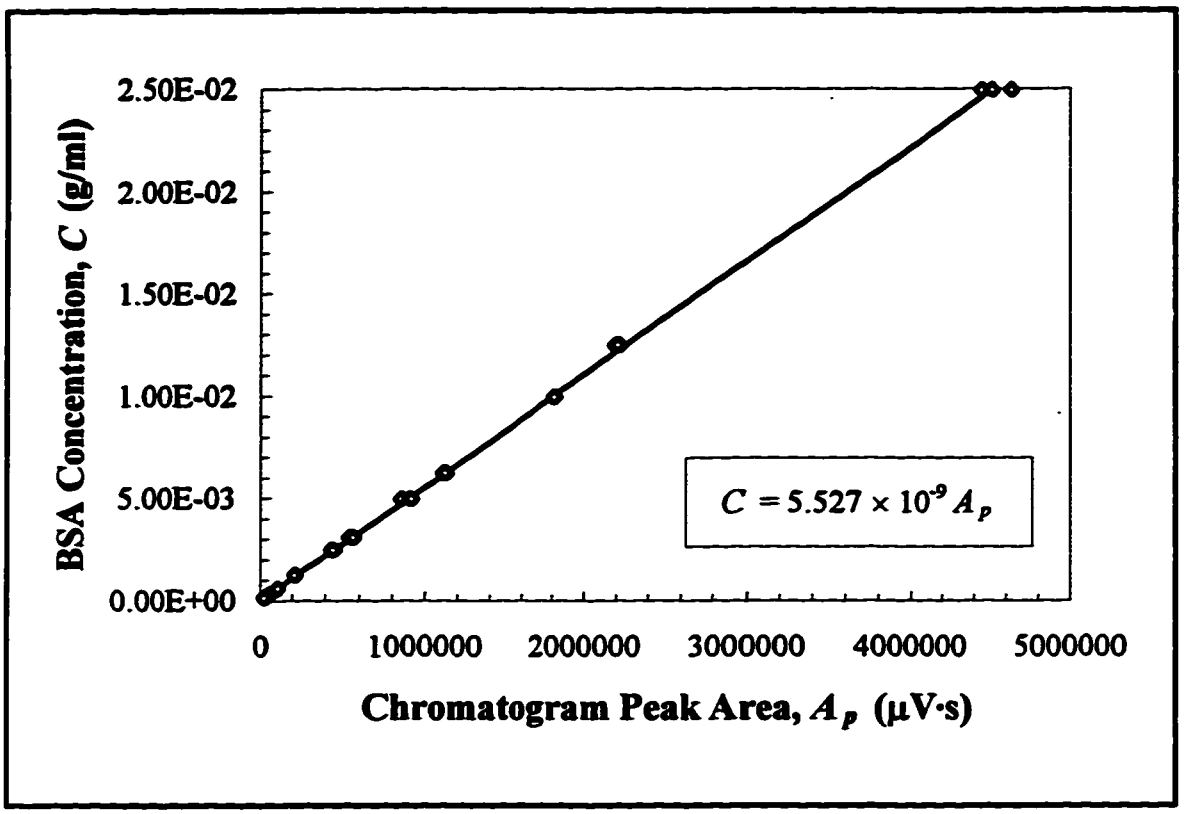

Figure 2.3.8.1. Sample BSA standard curve.

2. A reservoir containing deionized water, placed below the pump, is connected to the pump inlet. The pump outlet is then connected to the lower channel of the flow cell. The lower channel outlet is connected to the tubing that provides the hydrostatic head. A funnel, connected to the reservoir return, is positioned under the outlet at the highest point.
3. The upper channel is filled with deionized water and the inlet is closed. Tubing attached to the upper channel outlet is passed through a hole in the balance cover. A small container is placed on the balance to catch the permeate. To reduce the rate of evaporation, four water-filled 10 ml beakers are placed under the balance cover.
4. The pressure drop across the membrane can be controlled in two ways. Large pressure changes are effected by vertically moving the lower channel outlet tubing in increments of roughly 46 cm. Smaller changes are brought about by changing the flow rate through the lower channel by 5 to 10 ml/min.

5. Data acquisition and pump control are automated with the Visual BASIC program, ACK.BAS. Pressure and permeate weight readings are recorded for each of the five hydrostatic head positions and several flow rates.
6. The data are analyzed as in **Appendix B** to give a plot of the permeate rate as a function of the transmembrane pressure drop (**Fig. 2.3.9.2**). The average membrane permeability is then calculated using the slope of this plot, the cross-sectional area to flow, and the fluid viscosity.

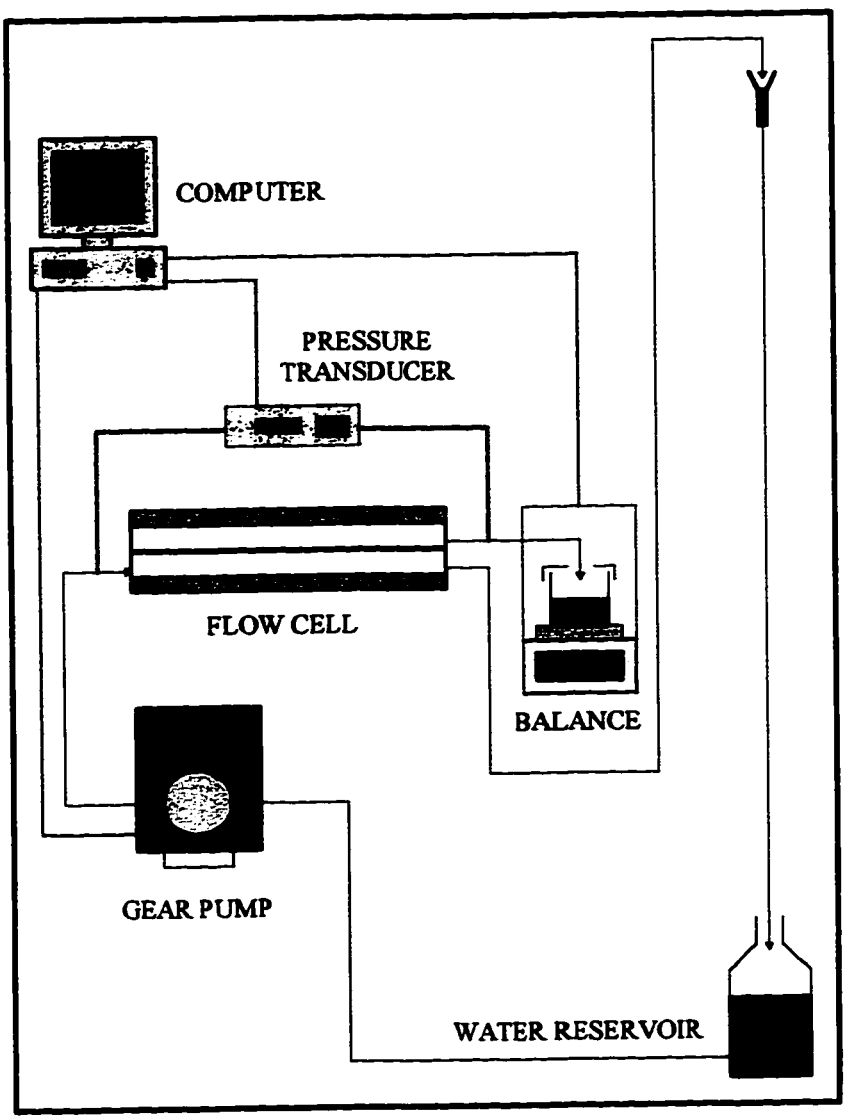

Figure 2.3.9.1. Schematic diagram of the equipment setup for *in situ* membrane permeability determination.

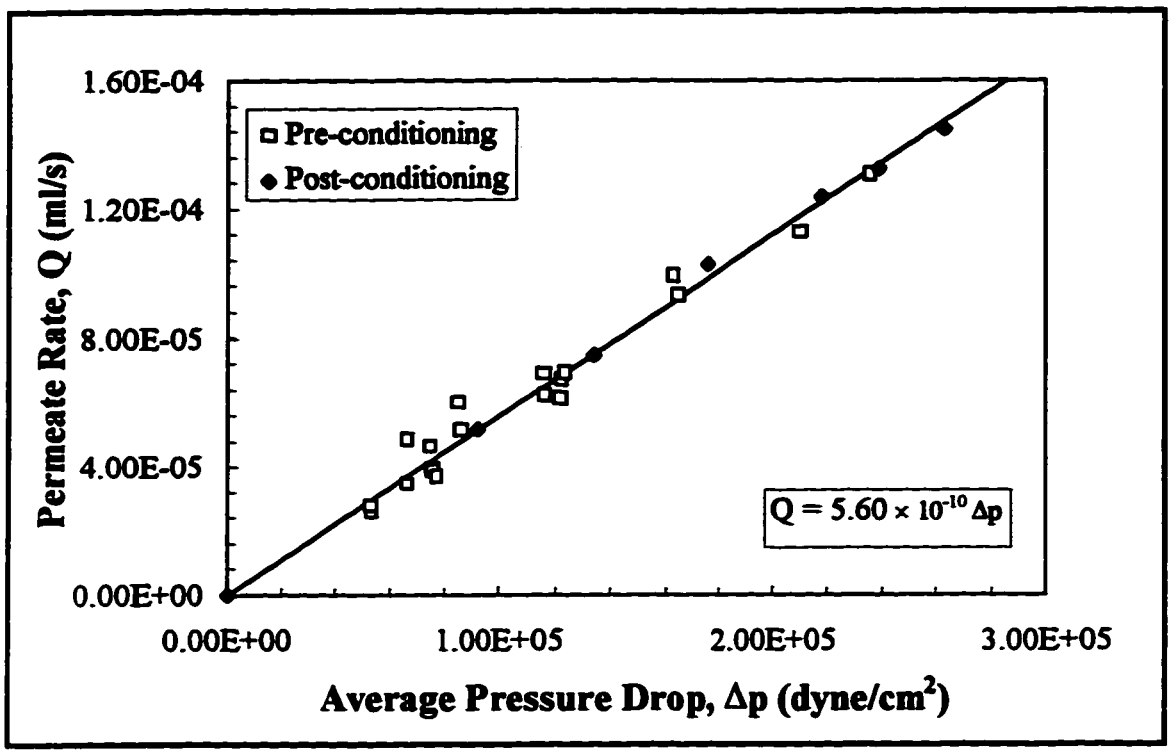

Figure 2.3.9.2. Permeate rate versus transmembrane pressure drop.

2.3.10 Membrane Thickness Determination

The membrane thickness can be obtained by averaging vernier caliper measurements made along a wet membrane strip. The cellulose acetate membrane, including the polyester backing, has an average measured thickness of approximately 0.025 cm. This finding was confirmed by microscopic examination of membrane sections.

Chapter 3

Theoretical Aspects

3.1 Governing Equations

Viscous flows of pure isothermal fluids are governed by the equation of continuity,

$$\frac{\partial \rho}{\partial t} = -(\nabla \cdot \rho \vec{v}), \tag{3.1.1}$$

and the momentum equations,

$$\frac{\partial(\rho u)}{\partial t} + \nabla \cdot (\rho \vec{v} u) = \nabla \cdot (\mu \nabla u) - \frac{\partial p}{\partial x} + \rho g_x + V_x, \tag{3.1.2a}$$

$$\frac{\partial(\rho v)}{\partial t} + \nabla \cdot (\rho \vec{v} v) = \nabla \cdot (\mu \nabla v) - \frac{\partial p}{\partial y} + \rho g_y + V_y, \tag{3.1.2b}$$

$$\frac{\partial(\rho w)}{\partial t} + \nabla \cdot (\rho \vec{v} w) = \nabla \cdot (\mu \nabla w) - \frac{\partial p}{\partial z} + \rho g_z + V_z, \tag{3.1.2c}$$

where the V terms represent additional viscous contributions and

$$|\vec{v}| = \sqrt{u^2 + v^2 + w^2}. \tag{3.1.3}$$

For a Newtonian fluid with constant density and viscosity, as is the case in the lower chamber of our flow cell, **equations 3.1.2a** through **3.1.2c** may be simplified with the equation of continuity to give the famous Navier-Stokes equation,

$$\rho \frac{D\vec{v}}{Dt} = -\nabla p + \mu \nabla^2 \vec{v} + \rho \vec{g}, \tag{3.1.4}$$

where the substantial time derivative is defined as

$$\frac{D\vec{v}}{Dt} = \frac{\partial \vec{v}}{\partial t} + u\frac{\partial \vec{v}}{\partial x} + v\frac{\partial \vec{v}}{\partial y} + w\frac{\partial \vec{v}}{\partial z}. \tag{3.1.5}$$

If the membrane is assumed to be anisotropic (that is, fluid flows through the membrane in only one direction), then the one-dimensional form of Darcy's law may be used to calculate membrane velocities:

$$v_m = -\frac{\kappa}{\mu}\frac{dp}{dy}. \tag{3.1.6}$$

Integration of **equation 3.1.6** across the membrane thickness, H_m, yields

$$v_m = \frac{\kappa}{H_m \mu}(p_L + \Pi_U - p_U) \equiv \frac{L_p}{\mu}(p_L + \Pi_U - p_U) \tag{3.1.7}$$

where the membrane permeability, L_p, is the ratio of the Darcy permeability, κ, and the membrane thickness. The osmotic pressure term, Π_U, arises from the presence of osmotically active species in the upper channel of the flow cell.

The conservation of chemical species in the presence of a velocity field is given by

$$\frac{\partial(\rho m_i)}{\partial t} + \nabla \cdot \left(\rho \vec{v} m_i + \vec{J}_i\right) = R_i \tag{3.1.8}$$

where R_i is the rate of generation of species i per unit volume. Since no chemical reactions occur in our system, R_i is exactly zero.

If the diffusion flux is defined by Fick's law of diffusion,

$$\vec{J}_i = -D_i \nabla m_i, \tag{3.1.9}$$

then **equation 3.1.8** may be rewritten as:

$$\frac{\partial(\rho m_i)}{\partial t} + \nabla \cdot (\rho \vec{v} m_i) = \nabla \cdot (D_i \nabla m_i). \tag{3.1.10}$$

3.2 Other Relationships

The osmotic pressure may be calculated with a semi-empirical equation of the form **[5, 13]**

$$\Pi = \Re T \sum_{i=1}^{n} \left[\frac{C_i}{M_i} \left(A_{i,1} + A_{i,2} C_i + A_{i,3} C_i^2 \right) \right]. \tag{3.2.1}$$

The required parameters for BSA and Dextran 70 are listed in **Table 3.2.1**.

Table 3.2.1. Osmotic pressure parameters for BSA and Dextran 70 [5, 13].

	BSA	Dextran 70
Species, i	1	2
Effective Molecular Weight, M_i (Da)	69000	70000
$A_{i,1}$	1.0000	1.6503
$A_{i,2}$ (ml/g)	1.0473×10^{-2}	2.7412×10^{-2}
$A_{i,3}$ (ml^2/g^2)	1.7374×10^{-5}	1.0755×10^{-4}

Empirical relationships for density, viscosity, and diffusivities as functions of temperature and species concentrations can be constructed by curve-fitting experimental and literature data. Details of curve-fitting results for BSA and Dextran 70 solutions are presented in the subsequent chapter.

4.3 Initial and Boundary Conditions

To solve the flow and concentration fields, the following initial and boundary conditions must be applied:

1. At time zero, the concentration of species *i* everywhere in the upper chamber is equal to an initial concentration. Elsewhere, the concentration of species *i* is set to zero.
2. Flow cell walls are represented by no-flow, no-slip boundaries.
3. Membrane surfaces are assumed to be no slip boundaries. Fluid flow through the membrane is governed by Darcy's law as described above.
4. The membrane is impermeable to the osmotically active species in the upper channel.
5. Fully parabolic flow is assumed along the lower chamber inlet.
6. Pressure at the lower chamber outlet is arbitrarily assumed equal to zero.

Chapter 4

Numerical Aspects

The following sections detail the development of a two-dimensional control volume model that describes the hydrodynamics and solute redistribution within the experimental flow cell. The model was developed in several stages, each building on the work of the previous one.

4.1 Preliminary Details

In his illustrative text of 1980, S. V. Patankar notes that in the relevant differential equations, the dependent variables "seem to obey a generalized conservation principle" [43]. Consequently, a general differential equation for an arbitrary dependent variable, ϕ, may be written as:

$$\frac{\partial(\rho\phi)}{\partial t} + \nabla\cdot(\rho\vec{v}\phi) = \nabla\cdot\left(\Gamma_\phi\nabla\phi\right) + S_\phi \qquad (4.1.1)$$

where Γ_ϕ is the diffusion coefficient, and S_ϕ is the source term. The ϕ subscripts are subsequently dropped for the sake of brevity. The power of **equation 4.1.1** lies in the fact that its discretized form can be used to obtain the discretized differential equation for any particular dependent variable. Before fully deriving control-volume discretization equations in two dimensions (2D), a number of conventions and rules must be addressed.

4.1.1 Control-Volume Formulation

In the control-volume formulation, the calculation domain is divided into nonoverlapping control volumes, each of which surrounds a single grid point. The differential equation is then integrated over each control volume through piecewise ϕ profiles between grid points. In this approach, the solution implies that exact integral conservation of ϕ exists for any number of control volumes, regardless of the grid point density.

The nomenclature used below is shown in the control volume of **Fig. 4.1.1.1**. The node of interest, P, is surrounded by a control volume of dimensions Δx by Δy by 1. Node W lies west of P (negative direction); nodes E, S, and N are located according to the other compass directions. Control volume faces are labeled similarly with the exception that lower case letters are used. Additionally, nodal distances in the x-direction are defined in **Fig. 4.1.1.2**. Nodal distances in the y-direction are similarly defined.

It should be noted that a node can lie anywhere within the control volume. However, from a computational standpoint, a scheme employing non-centrally located nodes can be problematic: it either requires additional storage of geometrical data (memory intensive) or more computational power to calculate the data (computationally intensive). Centrally-located nodes were considered adequate for the simple geometry of the rectilinear flow cell.

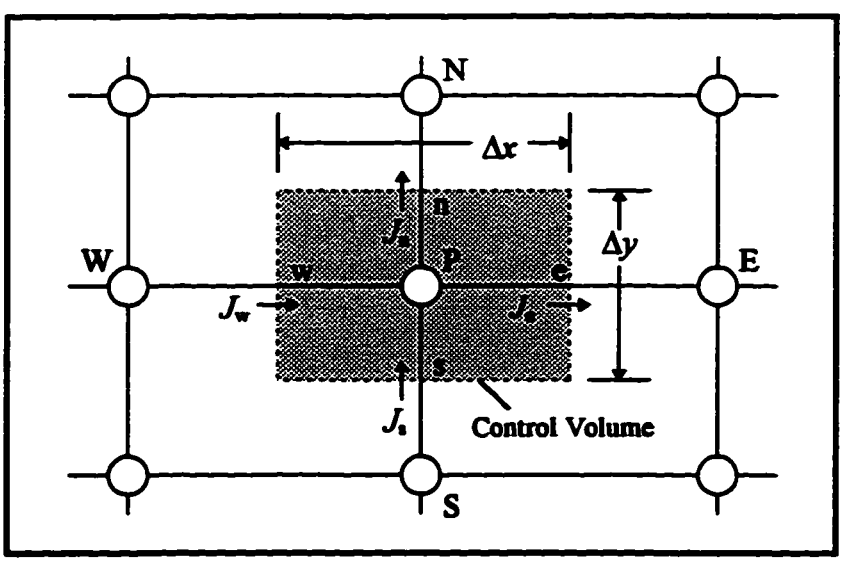

Figure 4.1.1.1. A control volume.

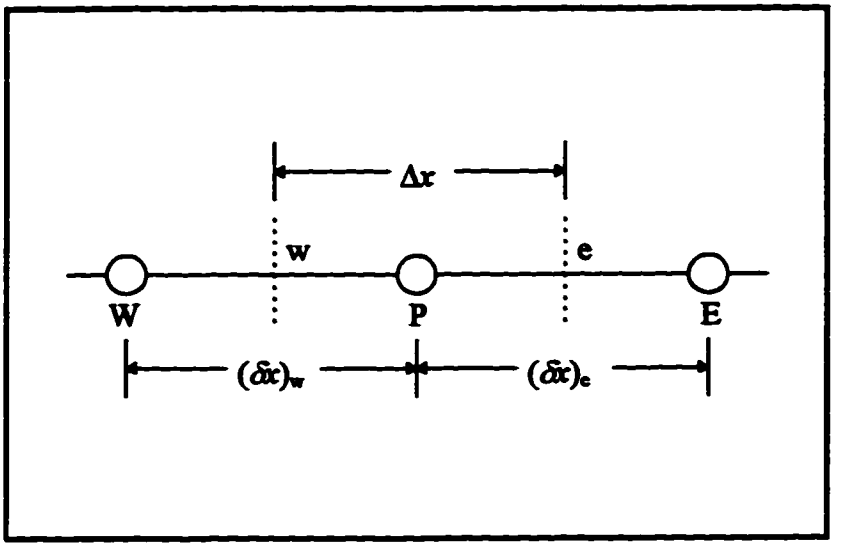

Figure 4.1.1.2. Nodal distances.

Returning to the generalized conservation **equation 4.1.1**, if the total (diffusion and convection) fluxes defined by

$$J_x \equiv \rho u \phi - \Gamma \frac{\partial \phi}{\partial x} \tag{4.1.1.1}$$

and

$$J_y \equiv \rho v \phi - \Gamma \frac{\partial \phi}{\partial y} \tag{4.1.1.2}$$

are introduced, the two dimensional form of the conservation equation becomes

$$\frac{\partial(\rho\phi)}{\partial t} + \frac{\partial J_x}{\partial x} + \frac{\partial J_y}{\partial y} = S. \tag{4.1.1.3}$$

At this point, integration over the control volume and discretization of **equation 4.1.1.3** and the equation of continuity,

$$\frac{\partial \rho}{\partial t} + \frac{\partial(\rho u)}{\partial x} + \frac{\partial(\rho v)}{\partial y} = 0, \tag{4.1.1.4}$$

present two difficulties. Firstly, we need to make an assumption about how ϕ_P, ϕ_E, ϕ_W, ϕ_N, and ϕ_S vary with time from t to $t + \Delta t$. Secondly, we desire a formulation in the form of grid node values only. It can be easily shown that numerous interpolation strategies exist for determining interfacial values. Since convection is to be included in the model and the solution procedure must be iterative, selection of an appropriate scheme is essential to obtaining physically realistic results. For example, a piecewise linear profile for ϕ (central-difference scheme) can only be applied to problems with low Reynolds numbers (and, thus, low Peclet numbers) [43]. These issues are addressed below.

4.1.2 S. V. Patankar's Four Basic Rules

The difficulties noted in the previous discussion can only be addressed after some ground rules are set. In choosing interpolation schemes and related practices, Patankar employs the criteria of overall balance and physical realism. Based on these he establishes the following four rules for discretization [43]:

"**Rule 1: Consistency at control-volume faces.** When a face is common to two adjacent control volumes, the flux across it must be represented by the *same* expression in the discretization equations for the two control volumes."

"**Rule 2: Positive coefficients.** All coefficients (a_P and neighbor coefficients a_{nb}) must always be positive." [This is a matter of convention: Alternatively, all coefficients must always be negative.]

"**Rule 3: Negative-slope linearization of the source term.** When the source term is linearized as $S = S_C + S_P T_P$, the coefficient S_P must always be less than or equal to zero." [ϕ may be substituted for the dependent variable T.]

"**Rule 4: Sum of the neighbor coefficients.** We require $a_p = \Sigma a_{nb}$ for situations where the differential equation continues to remain satisfied after a constant is added to the dependent variable."

The rationale and detailed implications of these rules are left up to the reader to explore in the literature [43]. Suffice it to say that with the general differential equation and the equation of continuity, these four rules form the framework of the numerical procedure.

4.1.3 Time Dependence

As will be seen later, integration of **equation 4.1.1.3** leads to terms containing the integral of the dependent variable at the nodes over time t to $t + \Delta t$. One generalized way of dealing with these expressions is by proposing

$$\int_t^{t+\Delta t} \phi_P \, dt = \left[f\phi_P^1 + (1-f)\phi_P^0 \right] \Delta t \qquad (4.1.3.1)$$

where f is a weighting factor between 0 and 1, and the 0 and 1 superscripts designate 'old' (known) and 'new' (unknown) values of ϕ_P, respectively. Similar expressions may be constructed for the other nodal ϕ variables. These expressions can then be used to derive a discretized form of **equation 4.1.1.3**. The actual derivation is beyond the scope of this discussion. However, for certain values of f, the discretization equation reduces to one of several well-known schemes.

If f is set to zero, ϕ_P is explicitly obtainable from known dependent variable values. This 'explicit' scheme assumes that the 'old' value prevails over the entire time step except at time $t + \Delta t$. Any scheme with $f \neq 0$ links ϕ_P with its neighbouring unknown values and is therefore implicit. Setting $f = 0.5$ leads to the Crank-Nicolson scheme, which assumes a linear variation of ϕ_P. The fully implicit scheme ($f = 1$) assumes that, at time t, ϕ_P suddenly changes from ϕ_P^0 to ϕ_P^1 and then remains at its new value over the entire time step.

We must now select the most appropriate scheme for our numerical model. The explicit scheme appears to be rather convenient. On the other hand, the Crank-Nicolson

scheme seems intuitively sensible. However, both of these schemes have a significant limitation. It can be shown that if the time step is not sufficiently small, **rule 2** may be violated, potentially leading to unrealistic results [43]. Its simplicity and unconditional adherence to **rule 2** make the fully implicit method (that is, $f = 1$) the scheme of choice for discretizing the time variation of ϕ.

4.1.4 Initial Derivation of the Discretization Equation

With the fully implicit scheme for time dependence and the **four basic rules** as guides, integration and discretization of **equation 4.1.1.3** over the control volume yields

$$\frac{(\rho_P\phi_P - \rho_P^0\phi_P^0)\Delta x\Delta y}{\Delta t} + J_e - J_w + J_n - J_s = (S_C + S_P\phi_P)\Delta x\Delta y \qquad (4.1.4.1)$$

where the source term has been linearized as prescribed by **rule 3** and, for the unsteady state term, ρ_P and ϕ_P are assumed to prevail over the entire control volume. Similarly, integration of **equation 4.1.1.3** over the control volume gives

$$\frac{(\rho_P - \rho_P^0)\Delta x\Delta y}{\Delta t} + F_e - F_e + F_n - F_s = 0, \qquad (4.1.4.2)$$

where the mass flow rates through the control volume faces are defined as

$$F_e = (\rho u)_e \Delta y, \qquad (4.1.4.3a)$$

$$F_w = (\rho u)_w \Delta y, \qquad (4.1.4.3b)$$

$$F_n = (\rho v)_n \Delta x, \qquad (4.1.4.3c)$$

$$F_s = (\rho v)_s \Delta x. \qquad (4.1.4.3d)$$

It should be noted that the ρu terms are assumed to prevail over their respective interfaces. Multiplication of **equation 4.1.4.2** by ϕ_P and subtraction from **equation 4.1.4.1** gives

$$\left(\phi_P - \phi_P^0\right)\frac{\rho_P^0 \Delta x \Delta y}{\Delta t} + \left(J_e - F_e\phi_P\right) - \left(J_w - F_w\phi_P\right) + \left(J_n - F_n\phi_P\right) - \left(J_s - F_s\phi_P\right) = \left(S_C + S_P\phi_P\right)\Delta x \Delta y \qquad (4.1.4.4)$$

To continue with the derivation, we require a way to express terms such as $\left(J_w - F_w\phi_P\right)$ as functions of nodal ϕ quantities.

4.1.5 Interpolation Schemes

A generalized formulation for the application of various interfacial interpolation schemes has been derived in the literature [43]. Only the final results are given here. It can be shown that

$$J_e - F_e\phi_P = a_E\left(\phi_P - \phi_E\right), \qquad (4.1.5.1a)$$

$$J_w - F_w\phi_P = a_W\left(\phi_W - \phi_P\right), \qquad (4.1.5.1b)$$

$$J_n - F_n\phi_P = a_N\left(\phi_P - \phi_N\right), \qquad (4.1.5.1c)$$

$$J_s - F_s\phi_P = a_S\left(\phi_S - \phi_P\right), \qquad (4.1.5.1d)$$

where

$$a_E = D_e A\left(\left|P_e\right|\right) + \left[-F_e, 0\right], \qquad (4.1.5.2a)$$

$$a_W = D_w A\left(\left|P_w\right|\right) + \left[F_w, 0\right], \qquad (4.1.5.2b)$$

$$a_N = D_n A\left(\left|P_n\right|\right) + \left[-F_n, 0\right], \qquad (4.1.5.2c)$$

$$a_S = D_s A\left(\left|P_s\right|\right) + \left[F_s, 0\right]. \qquad (4.1.5.2d)$$

In **equations 4.1.5.2a** through **4.1.5.2d**, the diffusive conductances are defined as

$$D_e = \frac{\Gamma_e \Delta y}{(\delta x)_e}, \tag{4.1.5.3a}$$

$$D_w = \frac{\Gamma_w \Delta y}{(\delta x)_w}, \tag{4.1.5.3b}$$

$$D_n = \frac{\Gamma_n \Delta y}{(\delta x)_n}, \tag{4.1.5.3c}$$

$$D_s = \frac{\Gamma_s \Delta y}{(\delta x)_s}, \tag{4.1.5.3d}$$

and the Peclet numbers are given by

$$P_e = \frac{F_e}{D_e}, \qquad P_w = \frac{F_w}{D_w}, \qquad P_n = \frac{F_n}{D_n}, \qquad \text{and } P_s = \frac{F_s}{D_s}. \tag{4.1.5.4}$$

Additionally, the ceiling function, $\lceil \text{argument 1}, \text{argument 2}, \ldots, \text{argument n} \rceil$, is simply the maximum of arguments 1 through n, and the interpolation function, $A(|P|)$, is given in **Table 4.1.5.1**.

Table 4.1.5.1. Interpolation function, $A(|P|)$, for several schemes.

Scheme	$A(\|P\|)$
Central Difference	$1-0.5\|P\|$
Upwind	1
Hybrid	$\lceil 0, 1-0.5\|P\| \rceil$
Power Law	$\lceil 0, (1-0.1\|P\|)^5 \rceil$
Exponential	$\dfrac{\|P\|}{\exp(\|P\|)-1}$

As noted earlier, the central difference scheme is limited to low Peclet numbers. This limitation can be overcome through the use of fine grids. But, such a strategy is undesirable since it requires large amounts of computer memory and is computationally expensive. All the other schemes give realistic results regardless of grid density. The problem with the upwind scheme is that it always calculates the diffusion term from a linear profile; therefore, diffusion is overestimated at large Peclet numbers. The hybrid scheme, a combination of the central difference and upwind schemes, may be viewed as a three-line approximation to the exact curve. In general, the power law scheme, although somewhat more complicated, gives better results. The best results are obtained with the exponential scheme which gives the exact solution to steady one-dimensional problems. Since exponentials are costly to calculate, and the difference between the power law and exponential curves is quite small, the power law scheme is usually prescribed [43].

4.1.6 Final Derivation of the General Discretization Equation

Substitution of **equations 4.1.5.1a** through **4.1.5.1d** into **equation 4.1.4.4** with subsequent rearrangement gives the final discretization equation,

$$a_P\phi_P = a_E\phi_E + a_W\phi_W + a_N\phi_N + a_S\phi_S + b, \qquad (4.1.6.1)$$

where

$$a_P = a_E + a_W + a_N + a_S + a_P^0 - S_P\Delta x\Delta y, \qquad (4.1.6.2)$$

$$a_P^0 = \frac{\rho_P^0\Delta x\Delta y}{\Delta t}, \qquad (4.1.6.3)$$

and

$$b = S_C\Delta x\Delta y + a_P^0\phi_P^0. \qquad (4.1.6.4)$$

With the development of **equation 4.1.6.1**, it would appear that we are ready to develop an algorithm to solve flow fields iteratively. Unfortunately, two additional difficulties must be dealt with. These are addressed in the section that follows.

4.1.7 Difficulties in Calculating the Flow Field

The first difficulty in the calculation of the flow field is that both the velocity and pressure fields are unknown, and the pressure gradient is part of the source term, b, in the equation of motion. What we need, then, is some way to separate the pressure gradient from the source term and derive auxiliary equations to determine the pressure field.

The second difficulty is somewhat more subtle and can be attributed to the first derivatives of pressure (momentum equations) and velocity (equation of continuity). If the one-dimensional case of **Fig. 4.1.1.2** is considered, the pressure drop $p_w - p_e$ across the control volume of unit cross-sectional area is the only additional term to be considered in the discretization equation. If a piece-wise linear pressure profile is assumed, it can be shown that $p_w - p_e$ is a function of the nodal pressures, p_W and p_E only. Consequently, the momentum equations contain the pressure information of two alternate nodes, rather than that of two adjacent ones. This tends to reduce the accuracy of the solution since the pressure values are obtained from an effectively coarser grid. However, this is not the most significant problem. A uniform grid in which velocities and pressures lie at common nodes can generate an unrealistic 'wavy' pressure field in which the alternate pressures are equal (and adjacent pressures differ). Such a field would be seen by the momentum equation as being uniform over the entire calculation domain. This phenomenon can also occur in the two- and three-dimensional situations. In addition, it is not limited to the equations of motion: a 'wavy' velocity can arise even though the equation of continuity is satisfied **[43]**.

The latter problem can be remedied by employing a staggered grid, the topic of the following discussion. The former difficulty is subsequently addressed by deriving the discretized momentum, pressure, and pressure-correction equations in two dimensions.

4.1.7.1. The Staggered Grid

By defining a different grid for each dependent variable, the 'wavy' field difficulty can be eliminated. In the staggered grid of **Fig. 4.1.7.1.1**, the velocity components are displaced from the primary pressure grid. As a result, x- and y-velocities lie on the faces of pressure control volumes.

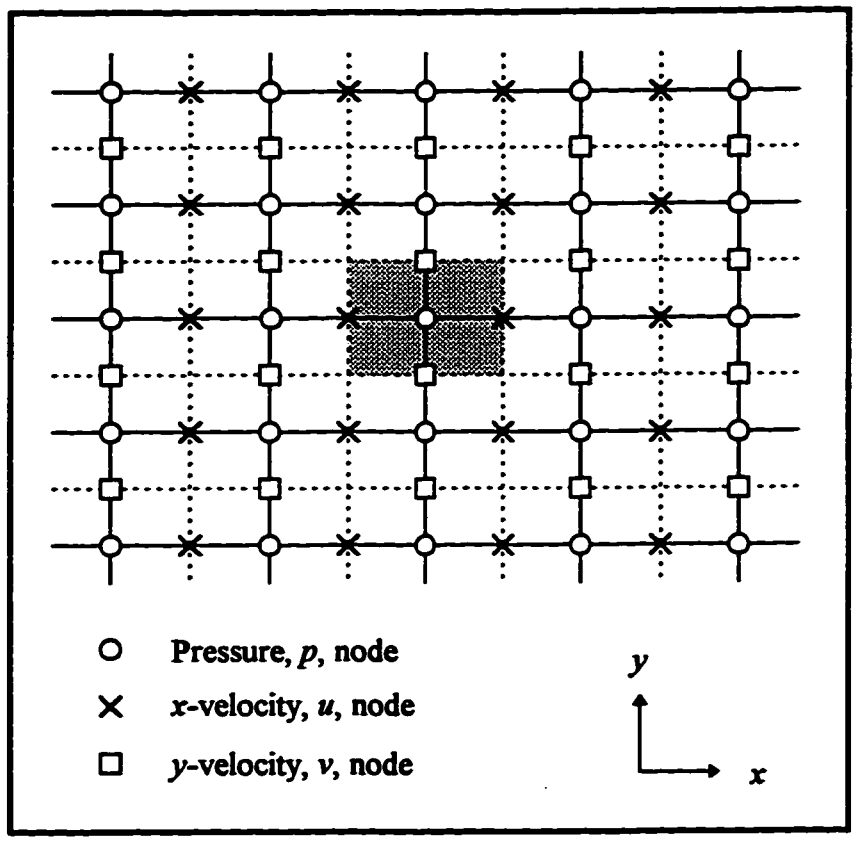

Figure 4.1.7.1.1. The staggered grid.

The staggered grid, first used in 1965 **[44]**, has two advantages over a uniform grid. Since the velocities lie on the main grid interfaces, mass flow rates across the control volume faces can be calculated without interpolation. More importantly, the information of adjacent grid locations is now used, preventing 'wavy' fields from arising. On the down side, the staggered grid requires that more geometric and indexing data be stored, and that other interpolations be performed **[43]**.

4.1.7.2. The Flow Field Equations

If we consider two adjacent nodes, P and E, on the staggered grid, and separate the pressure force, $p_P - p_E$, acting on the control volume in the x direction from the source term, b, then the discretization equation for u_e may be written as

$$a_e u_e = \sum a_{nb} u_{nb} + b + (p_P - p_E) A_e \qquad (4.1.7.2.1a)$$

where $A_e = \Delta y \times 1$ for two dimensions. Similarly, for v_n we can write

$$a_n v_n = \sum a_{nb} v_{nb} + b + (p_P - p_N) A_n \qquad (4.1.7.2.1b)$$

where $A_n = \Delta x \times 1$. These equations can only be solved if the pressure field is known or estimated. The equation of continuity will be satisfied only if the correct pressure field is used. Thus, the use of a 'guessed' pressure field p^* gives an imperfect ('starred') velocity field defined by

$$a_e u_e^* = \sum a_{nb} u_{nb}^* + b + (p_P^* - p_E^*) A_e, \qquad (4.1.7.2.2a)$$

$$a_n v_n^* = \sum a_{nb} v_{nb}^* + b + (p_P^* - p_N^*) A_n. \qquad (4.1.7.2.2b)$$

The correct pressure, p, can be determined with

$$p = p^* + p' \qquad (4.1.7.2.3)$$

where p' is the pressure correction. Similarly, velocity corrections can be applied to give

$$u = u^* + u' \quad \text{and} \quad v = v^* + v'. \qquad (4.1.7.2.4)$$

Subtraction of **equation 4.1.7.2.1a** from **equation 4.1.7.2.2a** and application of the above definitions lead to

$$a_e u_e' = \sum a_{nb} u_{nb}' + (p_P' - p_E') A_e. \qquad (4.1.7.2.5)$$

Omission of the $\Sigma a_{nb}u_{nb}'$ term in **equation 4.1.7.2.5** will allow for the derivation of a p' equation of the same form as the general ϕ equation. As a result, an iterative procedure that solves one variable a time will be possible. The resulting equation in two dimensions, upon rearrangement, becomes

$$u_e' = \frac{A_e}{a_e}(p_P' - p_E') \equiv \frac{\Delta y}{a_e}(p_P' - p_E'). \tag{4.1.7.2.6}$$

Thus, with equation 5.1.5.2.4, the velocity correction equation

$$u_e = u_e^* + \frac{\Delta y}{a_e}(p_P' - p_E') \tag{4.1.7.2.7}$$

is obtained. Similarly, the correction formula for the velocity in the y-direction is

$$v_n = v_n^* + \frac{\Delta x}{a_n}(p_P' - p_N'). \tag{4.1.7.2.8}$$

Substitution of **equations 4.1.7.2.7** and **4.1.7.2.8** into the discretized equation of continuity, upon rearrangement, yields

$$a_P p_P' = a_E p_E' + a_W p_W' + a_N p_N' + a_S p_S' + b, \tag{4.1.7.2.9}$$

where

$$a_E = \rho_e \frac{(\Delta y)^2}{a_e}, \tag{4.1.7.2.10a}$$

$$a_W = \rho_w \frac{(\Delta y)^2}{a_w}, \tag{4.1.7.2.10b}$$

$$a_N = \rho_n \frac{(\Delta x)^2}{a_n}, \tag{4.1.7.2.10c}$$

$$a_S = \rho_s \frac{(\Delta x)^2}{a_s}, \tag{4.1.7.2.10d}$$

$$a_P = a_E + a_W + a_N + a_S, \tag{4.1.7.2.10e}$$

and

$$b=\frac{(\rho_P^0-\rho_P)\Delta x\Delta y}{\Delta t}+\left[(\rho u)_w-(\rho u)_e\right]\Delta y+\left[(\rho v)_s-(\rho u)_n\right]\Delta x. \qquad (4.1.7.2.10f)$$

If the first term of the momentum equation,

$$u_e=\frac{\sum a_{nb}u_{nb}+b}{a_e}+\frac{\Delta y}{a_e}(p_P-p_E), \qquad (4.1.7.2.11)$$

is defined as the pseudovelocity, $u_e^{\#}$,

$$u_e^{\#}=\frac{\sum a_{nb}u_{nb}+b}{a_e}, \qquad (4.1.7.2.12)$$

then **equation 4.1.7.2.11** may be rewritten as:

$$u_e=u_e^{\#}+\frac{\Delta y}{a_e}(p_P-p_E). \qquad (4.1.7.2.13)$$

Similarly, we can obtain

$$v_n=v_n^{\#}+\frac{\Delta x}{a_n}(p_P-p_N). \qquad (4.1.7.2.14)$$

Using the latter two equations, the pressure equation can be derived similarly to p':

$$a_P p_P=a_E p_E+a_W p_W+a_N p_N+a_S p_S+b, \qquad (4.1.7.2.15)$$

where a_E, a_W, a_N, a_S, and a_P are given by **equations 4.1.7.2.10a** through **4.1.7.2.10e** and

$$b=\frac{(\rho_P^0-\rho_P)\Delta x\Delta y}{\Delta t}+\left[(\rho u^{\#})_w-(\rho u^{\#})_e\right]\Delta y+\left[(\rho v^{\#})_s-(\rho u^{\#})_n\right]\Delta x. \qquad (4.1.7.2.16)$$

With this last equation, we now have all of the tools necessary for solving fluid flow problems in two dimensions. What is missing, though, is a step-by-step methodology or algorithm.

4.1.8 SIMPLE and SIMPLER

For the formulations described above, Patankar gives two algorithms that allow the calculation of flow, mass, and energy fields [43]. These are SIMPLE (Semi-Implicit Method for Pressure-Linked Equations) and SIMPLER (SIMPLE Revised). The details of SIMPLE are not particularly important here. Under certain conditions often encountered in flow problems, SIMPLE is prone to divergence unless underrelaxation is used. This has been attributed to the omission of the $\Sigma a_{nb}u_{nb}'$ term in **equation 4.1.7.2.5**, which leads to exaggerated corrections of the pressure. The introduction of the pressure **equation 4.1.7.2.15** in SIMPLER, for the most part, eliminates this problem. Furthermore, the rate of convergence of SIMPLE has been found to be considerably slower than that of SIMPLER [43]. Consequently, SIMPLER was chosen for the numerical model of the rectilinear flow cell.

The SIMPLER algorithm, as described by Patankar [43] is as follows.

1. Start with a guessed velocity field.
2. Calculate the coefficients for the momentum equations and hence calculate $[u^{\#}, v^{\#}]$ from equations such as [**equation 4.1.7.2.12**] by substituting the values of the neighbor velocities, u_{nb}.
3. Calculate the coefficients for the pressure equation [**4.1.7.2.15**], and solve it to obtain the pressure field.
4. Treating this pressure field as p^*, solve the momentum equations to obtain $[u^*, v^*]$.
5. Calculate the mass source b [**equation 4.1.7.2.10f**] and hence solve the p' equation.
6. Correct the velocity field by use of [**equations 4.1.7.2.7 and 4.1.7.2.8**], but *do not* correct the pressure.
7. Solve the discretization equations for other ϕ's if necessary.
8. Return to step 2 and repeat until convergence.

4.2 Steady-State Parallel Plate Flow

In developing the discretized model we begin by considering steady-state viscous flow between parallel plates in the absence of a gravitational field. For this relatively simple scenario, all transient and source (S_C and S_P) terms drop out of the discretization equations. The grid employed here, with the relevant boundary conditions, is presented in **Fig. 4.2.1**. The main pressure grid consists of full control volumes. Half control volumes are used at the inlet and outlet for x-velocities, and at the plates for y-velocities.

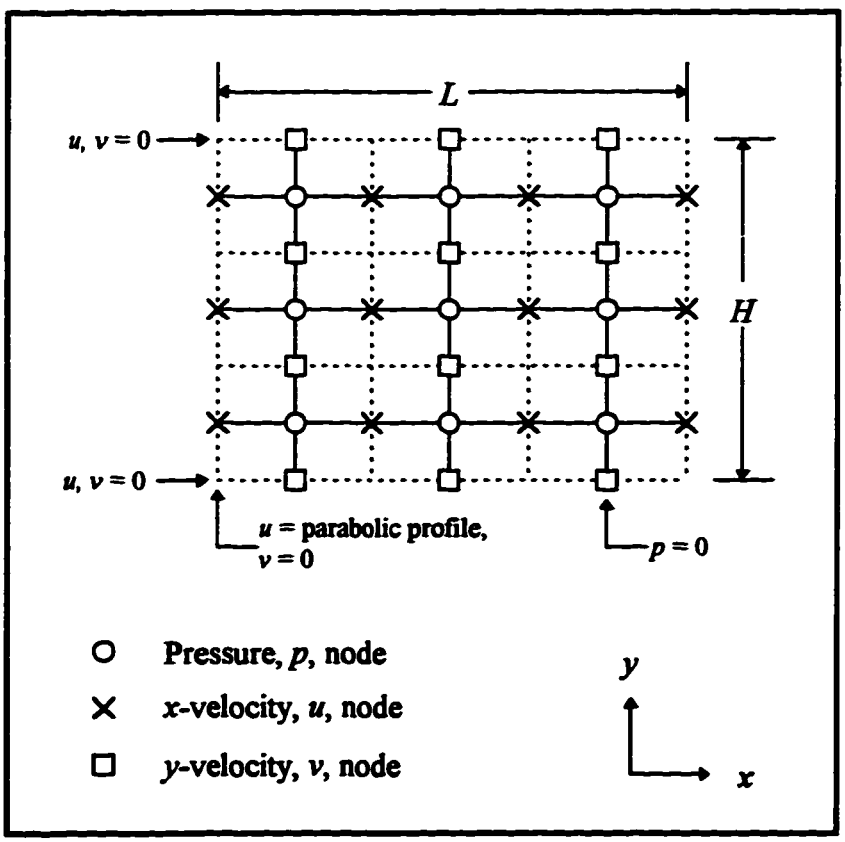

Figure 4.2.1. The staggered grid and boundary conditions.

To solve the flow field, we begin with **step 1** of the SIMPLER algorithm. Since an initial estimate for the velocity field may be difficult to determine for irregular geometries, all unknown velocities can be set to zero. While the initial guess has been observed to affect both the rate of convergence and the total time to convergence, a 'zero' velocity guess eliminates the complexities associated with obtaining reasonable initial approximations. Furthermore, under certain grid density and flow conditions, use of a nearly perfect velocity estimate as the initial guess can lead to longer convergence times than those obtained with the 'zero' guess.

In **step 2**, the coefficients for the momentum equations are calculated. Subsequently, the pseudovelocities ($u^{\#}$, $v^{\#}$) are determined (**equation 4.1.7.2.12**) by substituting the values of the neighbor velocities (u_{nb}, v_{nb}). The pseudovelocities are calculated once by moving along the grid from left to right and from top to bottom. This procedure is one iteration of the Gauss-Seidel point-by-point method.

Next, in **step 3** the coefficients for the pressure equation (**4.1.7.2.15**) are calculated. The pressure equation is then solved with the line-by-line tridiagonal matrix algorithm (TDMA). A summary of the algorithm, without derivation, is as follows:

For the discretization equation,

$$a_i\phi_i = b_i\phi_{i+1} + c_i\phi_{i-1} + d_i, \tag{4.2.1}$$

1. Calculate P_1 and Q_1 with:

$$P_1 = \frac{b_1}{a_1} \quad \text{and} \quad Q_1 = \frac{d_1}{a_1}. \tag{4.2.2}$$

2. Obtain P_i and Q_i for $i = 1, 2, 3, \ldots, N$, with:

$$P_i = \frac{b_i}{a_i - c_i P_{i-1}} \quad \text{and} \quad Q_i = \frac{d_i + c_i Q_{i-1}}{a_i - c_i P_{i-1}}. \tag{4.2.3}$$

3. Set $\phi_N = Q_N$.
4. Obtain $\phi_{N-1}, \phi_{N-2}, \ldots, \phi_3, \phi_2, \phi_1$ with:

$$\phi_i = P_i \phi_{i+1} + Q_i, \tag{4.2.4}$$

for $i = N-1, N-2, \ldots, 3, 2, 1$.

The algorithm moves from point to point along a line. For two dimensions, an iterative line-by-line technique is used in which contributions of nodes below and above the line are included within the d term of **equation 4.2.1**. In practice, convergence is normally obtained after completing several TDMA iterations. Furthermore, convergence can be sped up by choosing the best 'sweep' directions which bring boundary information most quickly into the calculation domain. Additionally, final convergence at this stage of SIMPLER, at considerable computational expense, is not really required since the pressure field obtained is only as good as the approximate velocity field used. By trial and error, it was discovered that one x-direction pass sweeping upwards followed by a second y-direction pass sweeping to the right generates satisfactory results with minimum computational effort. Similarly to **step 1**, the initial guess is a zero pressure field.

With the coefficients of **step 2**, the pressure field obtained is used in **step 4** to calculate the 'starred' velocities. Attempts to accomplish this with one or more TDMA iteration resulted in divergence. A single Gauss-Seidel iteration, however, worked well. In an attempt to speed up convergence, the number of iterations was increased. The additional calculations actually slowed down the overall convergence and, when the number of iterations passed a certain threshold, divergence occurred. It is presumed that this behaviour is a consequence of the non-linear nature of the governing equations.

In **step 5**, the mass source b is calculated with **equation 4.1.7.2.10f** and the p' equation is solved. Solution of the p' equation is carried out in a similar manner as that described for the pressure equation: apply one x-direction, line-by-line TDMA pass sweeping upwards, followed by a second y-direction pass sweeping to the right.

The velocity field is corrected in **step 6** by use of **equations 4.1.7.2.7** and **4.1.7.2.8**. **Step 7** does not apply in this simple flow problem since no other dependent variables are considered. **Step 8** directs us to repeat the algorithm via **step 2** until convergence. What the convergence criterion should be is the last difficulty. The solution to this problem is suprisingly simple when one observes that the source term b calculated in **step 5** must approach zero as improved solutions are obtained. This is necessarily so because p' must approach zero as the velocity and pressure fields improve. Consequently, when the maximum $|\bar{b}|$ value is less than some tolerance, the convergence criterion has been met.

With the SIMPLER algorithm constructed as detailed above, converged solutions were obtained at various grid densities, viscosities, and average inlet velocities. Comparison against analytical solutions showed that relative errors of less than 1% can be easily obtained. Lastly, the algorithm was tested with a plug flow inlet boundary condition. When the length to height ratio, L/H, was sufficiently large (in the order of 10), the expected parabolic profile of laminar flow developed near the outlet. The next logical step is the geometric extension of the model to allow for calculation of flow fields in the rectilinear flow cell.

4.3 Steady-State Flow in the Rectilinear Flow Cell

The geometry of the rectilinear flow cell was built into the model. The new grid configuration with the appropriate boundary conditions is shown in **Fig. 4.3.1**. The horizontal entrance and exit sections (of length $L_E = 60H_L$ primarily for display purposes) of the lower chamber have been added to minimize the effects of minor numerical method artifacts on y-velocities near the membrane. In reality, the lower chamber inlet and outlet are perpendicular to the longitudinal axis of the channel: consequently, end effects are assumed to be negligible.

For the most part, the equations used in the previous section apply. However, several additional expressions must be derived to account for flow through the membrane. If we consider a pressure node on the lower surface of the membrane, the associated velocity v_m is given by Darcy's law as:

$$v_n = v_m = \frac{\kappa}{\mu H_m}(P_P - P_N) \equiv \frac{L_P}{\mu}(P_P - P_N). \tag{4.3.1}$$

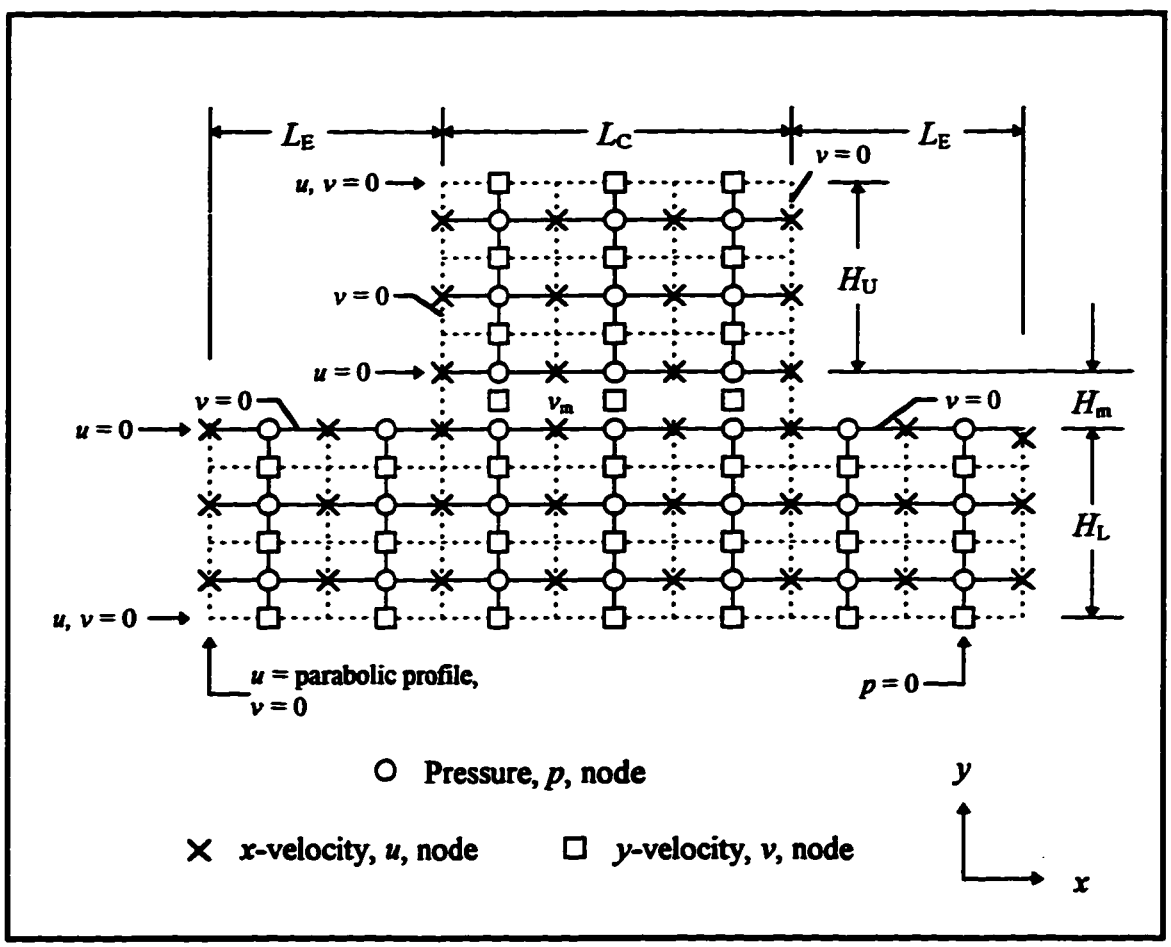

Figure 4.3.1. The grid for the rectilinear flow cell geometry.

All other interfacial velocity components are defined as in **equations 4.1.7.2.13** and **4.1.7.2.14**. Since the x-velocity along the membrane is assumed to be zero, the discretetized steady state form of the equation of continuity becomes

$$\left[(\rho v)_n - (\rho v)_s\right]\Delta x = 0. \tag{4.3.2}$$

Substitution of these velocity component expressions into **equation 4.3.2**, upon rearrangement, gives

$$a_P p_P = a_N p_N + a_S p_S + b, \tag{4.3.3}$$

where

$$a_N = \rho_n \frac{\kappa \Delta x}{\mu H_m}, \tag{4.3.4a}$$

$$a_S = \rho_s \frac{(\Delta x)^2}{a_s}, \tag{4.3.4b}$$

$$a_P = a_N + a_S, \tag{4.3.4c}$$

and

$$b = \rho_s v_s^{\#} \Delta x. \tag{4.3.4d}$$

For a pressure node on the upper surface of the membrane, **equation 4.3.3** can be obtained similarly, with the following modifications:

$$a_N = \rho_n \frac{(\Delta x)^2}{a_n}, \tag{4.3.5a}$$

$$a_S = \rho_s \frac{\kappa \Delta x}{\mu H_m}, \tag{4.3.5b}$$

$$b = -\rho_n v_n^{\#} \Delta x. \tag{4.3.5c}$$

A similar derivation for the pressure correction equation for an upper membrane surface pressure node, using **equation 4.1.7.2.8** and

$$v_s = v_s^{*} + \frac{\kappa}{\mu H_m}(p_S' - p_P') \tag{4.3.6}$$

yields

$$a_P p_P' = a_N p_N' + a_S p_S' + b, \tag{4.3.7}$$

where a_P is defined as in **equation 4.3.4c**, and

$$a_N = \rho_n \frac{\kappa \Delta x}{\mu H_m}, \tag{4.3.8a}$$

$$a_S = \rho_s \frac{(\Delta x)^2}{a_s}, \tag{4.3.8b}$$

$$b = \left[\rho_s v_s^* - \rho_n v_n^*\right] \Delta x. \tag{4.3.8c}$$

Lastly, it can be shown that for a pressure node on the lower membrane surface the following modifications apply:

$$a_N = \rho_n \frac{(\Delta x)^2}{a_n}, \tag{4.3.9a}$$

$$a_S = \rho_s \frac{\kappa \Delta x}{\mu H_m}. \tag{4.3.9b}$$

4.4 Gravitational Effects

The next stage in the development of the 2D model is incorporation of gravitational effects. If we define θ as being the angle above the horizontal, then the acceleration due to gravity in the x and y directions is

$$g_x = g \cdot \mathrm{Cos}(\theta), \tag{4.4.1a}$$

and

$$g_y = g \cdot \mathrm{Sin}(\theta), \tag{4.4.1b}$$

respectively. Inclusion of the gravity force acting on a control volume leads to the following modified forms of **equations 4.1.7.2.7, 4.1.7.2.8, 4.1.7.2.13 and 4.1.7.2.14**:

$$u_e = u_e^* + \frac{\Delta y}{a_e}\left(p_P' - p_E'\right) + \frac{\rho_e g_x \Delta x \Delta y}{a_e}, \tag{4.4.2a}$$

$$v_n = v_n^* + \frac{\Delta x}{a_n}\left(p_P' - p_N'\right) + \frac{\rho_n g_y \Delta x \Delta y}{a_n}, \tag{4.4.2b}$$

and

$$u_e = u_e^* + \frac{\Delta y}{a_e}\left(p_P - p_E\right) + \frac{\rho_e g_x \Delta x \Delta y}{a_e}, \tag{4.4.3a}$$

$$v_n = v_n^* + \frac{\Delta x}{a_n}\left(p_P - p_N\right) + \frac{\rho_n g_y \Delta x \Delta y}{a_n}, \tag{4.4.3b}$$

respectively.

4.5 The Final Extensions

To complete our model, solute species, osmotic pressure effects, transience, as well as density, viscosity, and diffusivity correlations must be included. If small enough time steps are employed, then it is possible to uncouple the Navier-Stokes equations from the mass fraction fields, thereby simplifying computations. This time-lagging and mass fraction field calculation are discussed in the following section.

4.5.1 Osmotically Active Solutes and Transience

The introduction of osmotic species in the upper channel leads to the addition of an osmotic pressure term, calculated with **equation 3.2.1**, in **equation 4.3.1** to give:

$$v_n = v_m = \frac{\kappa}{\mu H_m}\left(P_P - P_N + \Pi_N\right) \equiv \frac{L_P}{\mu}\left(P_P - P_N + \Pi_N\right). \tag{4.5.1.1}$$

As a result, for the pressure equation, **equations 4.3.4d** and **4.3.5c** become, respectively,

$$b = \rho_s v_s^* \Delta x - a_N \Pi_N, \tag{4.5.1.2}$$

and

$$b = a_S \Pi_P - \rho_n v_n^* \Delta x. \tag{4.5.1.3}$$

With these minor modifications, the steady state flow field can be obtained as detailed above.

With the solved flow field, it is now possible to obtain the various solute mass fraction distributions in the upper channel. With $\phi = m_i$ and the source terms, S_C and S_P, set to zero, **equations 4.1.6.1** through **4.1.6.4** are applicable. Additionally, while Γ is the fluid viscosity for flow field calculations, Γ_i becomes the diffusivity of solute i in the calculation of mass fraction fields. The solution procedure may be summarized as follows:

1. The flow field is obtained by solving the Navier-Stokes equations.
2. The total time is incremented and the mass fraction fields are solved. This is accomplished in a similar manner to the solution of the pressure field in **step 1**. For the first solute species, the coefficients for **equation 4.1.6.1** are calculated. The equation is then solved with one x-direction, line-by-line TDMA pass sweeping upwards, followed by a second y-direction pass sweeping to the right. The procedure is then carried out for solutes 2 through n and iterated until all mass fraction fields converge. Convergence is obtained when all species mass fractions at all nodes differ between iterations by less than the set tolerance.
3. With the new mass fraction fields, **steps 1** and **2** are repeated until the total simulated time equals the desired total run time.

4.5.2 Empirical Correlations for Density, Viscosity and Diffusivity

Density, viscosity and diffusivity terms may be calculated with empirical correlations obtained by curve-fitting of experimental and literature data. All empirical equations, obtained with Jandel TableCurve software, have an r^2 of 0.98 or greater.

4.5.2.1 Density

The temperature dependence of the density of pure water between 0°C and 100°C **[45]** can be approximated with the third degree polynomial,

$$\rho_0 = \alpha + \beta T + \delta T^2 + \gamma T^3, \qquad (4.5.2.1.1)$$

where T is the temperature in degrees Celsius and

$$\alpha = 1.00011,$$
$$\beta = 2.79572 \times 10^{-5},$$
$$\delta = -1.17114 \times 10^{-5},$$
$$\gamma = 3.29361 \times 10^{-8}.$$

If we assume that the solutions follow the same temperature dependence trend as pure water, then curve fitting of experimental and literature data [30] gives

$$\rho_{BSA} = \rho_0 + \alpha' C + \beta' C^2 \qquad (4.5.2.1.2)$$

for BSA solutions to 0.156 g/ml, where

$$\alpha' = 1.00011,$$
$$\beta' = 2.79572 \times 10^{-5},$$

and

$$\rho_{Dextran\ 70} = \rho_0 + \alpha'' C + \beta'' C^2 \qquad (4.5.2.1.3)$$

for Dextran 70 solutions to 0.104 g/ml, where

$$\alpha'' = 0.365630,$$
$$\beta'' = 7.9177 \times 10^{-2}.$$

If mixtures of BSA and Dextran 70 are assumed to be obey the ideal mixing rule, then it can be easily shown that

$$\rho_{Mixture} = \frac{m_{BSA}\rho_{BSA} + m_{Dextran\ 70}\rho_{Dextran\ 70}}{m_{BSA} + m_{Dextran\ 70}}.$$

4.5.2.2 Viscosity

The viscosity of pure water between 0°C and 100°C as function of temperature [46] can be approximated with

$$\mu_0 = \left(\frac{\alpha + \delta T}{1 + \beta T}\right)^2, \tag{4.5.2.2.1}$$

where

$$\alpha = 0.133864,$$
$$\beta = 1.87647 \times 10^{-2},$$
$$\delta = 1.89775 \times 10^{-4}.$$

Again, assuming the solute solutions follow the same temperature dependence trend as pure water, then curve fitting of literature data [13, 46] gives

$$\mu_{BSA} = \mu_0 + \alpha' C + \beta' C^2 + \gamma' C^3 + \delta' C^4, \tag{4.5.2.2.2}$$

for BSA solutions to 0.45 g/ml, where

$$\alpha' = -1.24721 \times 10^{-2},$$
$$\beta' = 0.892734,$$
$$\delta' = -6.96505,$$
$$\gamma' = 22.8414.$$

Similarly, for Dextran 70 to 0.22 g/ml, the following relationship may be applied:

$$\mu_{Dextran\ 70} = \mu_0 + \alpha'' C + \beta'' C^2 + \gamma'' C^3 + \delta'' C^4, \tag{4.5.2.2.3}$$

where

$$\alpha'' = 5.85548 \times 10^{-2},$$
$$\beta'' = 10.7794,$$
$$\delta'' = -71.3806,$$
$$\gamma'' = 2.22830 \times 10^{2}.$$

For lack of a better correlation, the following assumption is made. If viscosity contributions are additive, much like densities, the viscosity of a BSA and Dextran 70 mixture can beapproximated with

$$\mu_{Mixture} = \frac{m_{BSA}\mu_{BSA} + m_{Dextran\ 70}\mu_{Dextran\ 70}}{m_{BSA} + m_{Dextran\ 70}}. \tag{4.5.2.2.4}$$

4.5.2.3 Diffusivity

Diffusivities of BSA in solution to 0.46 g/ml and Dextran 70 in solution to 0.22 g/ml at 20°C are given in the literature [30]. Based on these data the following correlations were obtained:

$$D_{\text{BSA, ref}} = \alpha + \beta C + \delta C^2, \tag{4.5.2.3.1}$$

where

$$\alpha = 7.09614 \times 10^{-7},$$
$$\beta = -7.17195 \times 10^{-7},$$
$$\delta = 4.36027 \times 10^{-7},$$

and

$$D_{\text{Dextran 70, ref}} = \alpha' + \beta' \left[1 - Exp\left(\frac{C - \delta'}{\gamma'} \right) \right], \tag{4.5.2.3.2}$$

where

$$\alpha' = 8.07860 \times 10^{-7},$$
$$\beta' = -4.27231 \times 10^{-7},$$
$$\delta' = 5.31691 \times 10^{-2},$$
$$\gamma' = 1.86375 \times 10^{-2}.$$

Temperature dependence of diffusivity has been correlated with solvent viscosity in the following relationship [47]:

$$D_{\text{Species}} = \frac{T + 273.15}{T_{\text{ref}} + 273.15} \cdot \frac{\mu_{\text{Solvent, ref}}}{\mu_{\text{Solvent}}} D_{\text{Species, ref}}, \tag{4.5.2.3.3}$$

where $D_{\text{Species, ref}}$ and $\mu_{\text{Solvent, ref}}$ are the species diffusivity and solvent viscosity, respectively, at the reference temperature, T_{ref}. All other quantities are determined at the desired temperature, T. For a reference temperature of 20°C, **equation 4.5.2.3.3** reduces to:

$$D_{\text{Species}} = \alpha''(T + \beta') \frac{D_{\text{Species, ref}}}{\mu_{\text{Solvent}}}, \tag{4.5.2.3.4}$$

where

$$\alpha'' = 3.41805 \times 10^{-7},$$
$$\beta'' = 273.15.$$

4.6 Parametric Study

With the 2D numerical model for the rectilinear flow cell complete, our attention turns to how various parameters affect the model's performance. The goal of this section is to select numerical parameters that optimize the efficiency of the simulation while generating accurate results.

4.6.1 Time Step Size and Convergence Tolerance

Preliminary trials showed that the time step size (Δt) and convergence tolerance (ε) have profound effects on both the accuracy of the final solution and on the computational time. Since we have no general analytical solution with which we can measure the accuracy of the numerical solutions, a less direct method is employed. A total species balance over the upper channel allows the calculation of the overall solute error. Simply put, some solute is either lost or generated as a result of the numerical approximations used in the model. The goal, then, is to minimize this overall change in solute content. This strategy, when combined with the graphical inspection of transversely averaged concentration profiles, gives an indication of the accuracy of the final solution.

The physical, temporal, and geometric parameters used in the investigation of the effects of Δt and ε on the overall solute error and total computational time are given in **Table 4.6.1.1**. These parameters, unless otherwise indicated, were used in subsequent optimization studies. Additionally, the exponential interpolation scheme was employed (as in all subsequent simulations).

The results of the investigation, for time steps of 5 to 150 s and tolerances of 10^{-4} to 10^{-8}, are presented in **Table 4.6.1.2**. In addition, it was observed that, in general, the total computational time increases as the tolerance and step size are reduced.

Table 4.6.1.1. Parameters used in the time step size and convergence tolerance study.

Parameter	Value
Rectilinear Flow Cell Geometry	
Entrance Section Length, L_E	60 cm
Exit Section Length, L_E	15 cm
Channel Length, L_C	15 cm
Lower Channel Height, H_L	0.25 cm
Upper Channel Height, H_U	0.25 cm
Membrane Thickness, H_m	0.025 cm
Grid Density	
x-direction:	
Entrance Section	20 nodes
Exit Section	20 nodes
Channel	60 nodes
Total	100 nodes
y-direction:	
Lower Channel	50 nodes
Upper Channel	50 nodes
Total	100 nodes
Acceleration due to Gravity, g	981 cm/s^2
Angle above Horizontal, θ	$-\frac{\pi}{2} \equiv -90°$
Temperature, T	25°C
Total Run Time	72 h
Membrane Permeability	
L_p	1.0×10^{-11} cm
Darcy, κ	2.5×10^{-13} cm^2
Average Lower Channel Velocity, $\bar{u}$	25 cm/s
Initial BSA Concentration, C_0	0.01 g/ml (1 %)

Table 4.6.1.2. Total BSA relative error (%) as a function of time step size and convergence tolerance.

Tolerance	Time Step (s)				
	5	10	50	100	150
1E-04	-83.788	-84.966	-85.889	-86.005	-86.048
1E-05	-36.255	-37.440	-38.416	-38.531	-38.557
1E-06	-9.002	-9.377	-9.674	-9.659	-9.583
1E-07	-0.476	-0.522	-0.562	-0.570	-0.576
1E-08	0.445	0.436	0.429	0.429	0.431

Some runs with a tolerance of 10^{-9}, exhibiting rather lengthy computational times, were carried out. As a result, tolerances smaller than 10^{-8} were deemed too computationally costly. From **Table 4.6.1.2**, it appears that the smallest total BSA error is obtained with a tolerance of 10^{-8} and a time step between 50 and 100 s. Consequently, a tolerance of 10^{-8} and a time step of 1 min (somewhat arbitrarily) were chosen for subsequent simulations.

4.6.2 Grid Density

The effect of grid density on solution accuracy and computational time was investigated by varying the number of pressure nodes in both dimensions. In all cases, the nodal ratios in each dimension were preserved: That is, if N_x and N_y are the number of nodes in the x and y directions, respectively, then

$$N_x \text{ (entrance)}: N_x \text{ (channel)}: N_x \text{ (exit) and,}$$
$$N_y \text{ (lower channel)}: N_y \text{ (upper channel)}$$

were kept constant for all runs. The results are summarized in **Table 4.6.2.1**. Several factors must be considered in the choice of the best number of nodes in both directions.

Table 4.6.2.1. Total BSA relative error (%) as a function of grid density.

N_x	N_y		
	10	50	100
10	0.164	0.164	0.212
50	1.240	0.310	0.248
100	4.623	0.886	0.429

The lowest relative errors were obtained with $N_x = 10$. Furthermore, runs with $N_x : N_y$ ratios greater than or equal to 1 required rather long computational times for completion. For ratios less than 1, the computational time increased gradually as more nodes were added in a particular dimension. It would appear, then, $N_x : N_y = 10{:}50$ is the best grid density. However, since this grid density gives only 10 points in the x direction, plots tend to be fairly coarse. Also, under other conditions (for example, with higher membrane permeabilities) the x direction grid density may be insufficient in obtaining accurate results. Consequently, a grid density of $N_x : N_y = 50{:}100$ was selected for subsequent runs. Of course, we could conduct many more runs under other conditions and with other intermediate grid densities to optimize the grid, but this would be quite time-consuming.

4.6.3 Adaptive Time Stepping

As discussed above, the time step size is one factor influencing solution accuracy and computational time. The use of time steps that are too small results in long computational times and may in fact introduce error, presumably due to greater cumulative truncation errors. While the total time of computation can be drastically reduced with very large time steps, the solution accuracy suffers. However, under certain conditions, fairly large time steps can lead to lengthy computational times. The selection of the optimum time step is complicated by factors such as flow conditions, cell geometry,

and grid density. For example, higher membrane permeabilities necessitate the use of smaller time steps. What we need is some heuristic or algorithm to determine the optimum time step under any set of conditions.

Exploratory numerical simulations showed that for very large time steps, most of the computational effort is expended in recalculating the flow field. This makes perfect sense since the mass fraction field changes significantly only over relatively large time periods. Such a change in the mass fraction field, in turn, results in large changes in the flow field, requiring many iterations in the solution of the Navier-Stokes equations. On the other hand, small time steps lead to the unnecessary recalculation of the flow field after negligible changes are made to the mass fraction field. With these observations in mind, the following adaptive time stepping algorithm was devised:

1. Begin with a relatively small time step of, say, 1 s.
2. Calculate the flow field. If more than 1 iteration is required for convergence, halve the time step size. Otherwise, double the time step size.
3. Calculate the mass fraction field(s) and proceed to step 2 until the total time equals the desired total run time.

Table 4.6.3.1 shows that for all run times of 14 days or less, simulations with adaptive time stepping yield lower relative errors in BSA mass than those with 60 s time steps. The absolute, normalized (with respect to the initial concentration) difference in predicted BSA concentrations using a simulator with fixed time steps (60 s) and one utilizing adaptive time steps is presented in **Fig. 4.6.3.1**. As the run time increases, the nodal concentration differences tend to increase, particularly at the downstream end of the flow cell. For run times of 14 d, the concentration differences are small but significant. Based on the results, it is difficult to determine which simulation is more accurate. Simulations with run times of 7 d or less exhibit very small concentration differences. Thus, the adaptive time stepping algorithm is at least applicable for short to moderately long run times.

Table 4.6.3.1. Total BSA relative error (%) as a function of total run time for 60 s and adaptive time steps.

Time	Total Run Time (d)						
Step	0.5	1	2	3	6	7	14
60 s	0.008	0.017	0.034	0.053	0.113	0.134	0.318
Adaptive	0.006	0.015	0.035	0.049	0.053	0.044	0.213

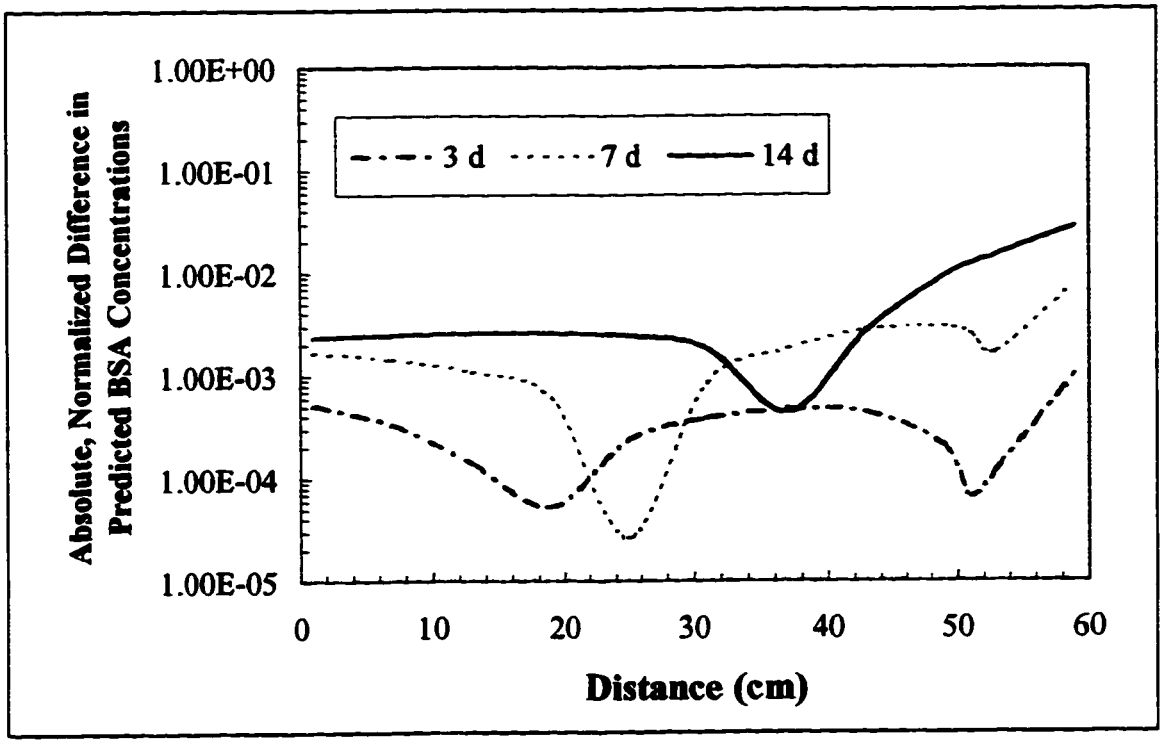

Figure 4.6.3.1. Absolute, normalized (with respect to the initial concentration) difference in predicted BSA concentrations using simulator with fixed time steps (60 s) and one utilizing adaptive time steps. Results for 3 different run times (3 d, 7 d, 14 d) are presented.

4.7 Preliminary Verification of the Model

Partial verification of the numerical model for the rectilinear flow cell was accomplished in two ways. The first test of the model's validity involved inspection of the membrane fluid velocities. At time zero, a momentum balance indicates that there must be symmetry about the longitudinal axis of the membrane. That is, the absolute value of the velocities along the first half of the membrane must exactly mirror the absolute value of the velocities along the second half. This was indeed observed for simulations with various permeabilities and average lower channel inlet velocities.

For laminar flow between semi-infinite parallel plates, it can be shown that the velocity and pressure profiles are given by

$$u = 6\bar{u}\frac{y}{H_L}\left(1-\frac{y}{H_L}\right) \quad \text{and} \quad v = 0, \tag{4.7.1}$$

$$p_x = \frac{12\bar{u}\mu}{H_L^2}(L-x) + p_L, \tag{4.7.2}$$

where H_L is the plate separation and, p_x and p_L are the pressures at position x and some reference position L, downstream. If the membrane permeability is set to zero and the side wall effects are assumed to be negligible, then the parallel plate geometry is obtained in the lower channel of the flow cell. The error in numerical solutions of flows in this geometry can be determined by comparison against analytical solutions (**equations 4.7.1** and **4.7.2**).

Maximum simulation errors are plotted against convergence tolerances in **Figs. 4.7.1** and **4.7.2**. An acceptable maximum error of 1 % for pressure and x-velocities is obtained with tolerances of 10^{-7} and smaller. In addition, the maximum errors for x- and y-velocities level off at minima for tolerances less than approximately 10^{-7}, indicating that the use of very low tolerances is not worth the additional computational effort. Thus, these results imply model validity and support the selection of the 10^{-8} tolerance.

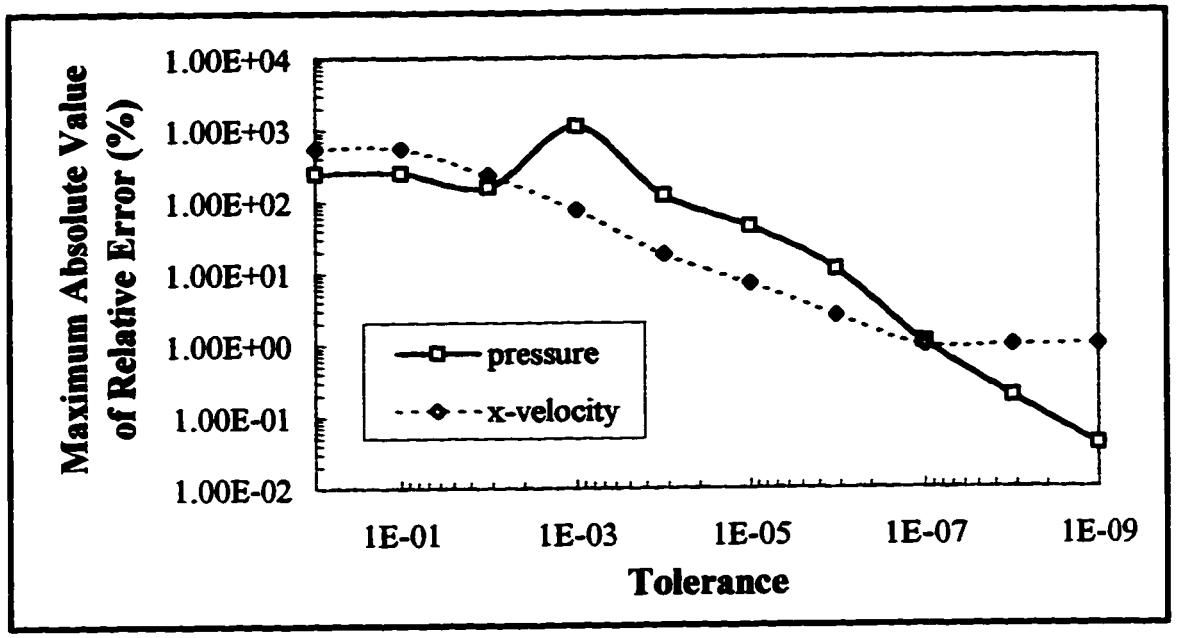

Figure 4.7.1. Maximum absolute value of the relative error of pressures and x-velocities for parallel plate flow simulations at different convergence tolerances.

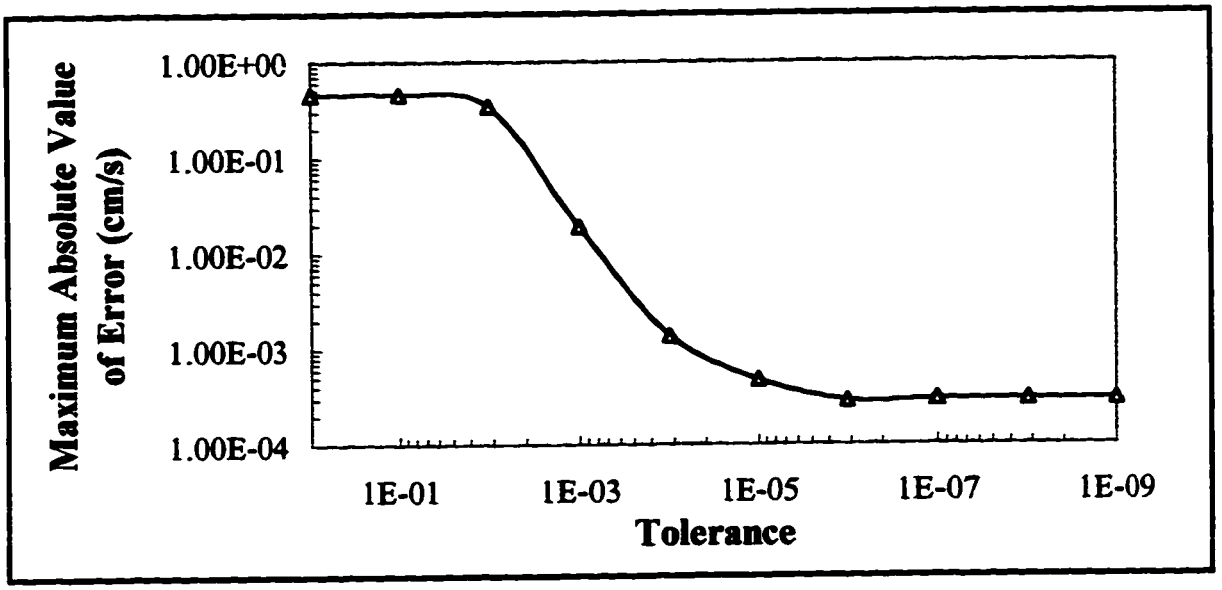

Figure 4.7.2. Maximum absolute value of the error of y-velocities for parallel plate flow simulations at different convergence tolerances.

4.8 Convergence and Model Performance

In this section, two issues are addressed: Model performance and what is loosely termed the 'low permeability problem'. Model performance refers to the overall convergence rate. As noted above, the convergence rate is influenced by many factors, each interacting with the others.

It is useful to make an analogy at this point. The computational domain may be likened to a multi-dimensional landscape through which a traveler moves. The traveler ambles toward the final destination, the solution, navigating with the rules of an algorithm. How quickly the traveler reaches the goal depends on his initial location and the nature of the landscape. Consider two travelers: One begins his journey at a location far away from the ultimate destination while the second starts very close to the goal. All things being the same, we might expect the latter to reach the goal first. However, the landscape may be such that our 'closer' traveler must first negotiate obstacles, and in doing so, must move far away from the final destination. This may be exactly what happens when a good approximation of the flow field is used as an initial guess: convergence sometimes occurs later than when a zero field is employed as the starting point.

When high average velocities are used in simulations, performance may degrade significantly. As noted earlier, the problem can be exacerbated with certain grid densities. In such cases, the computational landscape may have so many obstacles that our traveler essentially becomes bogged down near one location for extended periods of time. The problem lies in the non-linearity of the system to be solved and our attempts at approximation through linearization. To speed up the solution process, then, we can reduce the size and number of obstacles through careful selection of the grid density.

How else can we help out our weary traveler and improve the model's performance? One approach investigated was the use of relaxation factors. This can be something like giving our traveler a high-powered pogo stick. Of course, this is not

without its risks: While the traveler may be able to get over larger obstacles, he may not have as much control. That is, divergence may result. The relaxation scheme coded into the flow field calculation section of the model is given by

$$\phi_P = \phi_P^* + \sigma\left(\frac{\sum a_{nb}\phi_{nb} + b}{a_P} - \phi_P^*\right), \tag{4.8.1}$$

where σ is the relaxation factor. When σ is between 0 and 1, its effect is underrelaxation because ϕ_P remains closer to ϕ_P^*. As expected, underrelaxation tended to slow down the convergence rate. Better results, under certain conditions, were obtained with overrelaxation, with σ between 1 and 1.1. However, performance gains were relatively small. For the most part, bigger relaxation factors resulted in divergence. Since there are no general rules for selecting the optimum value of the relaxation factor, exploratory computations for the given problem must be carried out. As a result, the use of a relaxation factor was deemed impractical, at least for the geometry of the rectilinear flow cell.

We now turn to the 'low permeability problem', the nature of which is summarized as follows. When a realistic membrane permeability is used in the calculation of the initial flow field, an inaccurate solution is obtained on convergence. The details as to why this occurs are not perfectly clear, but round-off and truncation errors are likely the cause. With realistic permeabilities, membrane fluid velocities are 8 or more orders of magnitude smaller than x-velocities in the lower channel. Furthermore, pressure values are typically 2 to 3 orders of magnitude larger than the absolute value of the x-velocities. It is not surprising that errors arise and lead to misleading solutions. Introduction of scaling factors or use of dimensionless groups might solve the problem, but these approaches would require the reworking of the numerical model and subsequent testing. Instead, a wholly satisfactory work-around was developed. Initially, the flow field is calculated with a large permeability ($L_p = 4 \times 10^{-9}$ cm). The permeability is then decreased by at most one order of magnitude and the flow field is recalculated. The process is repeated until the desired permeability is obtained. The mass fraction fields can then be calculated as usual.

4.9 The Simulation Program

The 2D numerical model, programmed in FORTRAN 77, consists of roughly 6000 lines of code. The key features of the program are given below.

- **Data input from file or console.** Geometric, physical, and other variables can be either read in from a data file (INPUTS.DAT) or can be entered at runtime.

- **Pseudo-command line.** The pseudo-command line, as shown in **Figs. 4.9.1** and **4.9.2**, allows the user to display and change parameters, and display plots at runtime. In addition, solutions can be saved to files and, subsequently, read in for inspection and further calculations. For convenience, command menus can be accessed by pressing the 'Enter' key.

- **Multiple solute capability.** Provided enough random access memory is available, simulations with more than one solute species can be carried out. Density, viscosity, diffusivity, and osmotic pressure correlations for BSA and Dextran 70 are incorporated in the code. Correlations can be added for other solutes.

- **Graphical plotting interface.** With the Watcom graphical libraries, a graphical interface for plotting solution results was developed. Pressures, velocities, mass fractions, and pressure source terms (b) can be plotted at runtime. Three types of plots are available: contour plots (**Figs. 4.9.3, 4.9.4, and 4.9.5**) display distributions within the flow cell, cross-sectional plots (**Figs. 4.9.6, 4.9.7, and 4.9.8**) show profiles along the x- and y-directions, and total velocity vector plots (**Fig. 4.9.9**). In these figures, the main flow direction is to the right. The direction in which gravity acts is indicated by the line in the upper left-hand box; the red tip is equivalent to an arrowhead. Additionally, no units are given in the plots. In all cases, consistent units must be used.

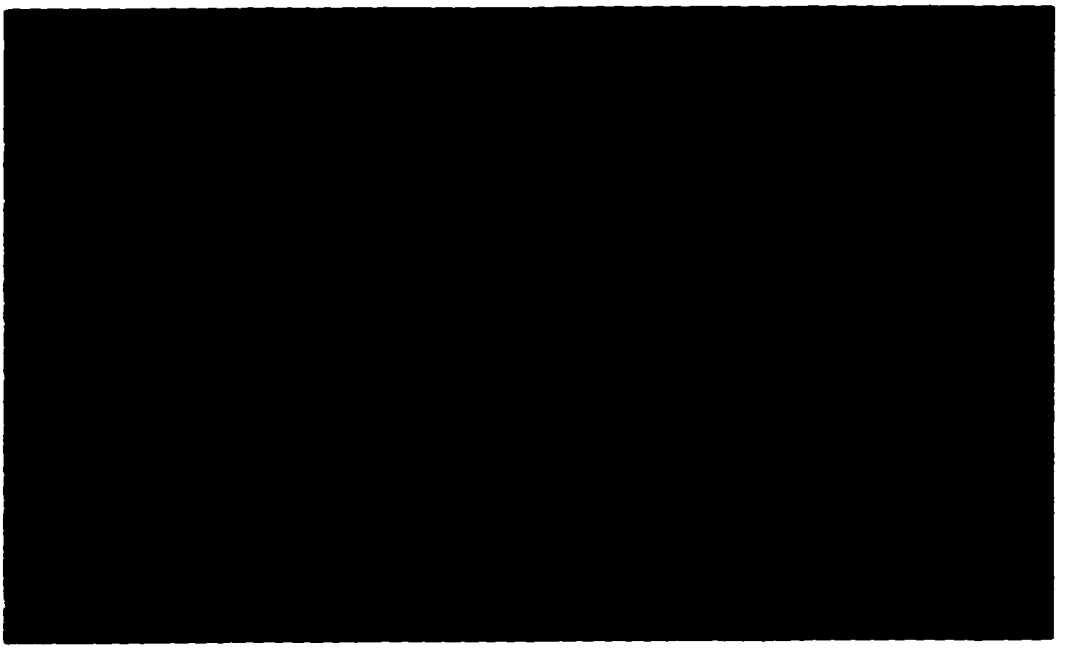

Figure 4.9.1. The main command menu.

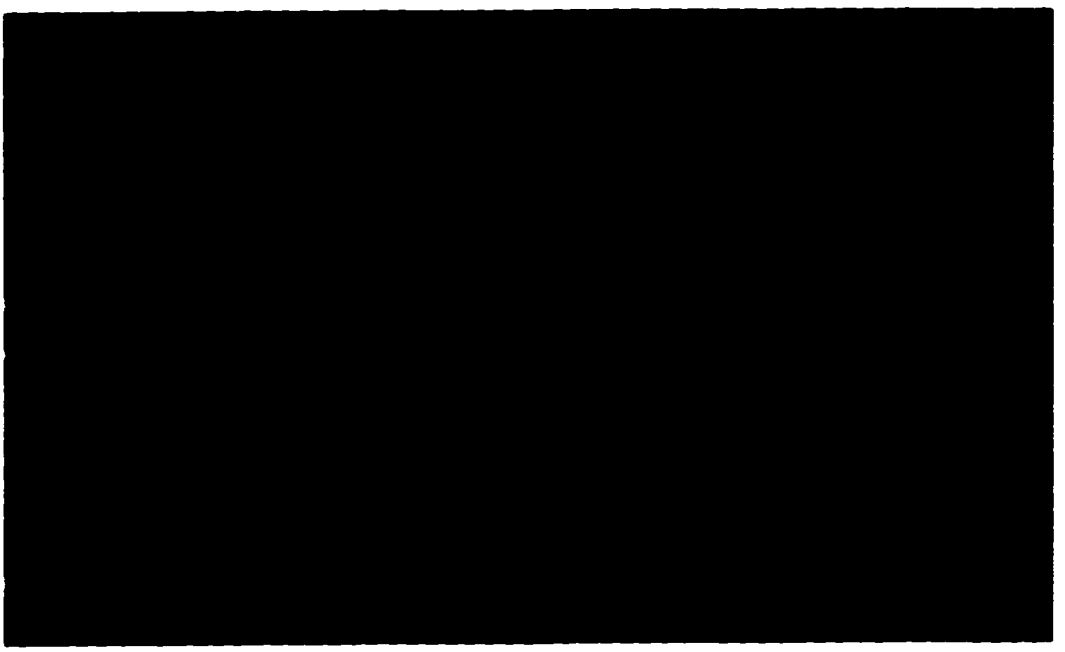

Figure 4.9.2. The plot command menus.

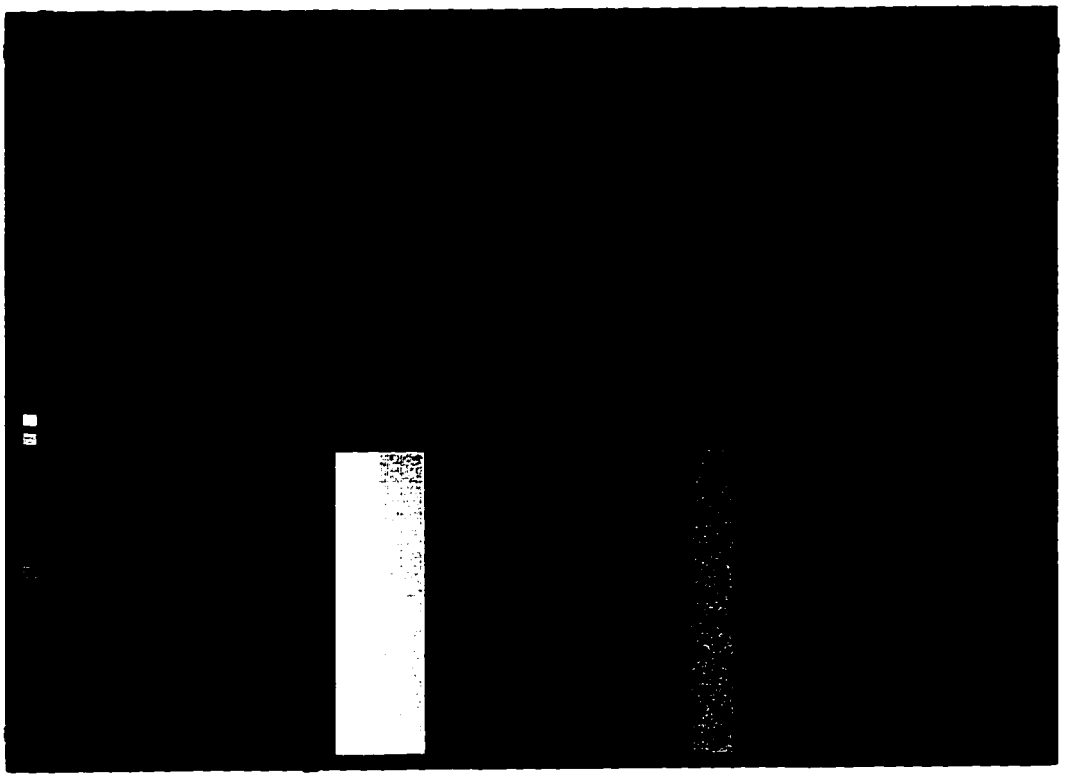

Figure 4.9.3. The pressure distribution.

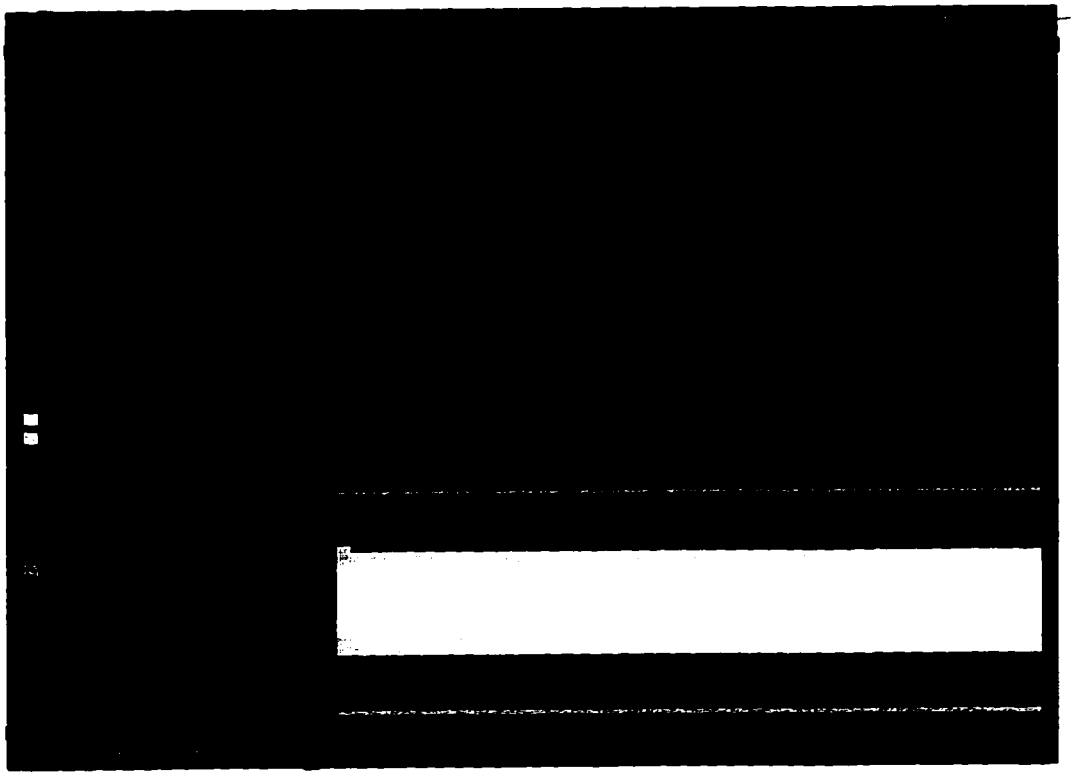

Figure 4.9.4. The x-velocity distribution.

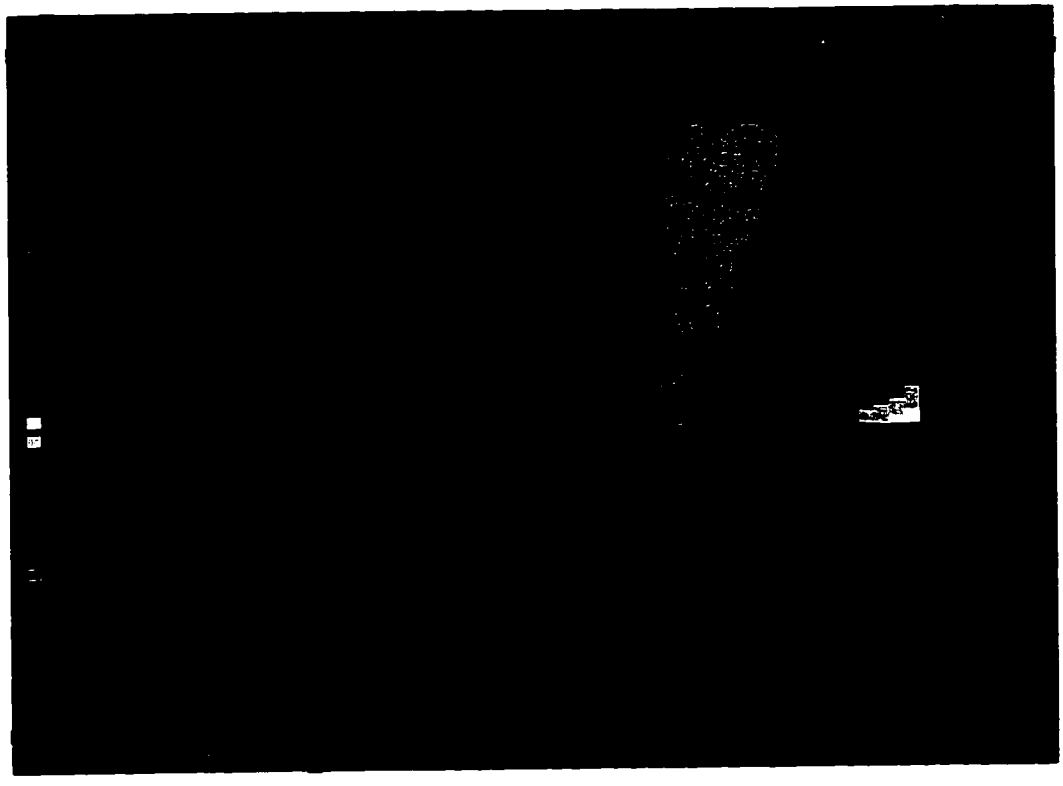

Figure 4.9.5. The BSA mass fraction distribution.

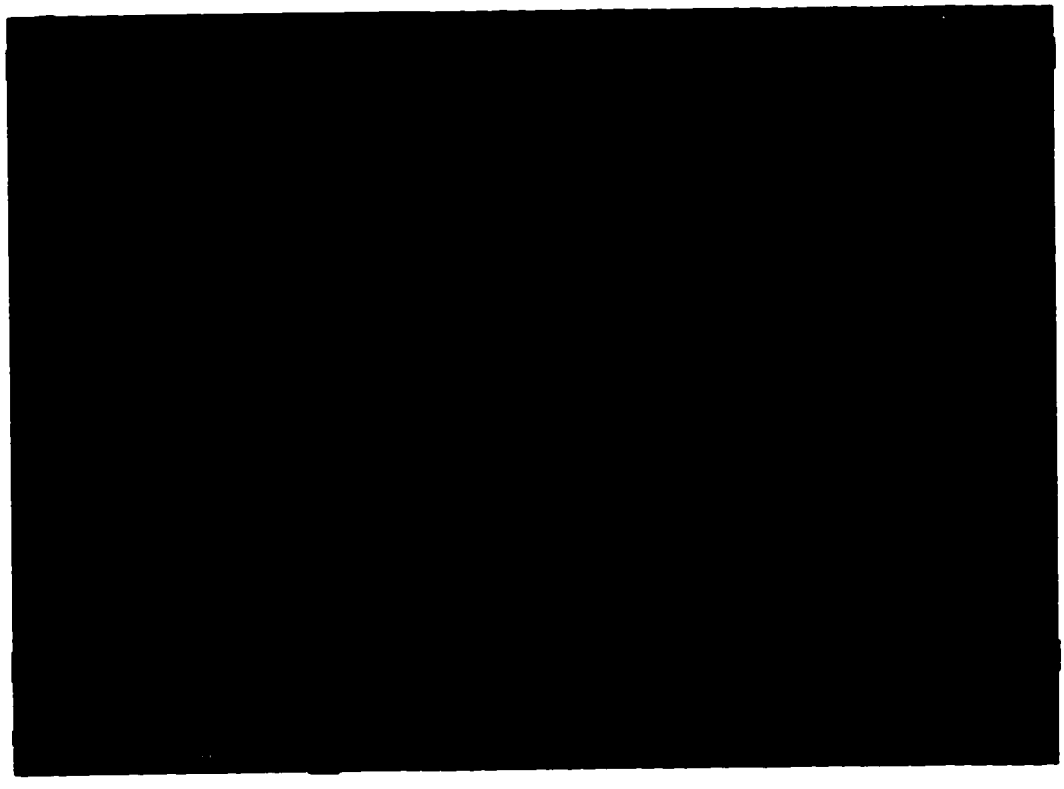

Figure 4.9.6. The BSA mass fraction profile along the membrane.

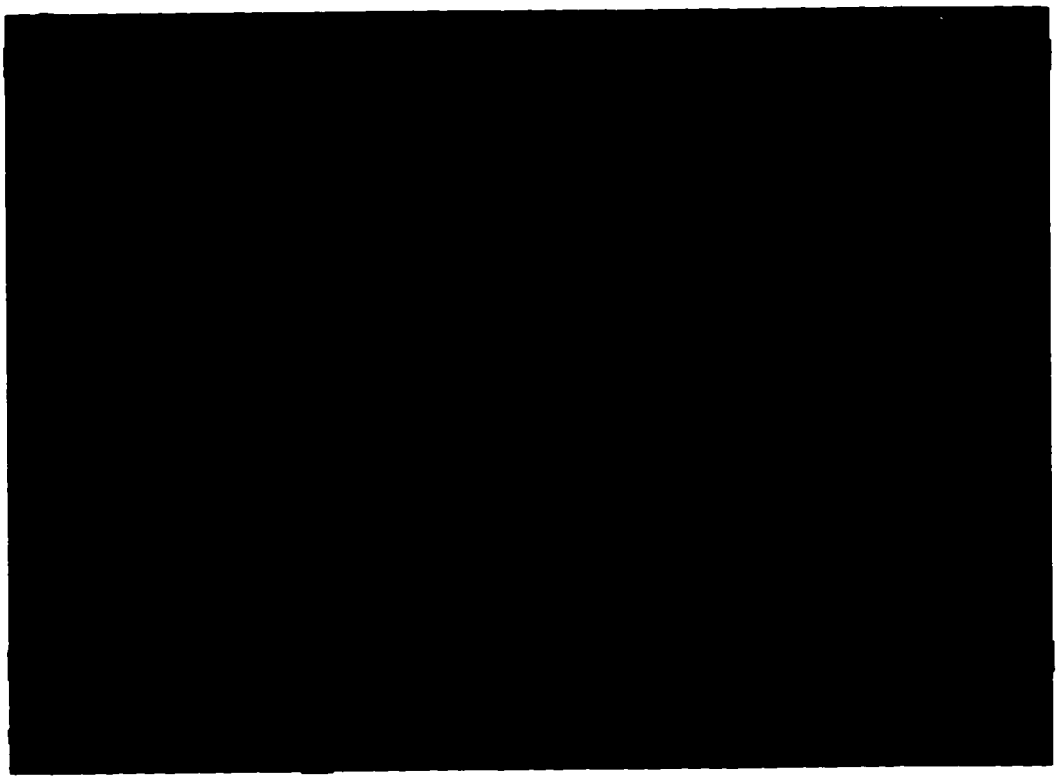

Figure 4.9.7. The membrane fluid velocity profile.

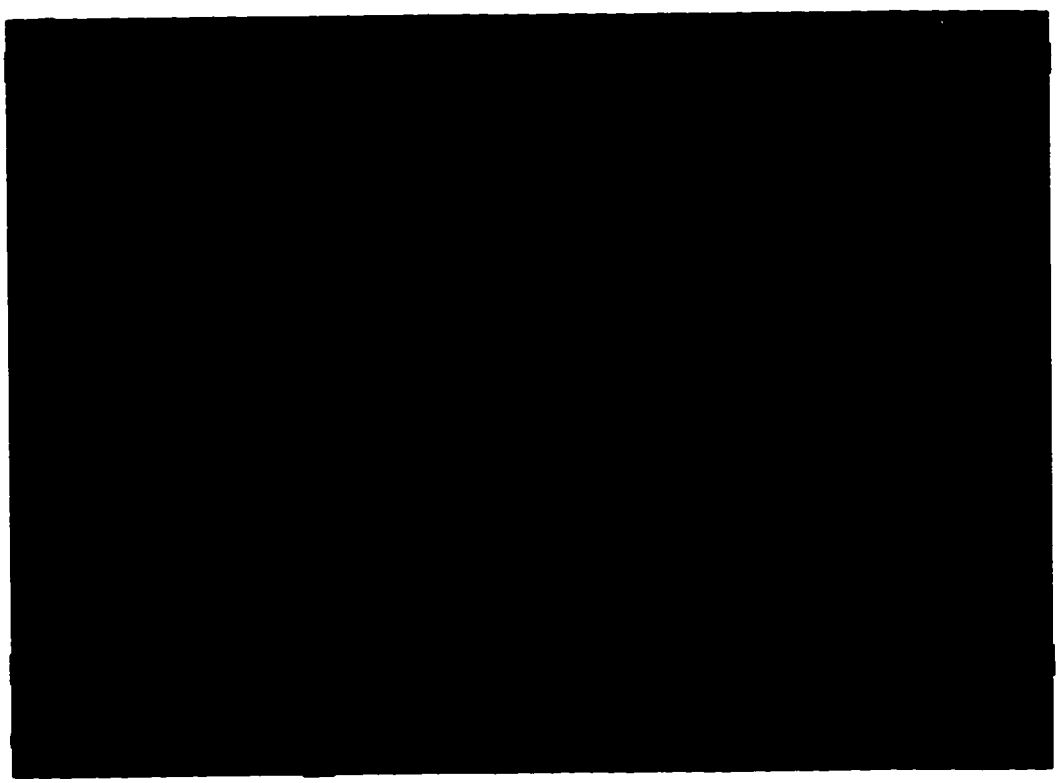

Figure 4.9.8. The x-velocity profile at the longitudinal center of the flow cell.

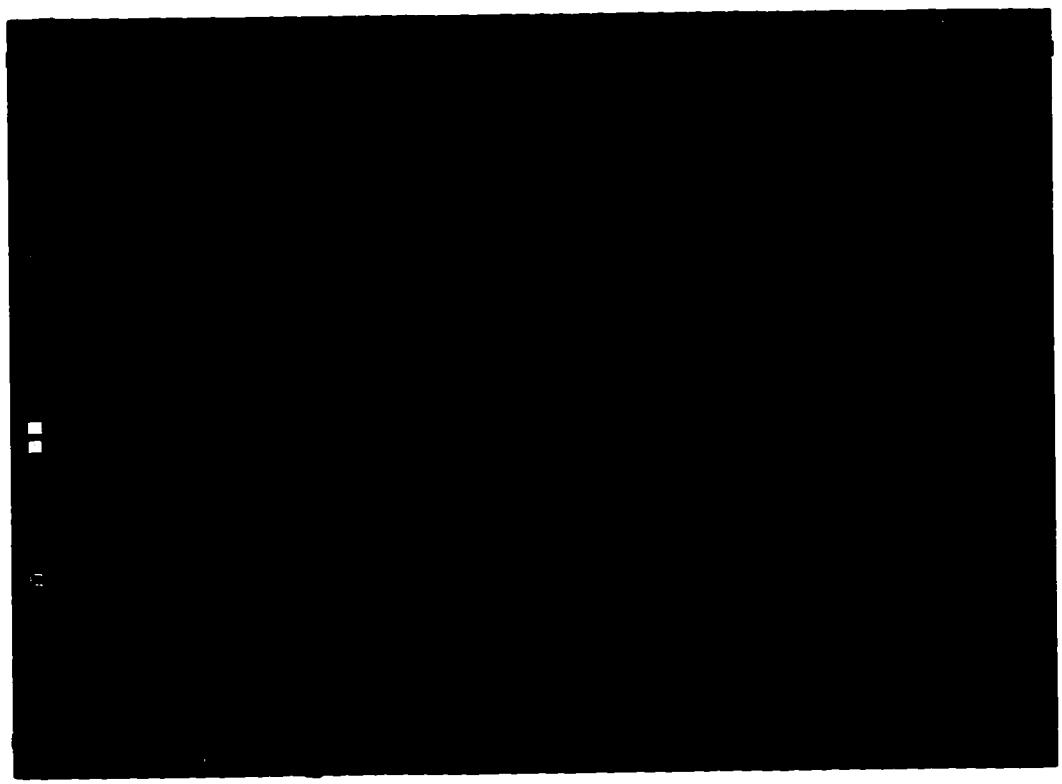

Figure 4.9.9. Total velocity vectors in the upper channel.

Chapter 5

Results and Discussion

5.1 Initial Experimental Difficulties

Exploratory experimental runs were hampered by fluid leakage from sample ports, inlet and outlet fittings, as well as the sides of the flow cell. After the flow cell was redesigned and rebuilt, further tests suggested that all leaks had been stopped. It should be noted that, for these tests, silicone glue was used to seal the membrane within the flow cell. HPLC analysis of the upper channel fluid consistently indicated the loss of protein. Analysis of the buffer solution circulated through the lower channel revealed the presence of BSA. Clearly, the silicone gasket was allowing fluid exchange between the channels. Attempts to remedy the problem through careful application of the glue were only occasionally successful. Furthermore, the use of silicone glue made disassembly of the flow cell difficult at best. The use of room temperature vulcanization (RTV) rubber solved the latter problem, but did not satisfactorily resolve the leakage issue. A properly installed Parafilm® gasket, as detailed in **Chapter 2**, allowed for easy disassembly and prevented fluid exchange between channels. Although no BSA was found in the lower channel fluid, a drop in the initial BSA concentration was observed over time in the upper channel under no-flow conditions. Since no other sources of leaks could be found, another avenue was explored. It was noted that the upper channel inlet and outlet fittings contained air bubbles upon protein loading . It was hypothesized that, due to the osmotic activity of BSA, fluid from the lower channel diluted the protein solution in the upper channel, compressing the air bubbles in the process. When all air bubbles were purged from the system, the problem was eliminated.

With the flow cell difficulties rectified, a partial factorial experimental design was constructed to investigate the effects of the initial BSA concentration, average lower channel fluid velocity, and total run time, on protein polarization. At the same time, development of the 2D model was begun. Initial experimental results for run times up to 24 h showed no discernible polarization. The partial factorial design was abandoned and longer experimental runs were conducted. At about the same time, a simplified 2D model

was completed. For the experimental conditions used, simulations indicated runs of at least 3 days (and, probably closer to 7 days) are required for observable polarization to occur.

5.2 Membrane Permeability

Before the experimental and numerical results can be evaluated, the results of the *in situ* membrane permeability determination must be considered. As indicated by the data of **Fig. 2.3.9.2**, a permeability of 3.33×10^{-13} cm was obtained for the cellulose acetate membrane before and after conditioning with 0.099 to 1.49 % BSA solutions. This value is roughly one order of magnitude smaller than that reported for a similar cellulose acetate membrane [5]. This finding is not particularly surprising. While the membrane used was made by the same manufacturer, and had the same designation and molecular weight cut-off range as the one used by Bhola [5], commercial membranes can vary greatly from batch to batch, and even within batches. Furthermore, Bhola reported a decrease in permeability after conditioning with BSA. As opposed to the *in situ* determination used here, a coupon sampling technique was employed. Close examination of Bhola's data revealed that membrane coupons, prior to conditioning, had permeabilities of 1.8×10^{-12} cm to 7.4×10^{-12} cm [5]. Post-conditioning, coupon permeabilities of 1.7×10^{-12} cm to 5.8×10^{-12} cm were obtained [5]. Because of the large variations in these data, no firm conclusions can be drawn regarding the effect of BSA conditioning. The advantage of the *in situ* procedure is that it gives the average permeability of the membrane actually used in the flow cell. Additionally, the data obtained exhibit less variation (as compared to the coupon sampling method) and suggest BSA conditioning has little or no effect on membrane permeability. It is possible, though, that BSA is weakly adsorbed and is flushed from the surface of the membrane during the permeability determination.

As the pressure drop across a membrane is increased, membrane compaction results in a reduction in the average pore size and permeability which, in turn, translates

into a drop of water flux across the membrane. A subsequent gradual release of the pressure is accompanied with a rise in membrane permeability. This phenomenon is termed hysteresis and, for the most part, is reversible. Furthermore, some membrane compaction at high pressures is irreversible. In practice, the hysteretic effect and irreversible compaction occur at much higher pressures than those encountered in the rectilinear flow cell [5, 28]. Therefore, the effect of pressure on membrane permeability can be assumed negligible here.

Lastly, membrane aging and susceptibility to microbiological attack can effect the permeability of a membrane. Cellulose acetate membranes have reasonable hydrolysis and compaction characteristics, and typical useful lifespans of several years. Practical temperature and pH operating ranges for these membranes are 0 to 30°C and 4.0 to 6.5, respectively. For shorter application times, useful pH ranges of 3 to 8 have been reported [48]. However, cellulose acetate membranes are susceptible to microbiological attack, particularly at higher temperatures [48]. Unused membranes can be stored indefinitely in a cool, dry environment. In the experiments conducted here, aseptic techniques and the use of the bacteriostatic agent, sodium azide, minimized microbiological degradation of the membrane. After 5 months of operation, no noticeable change was observed in the permeability of the membrane used in the flow cell. This finding is consistent with those reported by Bhola [5].

5.3 Experimental and Numerical Results

Experimental and numerical results are plotted in **Figs. 5.3.1** through **5.3.3**. The experimental data of **Figs. 5.3.1** and **5.3.2** are averages of three horizontal runs, 3 and 7 days in duration, with error bars being two standard deviations from the mean. The data of **Fig. 5.3.3** represent a single 9 day run in the vertical orientation with the buffer flowing downwards.

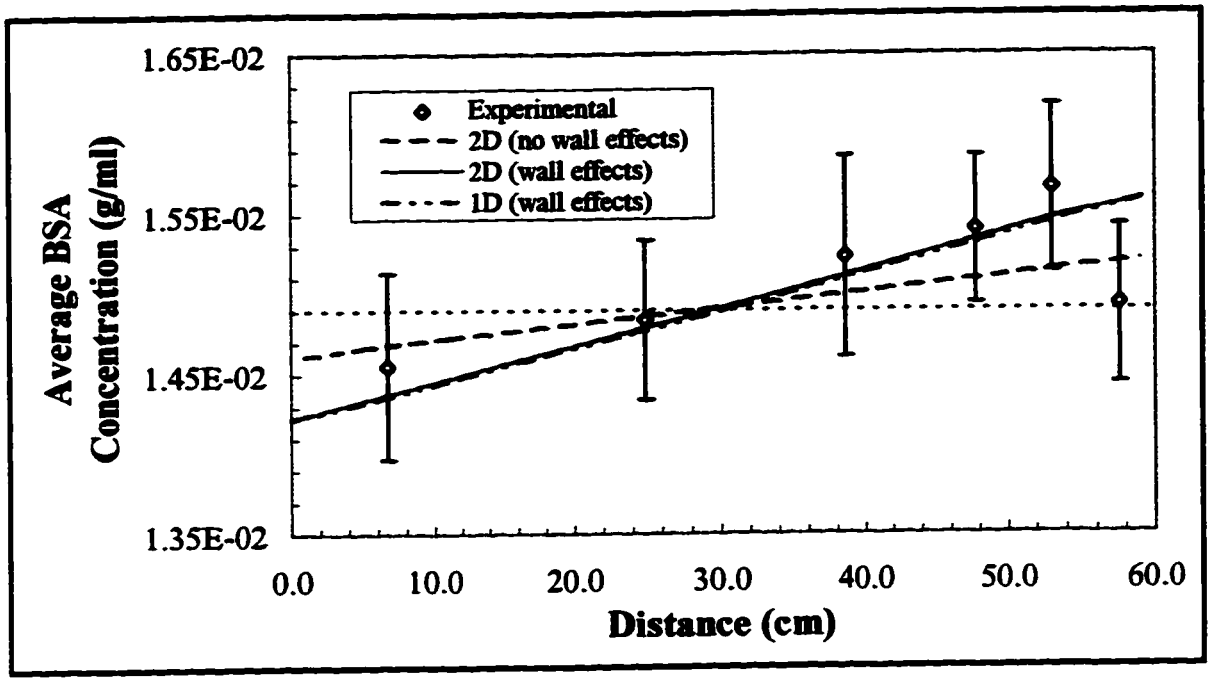

Figure 5.3.1. Experimental and numerical results for 3 day BSA polarization runs ($\bar{v}$ = 10.0 cm/s, C_0 = 0.0149 g/ml, horizontal operation).

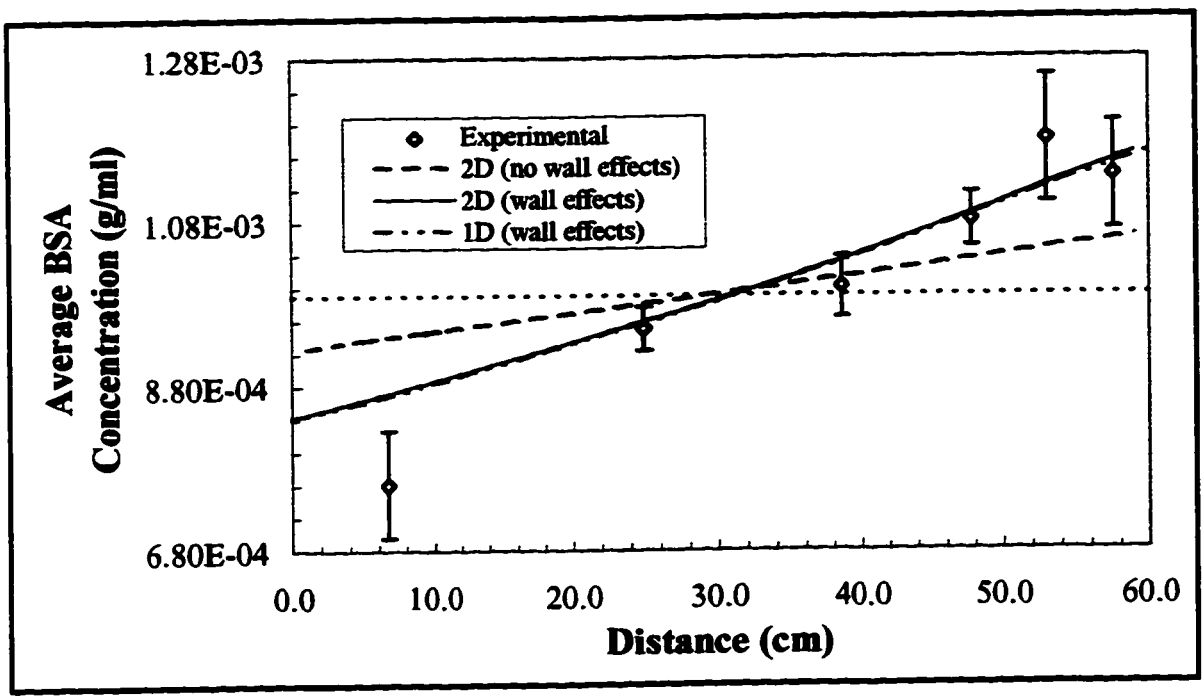

Figure 5.3.2. Experimental and numerical results for 7 day BSA polarization runs ($\bar{v}$ = 15.0 cm/s, C_0 = 0.00099 g/ml, horizontal operation).

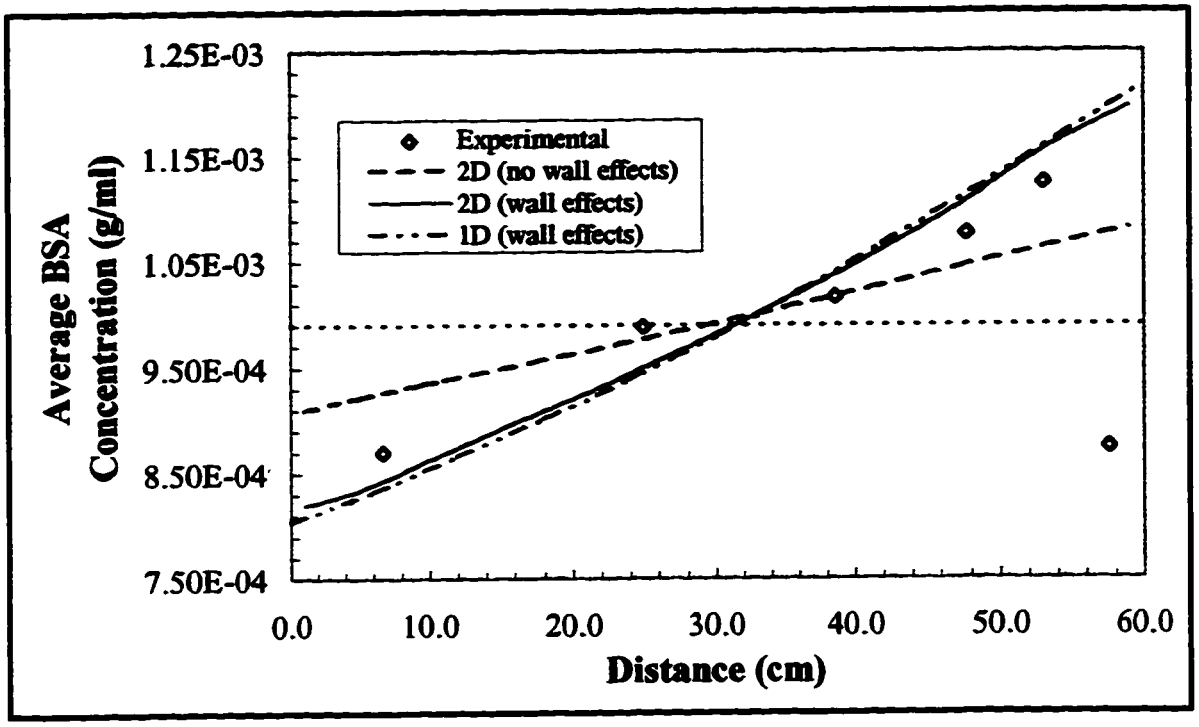

Figure 5.3.3. Experimental and numerical results for one 9 day BSA polarization run ($\bar{v}$ = 15.1 cm/s, C_0 = 0.00099 g/ml, vertical operation).

As can be seen from **Fig. 5.3.1**, 3 day runs, with an average lower channel inlet velocity of 10.0 cm/s, result in negligible BSA longitudinal polarization, the average maximum BSA concentration increasing by approximately 5 % from the initial concentration of 0.0149 g/ml. More significant protein redistribution was observed with 7 and 9 day runs in which the average velocity was increased to roughly 15 cm/s. With the longer runs, concentration changes at the other end of the flow cell varied between -12 % and +23 % from the starting BSA concentration of 0.00099 g/ml.

In all cases, the protein concentration rises gradually along the length of the upper channel, with the exception of the most downstream point. A drop in the concentration is consistently observed near the outlet end of the flow cell. This phenomenon is likely a consequence of end effects. The lower channel inlet and outlet are oriented perpendicularly with respect to the long axis of the channel. However, for simplicity, the

geometry used in the 2D model was constructed such that the inlet and outlet are parallel with the long axis. Consequently, the 2D model is not expected to accurately predict the end effects encountered in the rectilinear flow cell.

Because of the inlet and outlet configurations, fluid flow changes direction by 90 degrees near the lower channel ports. Consequently, regions of high pressure are expected to exist at the ends of the this channel. Such a region at the downstream end of the flow cell would hinder transmembrane flow, thereby reducing the convective transport of protein in the upper channel and inducing a zone of stagnation. Diffusive transport of BSA would predominate in this stagnant area, elevating the BSA concentration slowly above the initial value. For the 9 day run, the concentration at the most downstream sampling port is below the initial 0.00099 g/ml. It is likely that this data point is in error, presumably due to sampling errors. In all other runs, the concentration at this position is greater than or equal to the starting concentration.

To verify that the postulated high pressure regions occur at the lower channel ends, Computational Fluid Dynamics Research Corporation's CFD-ACE software was used to simulate 2D flow in a sharp 90 degree bend under typical experimental conditions. The velocity fields and pressure distributions of **Figs. 5.3.4** and **5.3.5**, respectively, show the presence of recirculation regions and their associated pressure extrema. As expected, a high pressure zone exists in close proximity to where the membrane would be in the flow cell. In addition, end effects in the flow cell are likely to be greater than those simulated here because the fluid ports are cylindrical and open up into a rectangular duct.

Three numerical curves are plotted with the experimental data. The first curve in each figure was generated with the 2D model described above. In constructing the model, a semi-infinite parallel plate assumption was made. This simplification assumes that the side walls of the channels have negligible effects on flow cell hydrodynamics. The consequence of this assumption is particularly evident in **Figs. 5.3.2** and **5.3.3**. Clearly, the model appears to underestimate the degree of BSA polarization.

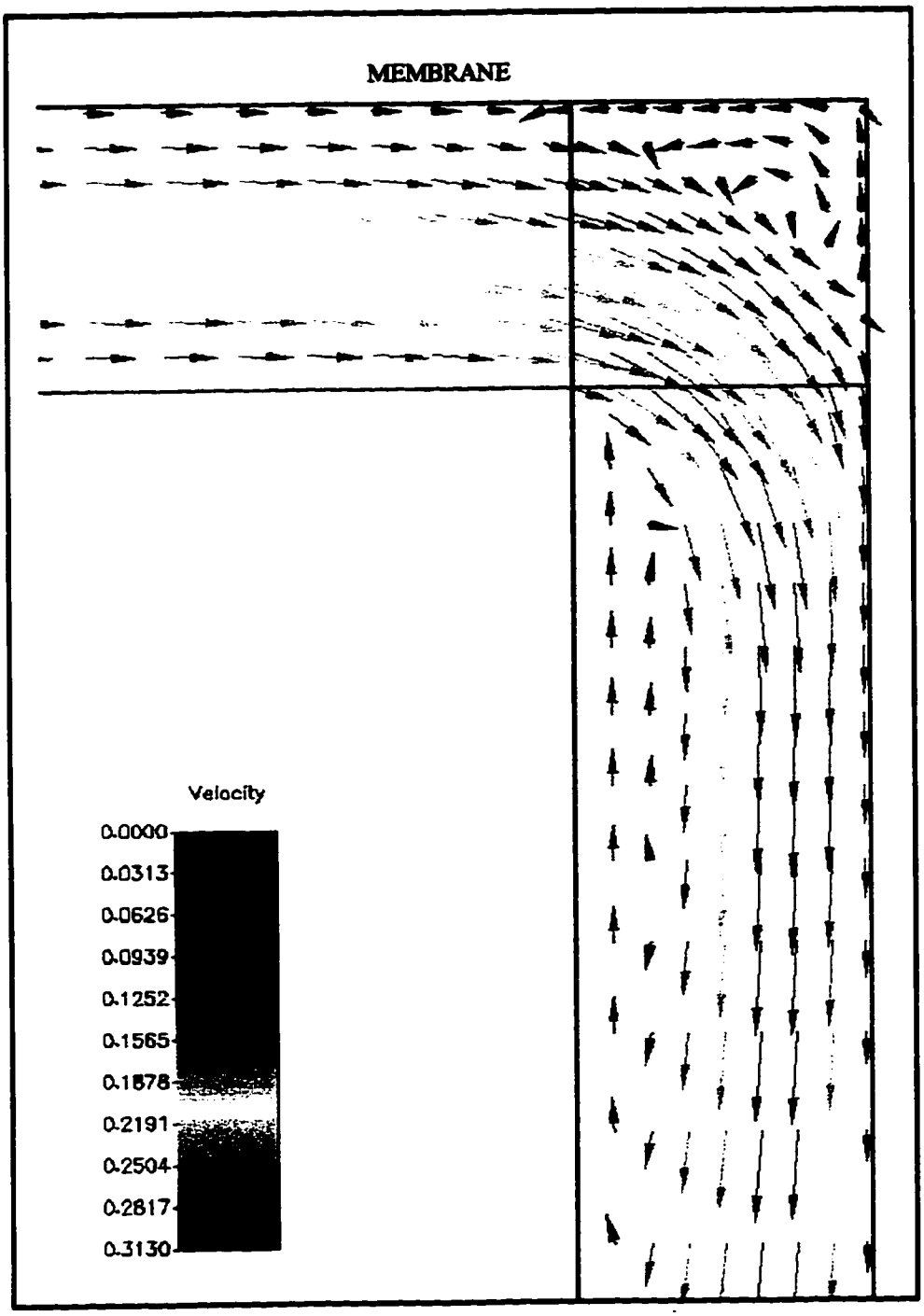

Figure 5.3.4. CFD-ACE model simulation velocity field for an average inlet velocity of 15 cm/s. Velocity vectors are in m/s.

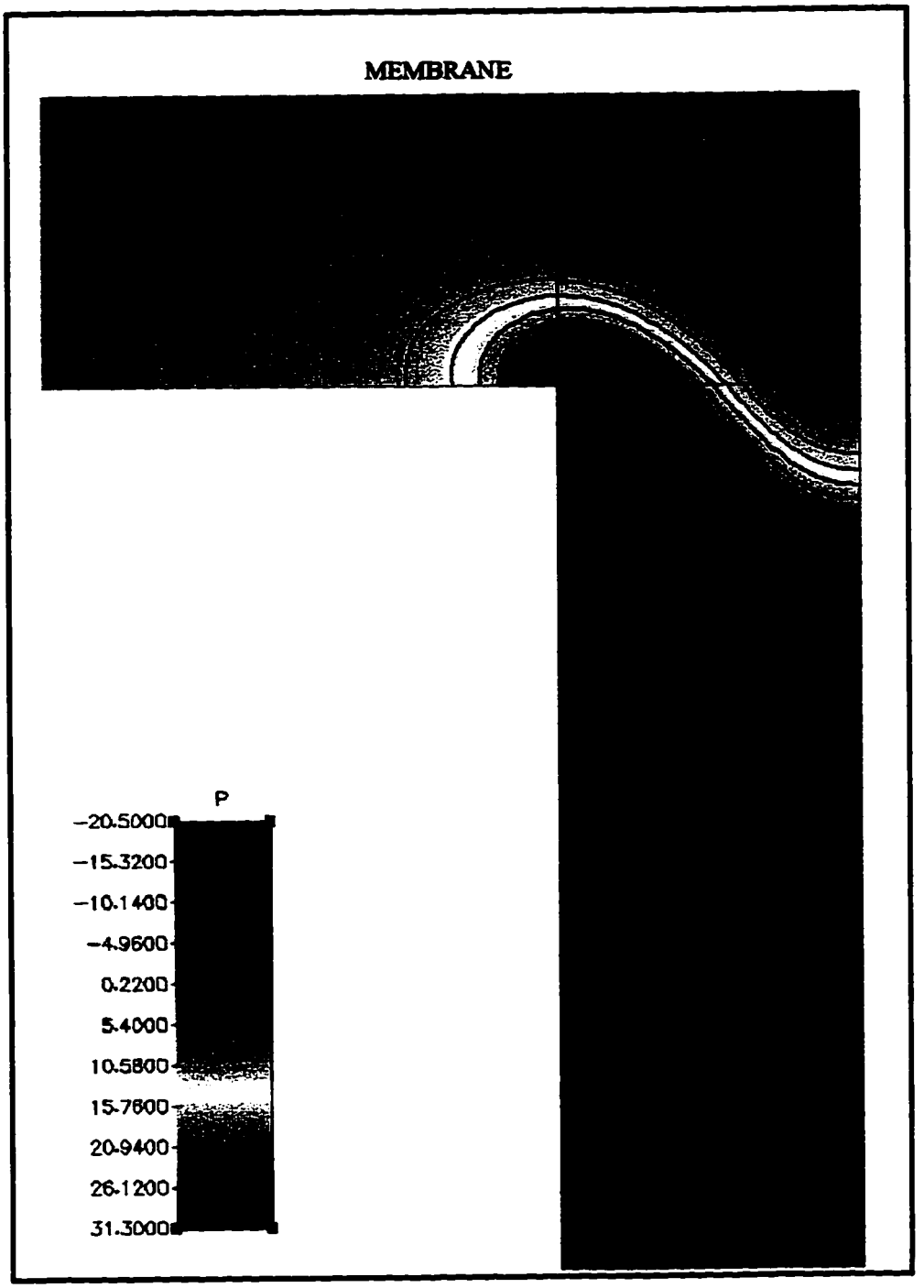

Figure 5.3.5. CFD-ACE model simulation pressure field for an average inlet velocity of 15 cm/s. Pressures are in Pa.

The average pressure drop for fully developed flow through a rectangular duct having cross-sectional dimensions W and H_L is given by [46]

$$\bar{p}_x - \bar{p}_L = \frac{12\bar{u}\mu}{H_L^2}(L-x)\zeta_L, \tag{5.3.1}$$

where

$$\zeta_L = \left[1 - \frac{192H_L}{\pi^5 W}\sum_{i=1,3,5,\ldots}^{\infty}\frac{\mathrm{Tanh}\left(\frac{i\pi W}{2H_L}\right)}{i^5}\right]^{-1}. \tag{5.3.2}$$

As H_L/W approaches zero, ζ_L approaches unity and **equation 5.3.1** reduces to the parallel plate form, **equation 4.7.2**. For the rectilinear flow cell channels, the height to width ratio is one, giving $\zeta_L \approx 2.371$. Therefore, the parallel plate assumption yields pressure drops that are approximately 2.371 times too low. As a result, the pressures that drive fluid flow through the membrane are also too low by this factor. A geometric factor for the upper channel, ζ_U, may be calculated similarly. The 2D model was corrected by incorporating the channel geometric factors in the Darcy equation. Thus, **equations 4.3.6** and **4.5.1.1** are modified to give

$$v_s = v_m = v_s^* + \frac{\kappa}{\mu H_m}\left(\zeta_L p_S' - \zeta_U p_P'\right) \tag{5.3.3}$$

and

$$v_n = v_m = \frac{\kappa}{\mu H_m}\left(\zeta_L P_P - \zeta_U P_N + \zeta_U \Pi_N'\right) \tag{5.3.4}$$

where Π' is a scaled osmotic pressure equal to the true osmotic pressure divided by ζ_U. This scaling operation is necessary because the pressures used in the calculation of the flow field may be considerably different in magnitude from those of true 3D duct flow.

The corrected model, 2D (wall effects), gives a much better fit of the experimental data. Further validation of the corrected 2D model comes from the 1D model of Taylor *et al.* [35] which calculates an average channel flow that incorporates wall effects. In **Figs. 5.3.1 through 5.3.3**, both of the models that account for channel side wall effects give very similar curves. In fact, the 1D model curve deviates from that of the 2D model by less than 2 %, with the maximum deviations occurring at the extrema of the upper channel. That is, for most of the flow domain, the models are in agreement to within less than 1 %.

5.4 Experimental Error and Limitations

As noted above, one source of experimental error is sampling. During sampling, air bubbles enter the syringe. For the most part, these bubbles were allowed to accumulate into an air gap between the plunger end and the BSA solution. The maximum error in the sample volume using this procedure is expected to be less than 0.5 μl of 20 μl, or 2.5 %. However, the use of old Hamilton syringes, the plungers and barrels of which had been interchanged many times, may have contributed to sampling error. The components of these precision instruments should not, in practice, be interchanged because poor fit and increased wear can lead to leakage. Additionally, since about 3 % of the total upper channel was withdrawn during sampling, disruption of the concentration field may have contributed to the error in the last samples taken. Thus, a conservative estimate of the total sampling error is about 3 %.

The 20 μl samples were diluted with 100 μl of buffer solution. The maximum dilution error, mainly due to pipetting, is roughly 1 to 2 %. The error in HPLC analysis was estimated with the sample injection replicate deviation from the mean of the replicates. On average, deviations of 0.3 % and 1.3 % for BSA concentrations of approximately 0.0149 g/ml and 0.00099 g/ml, respectively, were obtained. Similar dilution, pipetting, and analysis errors arose during BSA standard curve preparation.

Application of a root-mean-square calculation allows for the estimation of total error. The calculation gives a conservative total error value of approximately 4 % for all concentrations encountered in this work. Except for the first and last two points in **Fig. 5.3.2**, this value is greater than or equal to two standard deviations calculated for each mean value of three runs.

Clearly, the magnitude of the total error makes validation of the 2D model somewhat questionable when low degrees of polarization are obtained. What we need is validation at high BSA polarization. To accomplish this, a number of options are available. Firstly, the run duration could be increased to several weeks. However, this would lead to rather long periods of experimentation producing relatively small amounts of data. Furthermore, significant protein degradation would occur over long periods at room temperature. Consequently, increasing the run time is not practical and, in fact, certain benefits would be derived from shorter run times.

The other options leading to greater degrees of polarization deal with changing the hydrodynamics of the flow cell and membrane. The rate of polarization is ultimately dependent on fluid flux through the membrane, which in turn, is governed by Darcy's law. Therefore, increasing the driving force, that is, the pressure drop across the membrane, should accelerate the rate of solute polarization. This can be accomplished by raising the average velocity at the lower channel inlet. The problem with this approach is that the existing pump head is capable of delivering a maximum average velocity of about 16 cm/s. A higher capacity pump head could be used. Alternatively, the lower chamber height could be reduced to give a larger pressure drop in the lower channel. The last option is to use a membrane with a higher permeability.

In summary, the limitations of the current experimental design preclude further validation of numerical models at high degrees of BSA polarization. In the following section, a parametric study is presented to further compare the 1D and 2D models and to investigate potential strategies for reducing solute polarization.

5.5 Factors Affecting Solute Redistribution

The effects of the following factors on BSA polarization were investigated through numerical simulations: membrane permeability, average lower channel inlet velocity, run duration, initial BSA concentration, gravity, and Dextran 70 loading. The modified 2D model which incorporates side wall effects was used in all subsequent simulations. Unless otherwise stated, all subsequent 2D simulations assume the absence of a gravitational field. Since gravity is not built into the 1D model, this assumption allows for direct comparison of the two models.

The effect of membrane permeability on polarization predicted by the two models, assuming 6 h runs, is shown in **Fig. 5.5.1**. The permeabilities range from the low value of 3.33×10^{-13} cm, characteristic of the cellulose acetate membrane used in experimental runs, to 6.00×10^{-11} cm, typical of some polysulfone membranes **[13, 35]**. At the lower permeabilities, the 2D model is in excellent agreement with the 1D model. At the higher membrane permeability, the 1D model tends to overestimate the average BSA concentrations at the downstream end.

Similar trends can be seen in **Fig 5.5.2** in which the average lower channel inlet velocity, $\bar{v}$, is varied. As is the case for all subsequent simulations, a membrane permeability of 6.00×10^{-11} cm was used. As expected, the degree of BSA polarization increases with increasing lower channel velocities. That is, the data of **Figs. 5.5.1** and **5.5.2** indicate that fluid flux through the membrane is the predominating factor governing BSA redistribution along the length of the upper channel. Again, very good agreement between the two models exists along most of the length of the flow cell. However, as the average inlet velocity is increased, the discrepancy between the models near the flow cell outlet increases.

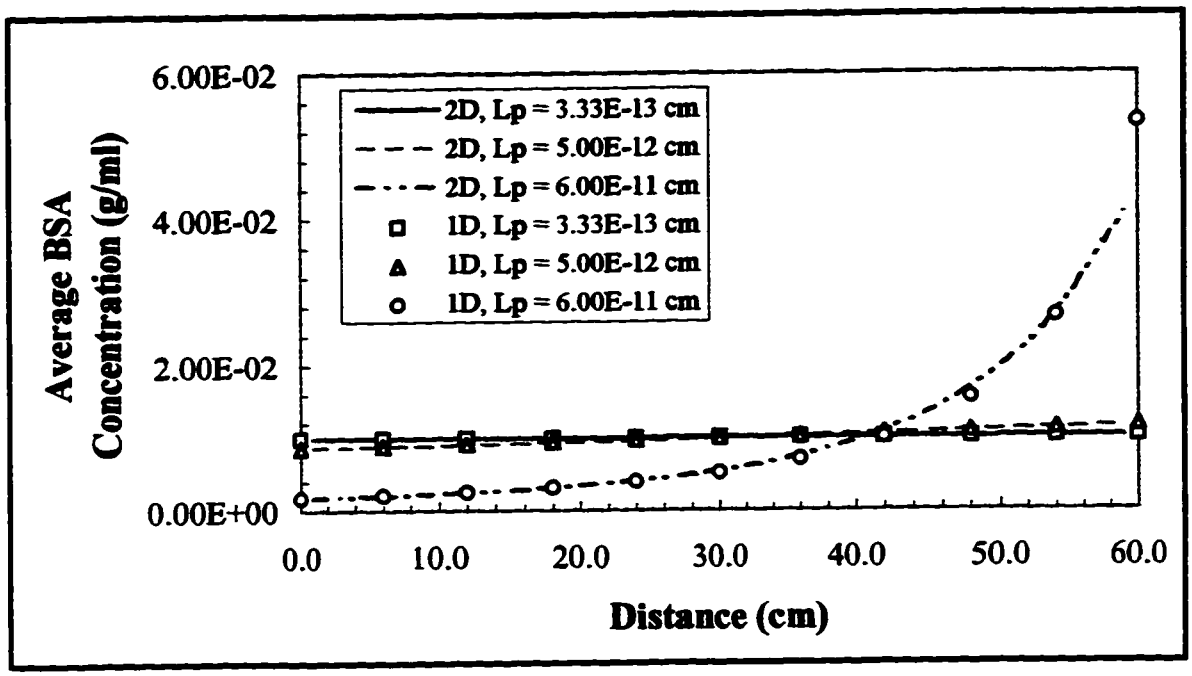

Figure 5.5.1. BSA polarization with membrane permeability as a parameter ($\bar{v} = 25$ cm/s, $t = 6$ h, $C_0 = 0.01$ g/ml).

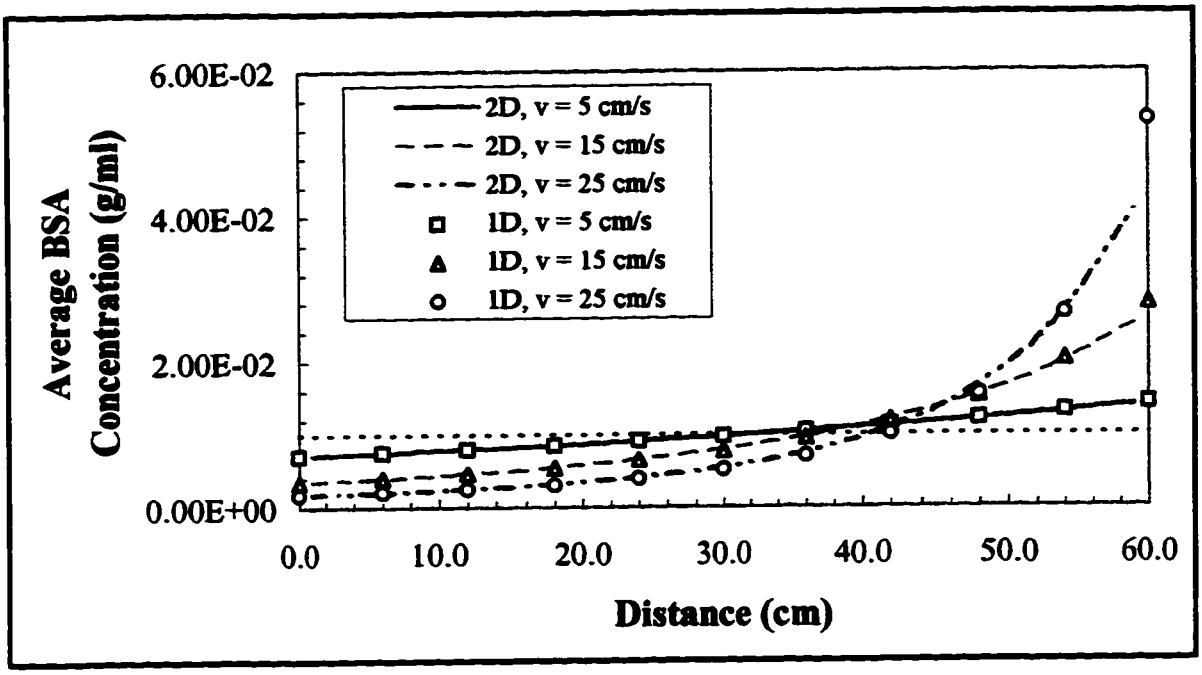

Figure 5.5.2. BSA polarization with average lower channel inlet velocity as a parameter ($L_p = 6.00 \times 10^{-11}$ cm, $t = 6$ h, $C_0 = 0.01$ g/ml).

The discrepancies between the two numerical models at the downstream end of the upper channel can be explained as follows. Thus far, only solute polarization along the length of the flow cell has been considered. However, solute redistribution in the transverse direction (y-axis) does occur. When the transmembrane fluid flux and BSA concentrations are low (**Figs. 5.5.3** and **5.5.4**), the concentrations at the membrane are essentially equivalent to the transversely averaged BSA concentrations. In this case, the 1D model can be applied. On the other hand, when the transmembrane flux is high (**Figs. 5.5.5** and **5.5.6**), significant transverse polarization occurs and the 1D model proves less accurate because it assumes a transversely averaged concentration profile. In particular, high BSA concentrations occur at the membrane near the downstream end of the flow cell. Since the osmotic pressure (a function of the local osmotically active solute concentration) at the membrane affects transmembrane flow, the use of a transversely averaged concentration profile can give rise to inaccurate osmotic pressure terms, and therefore, incorrect membrane fluid fluxes. The 1D model predicts a less extreme concentration variation along the membrane than is obtained with the 2D model. A greater degree of polarization along the membrane generates higher osmotic pressure

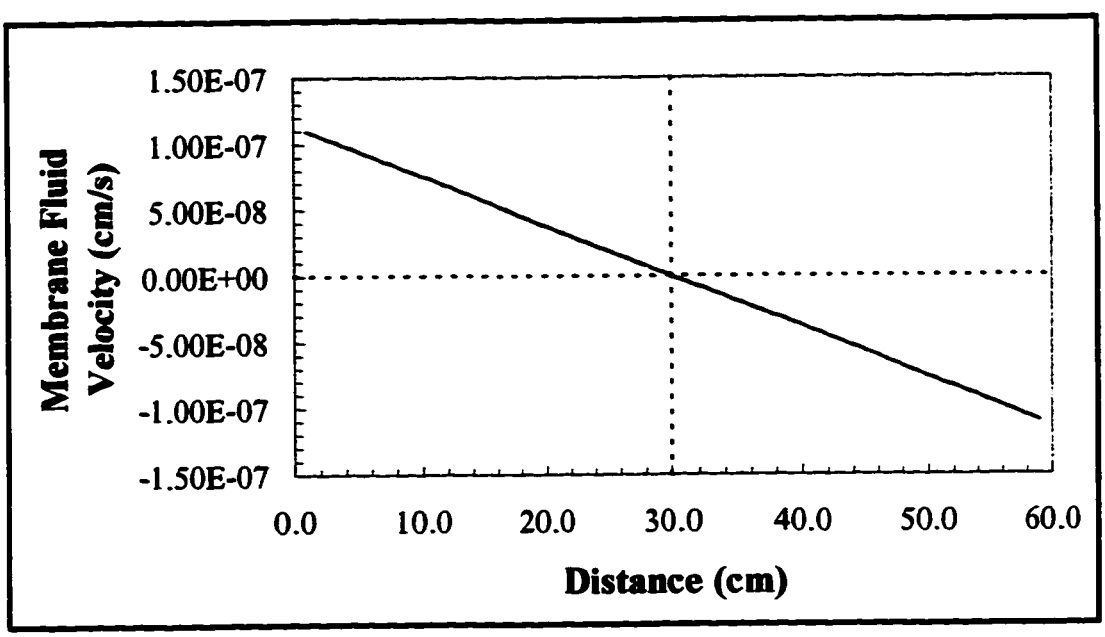

Figure 5.5.3. Fluid velocity profile for low permeability membrane ($L_p = 3.33 \times 10^{-13}$ cm, $\bar{v} = 25$ cm/s, $t = 6$ h, $C_0 = 0.01$ g/ml).

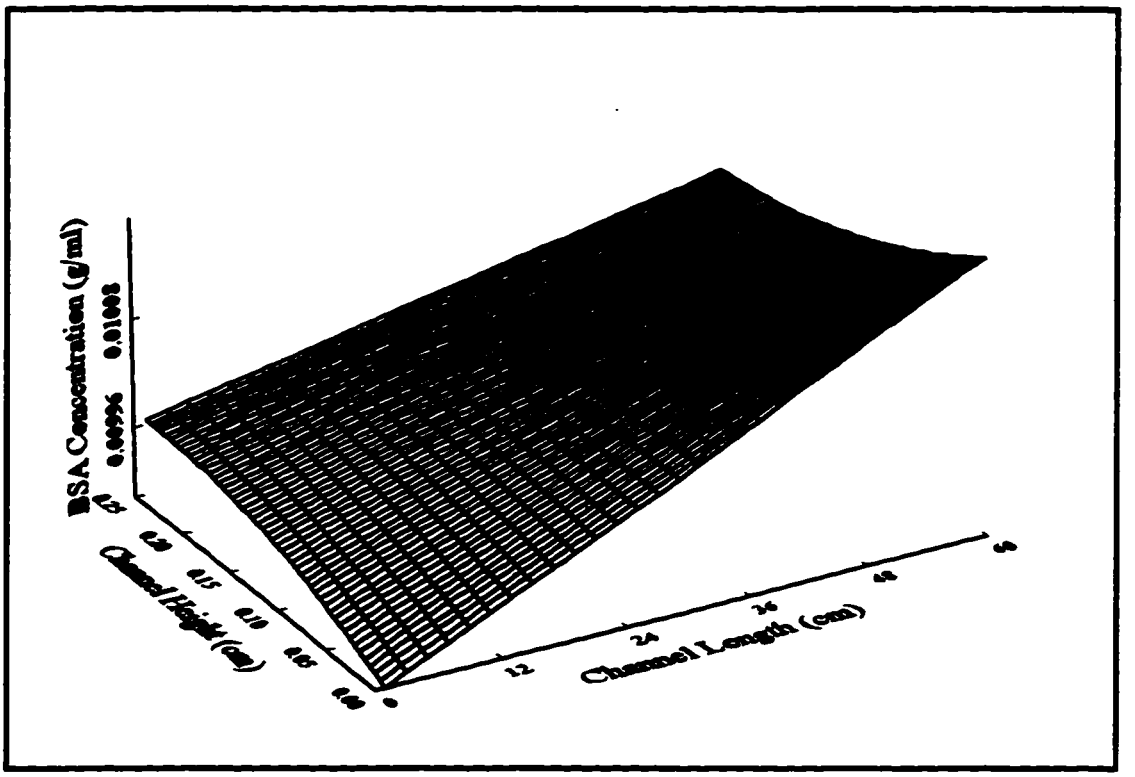

Figure 5.5.4. BSA concentration distribution for low permeability membrane ($L_p = 3.33 \times 10^{-13}$ cm, $\bar{v} = 25$ cm/s, $t = 6$ h, $C_0 = 0.01$ g/ml).

gradients which, in turn, can counteract the hydrodynamic pressure gradient and thereby reduce overall polarization. The net effect is that more protein accumulates at the membrane while less protein moves downstream. As shown in **Figs. 5.5.4** and **5.5.6**, the 2D model predicts the solute concentrations everywhere in the upper channel. As a result, no averaging error is introduced into the calculation of osmotic pressures and membrane fluid velocities.

Over time, BSA polarization is expected to increase as more protein is swept downstream. This is precisely the result shown for several practical run times in the semi-log plot of **Fig. 5.5.7**. Eventually, at a sufficiently long period of time, all the BSA will reside in a localized region at the downstream end of the upper channel. If a high enough initial BSA concentration is used, the resulting osmotic pressures would counteract the

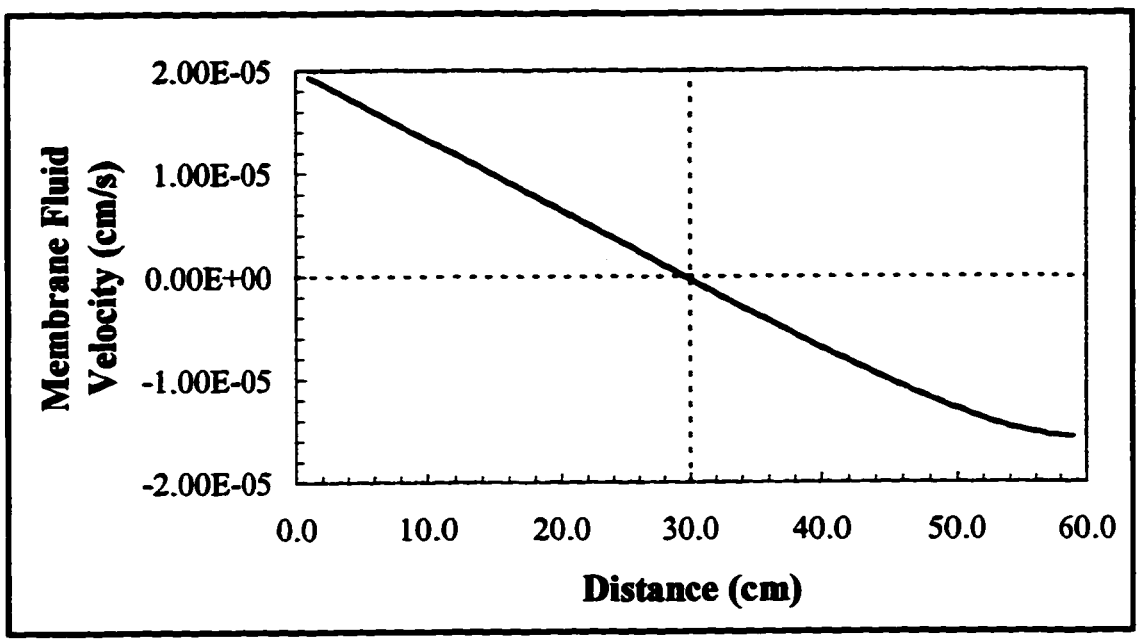

Figure 5.5.5. Fluid velocity profile for high permeability membrane ($L_p = 6.00 \times 10^{-11}$ cm, $\bar{v} = 25$ cm/s, $t = 6$ h, $C_0 = 0.01$ g/ml).

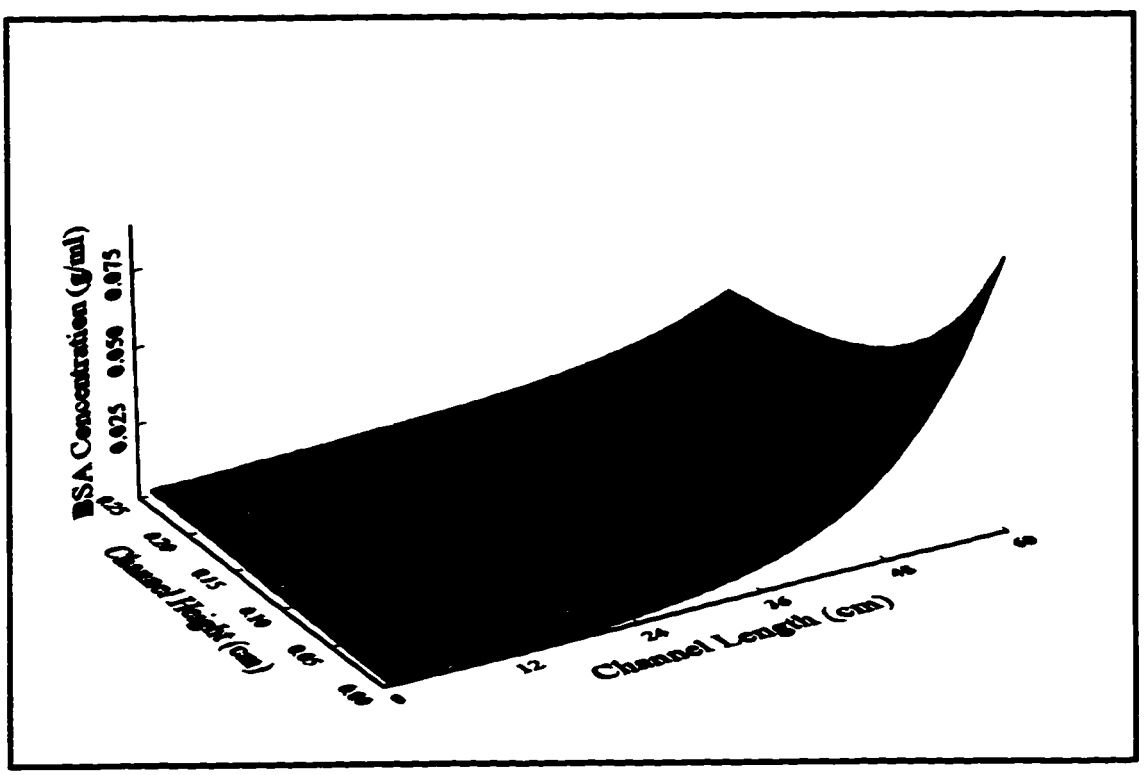

Figure 5.5.6. BSA concentration distribution for high permeability membrane ($L_p = 6.00 \times 10^{-11}$ cm, $\bar{v} = 25$ cm/s, $t = 6$ h, $C_0 = 0.01$ g/ml).

transmembrane pressure drop, effectively stopping flow through the membrane in this region. As indicated by **Fig. 5.5.5**, the steady state membrane fluid velocity profile would be asymmetric about the longitudinal center of the flow cell, with downstream velocities passing through a local minimum. In practice, however, very long run times are required for steady state to occur. Furthermore, due to the highly non-linear nature of the resultant mass fraction field, simulations under these conditions are very computationally expensive and prone to significant cumulative error. This, then, is one limitation of the 2D model.

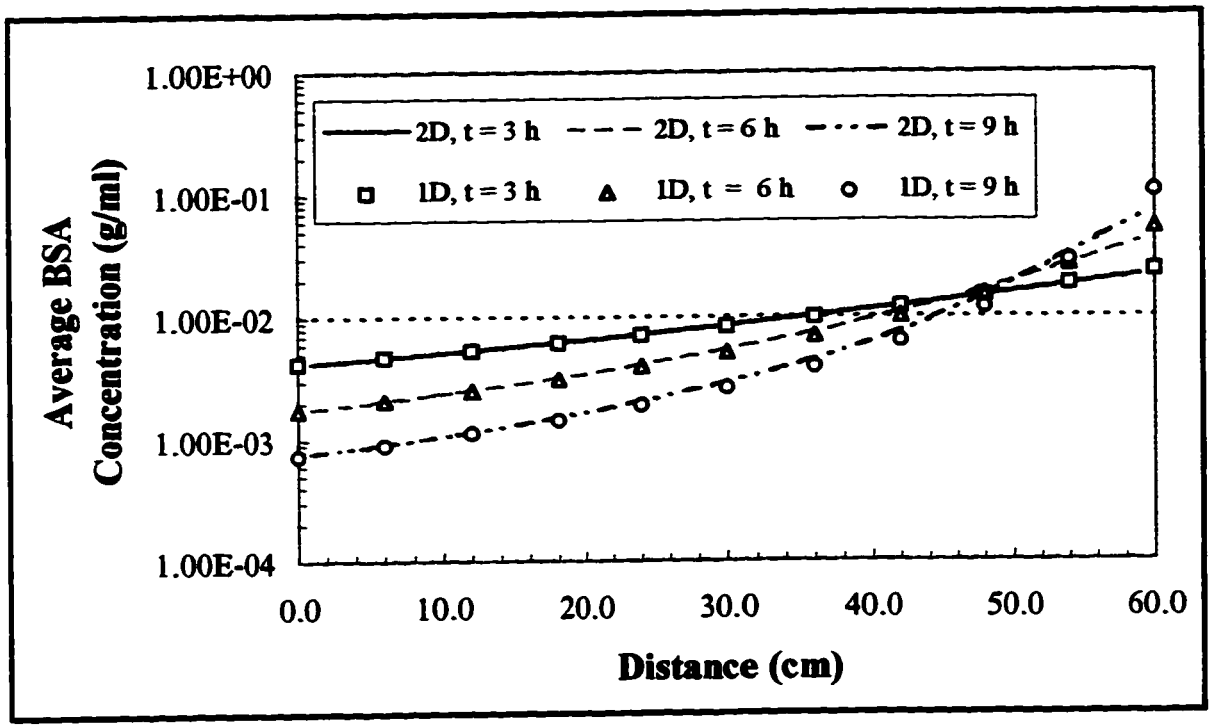

Figure 5.5.7. BSA polarization with run duration as a parameter ($L_p = 6.00 \times 10^{-11}$ cm, $\bar{v} = 25$ cm/s, $C_0 = 0.01$ g/ml).

If sufficient osmotic pressure gradients resulting from localized regions of high BSA concentrations can reduce fluid flow across the membrane, then high initial concentrations should slow down the rate of polarization throughout the upper channel. This is precisely the effect observed in **Fig. 5.5.8** and reported in the literature [**9, 13, 35**].

The concentration profiles of **Fig. 5.5.8** are normalized with respect to the initial BSA concentrations to clearly demonstrate the differences in polarization. The close agreement between the 1D and 2D models seen for the relatively low initial BSA concentrations of 0.01 g/ml (1 %, mass/volume) begins to break down at higher concentrations. Again, the discrepancy between the two models can be attributed to the considerable transverse concentration gradients that are generated at both ends of the flow cell, as shown in **Fig. 5.5.9**.

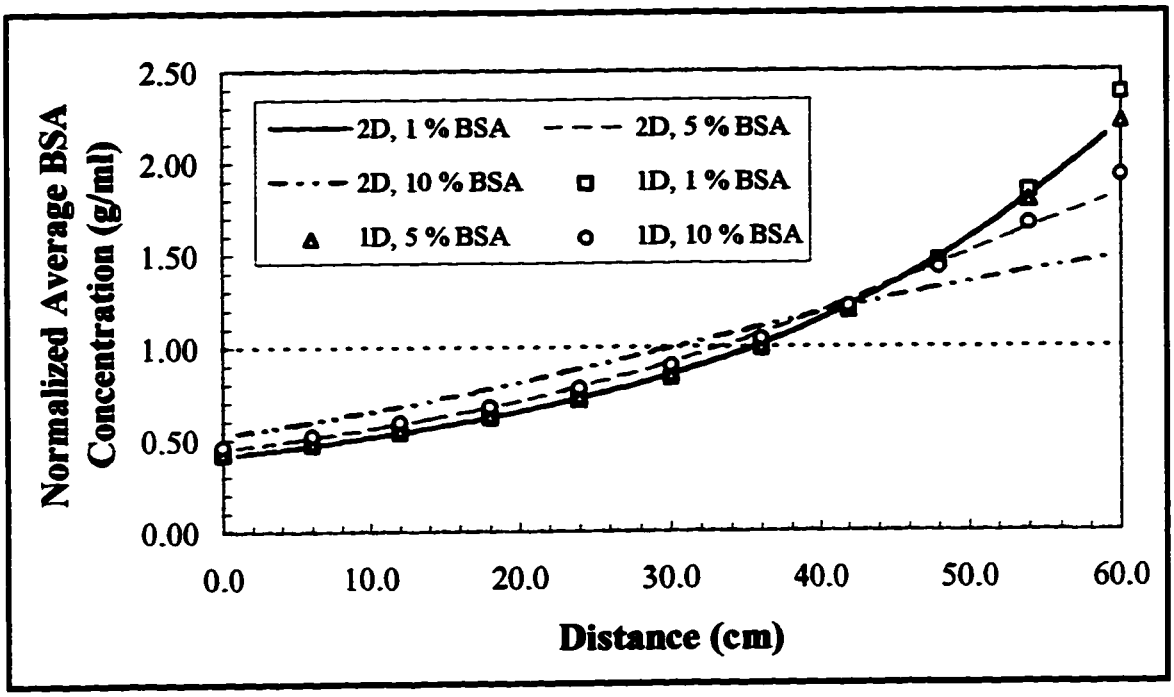

Figure 5.5.8. Normalized BSA concentration profiles with initial BSA concentration as a parameter ($L_p = 6.00 \times 10^{-11}$ cm, $\bar{v} = 25$ cm/s, $t = 3$ h).

It has been suggested that buoyancy effects may significantly contribute to the concentration of the protein layer at the membrane surface [5]. Simulations with approximately 0.1 % to 1.5 % BSA solutions, in the absence and presence of gravity (horizontal orientation), have consistently given similar results within the numerical error.

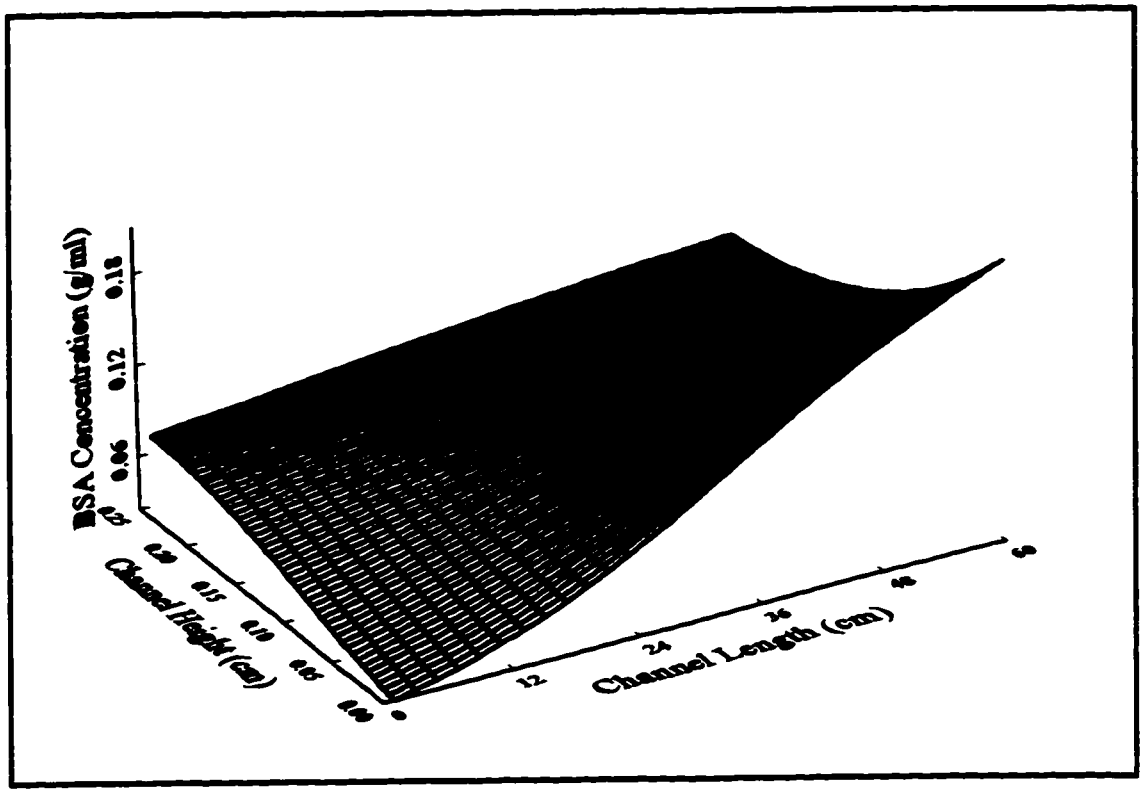

Figure 5.5.9. BSA concentration distribution for an initial BSA concentration of 0.1 g/ml ($L_p = 6.00 \times 10^{-11}$ cm, $\bar{v} = 25$ cm/s, $t = 3$ h).

If the main lower channel flow is taken to be the positive x-direction, four flow cell orientations (**Fig. 5.5.10**) may be defined as

Horizontal:	gravity perpendicular to the main flow direction, in the negative y-direction.
Inverted Horizontal:	gravity perpendicular to the main flow direction, in the positive y-direction.
Vertical:	gravity parallel to the main flow direction, in the positive x-direction.
Inverted Vertical:	gravity parallel to the main flow direction, in the positive x-direction.

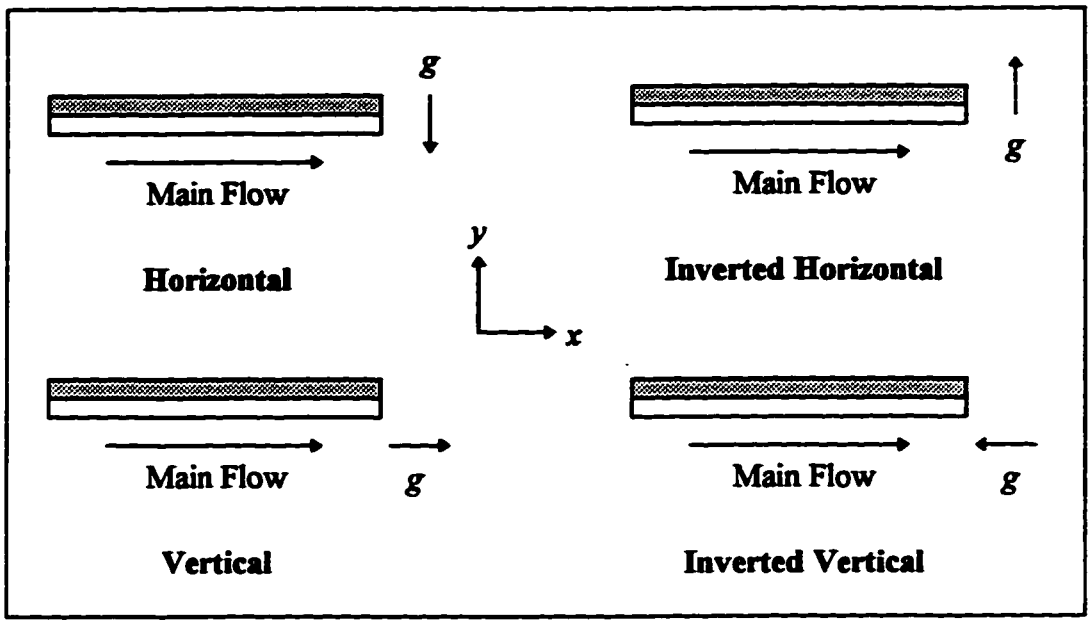

Figure 5.5.10. The four main flow cell orientations.

The effect of gravity at low BSA loading is shown in **Fig. 5.5.11**. The polarization curves for both horizontal orientations are similar to the zero gravity plot. The vertical orientation appears to give slightly more polarization. This observation is consistent with the protein settling downwards, thereby accelerating polarization. The inverted vertical orientation results in very little polarization. It is tempting to postulate that in the latter configuration buoyancy forces and diffusion offset forced convection, leading to negligible BSA movement. However, the shape of the transversely averaged concentration profile and the 2D BSA mass fraction distribution of **Figs. 5.5.11** and **5.5.12**, respectively, suggest that this explanation is perhaps too simplistic.

More information can be obtained from the velocity vector plot of **Fig. 5.5.13**, in which only the membrane and upper channel are drawn. Flow in the upper channel is divided into two regions of recirculation, each occupying approximately half of the channel. These recirculation patterns carry BSA transversely from the regions at the membrane near the longitudinal center of the channel. Of interest are how the

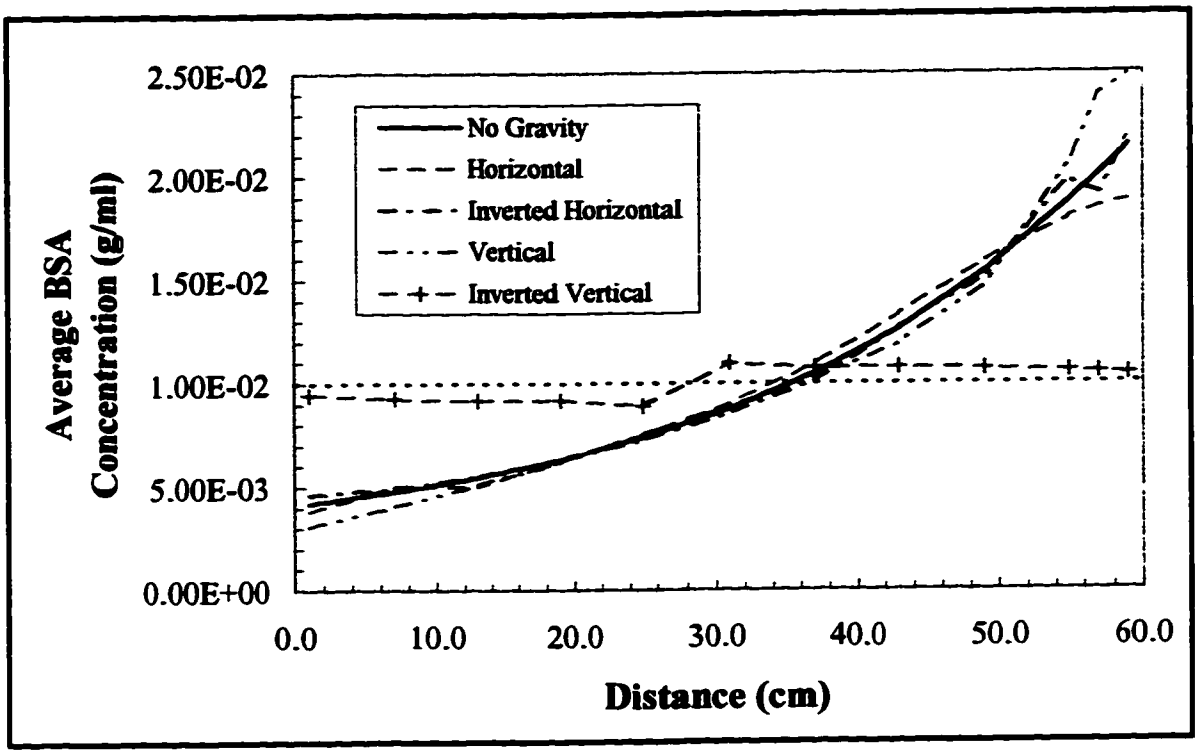

Figure 5.5.11. The effect of gravity on BSA polarization at low BSA loading ($L_p = 6.00 \times 10^{-11}$ cm, $\bar{v} = 25$ cm/s, $t = 3$ h, $C_0 = 0.01$ g/ml).

recirculation patterns develop and why transversely averaged BSA concentrations in the upstream half are less than the initial concentration while those in the downstream portion are above the starting value.

On start-up, the velocity distribution in the upper channel is such that fluid enters the channel through the first half of the membrane, is redirected longitudinally, moves along the length of the channel, and is redirected again toward the second half of the membrane through which it exits. This velocity distribution is precisely that shown in the example of **Fig. 4.9.9**. It is this convective flux which carries solutes downstream. Under the conditions of current interest, simulations have shown that slight but significant BSA polarization occurs within one minute. As the protein accumulates, the solution density rises and buoyancy forces become significant. Consequently, protein at the downstream

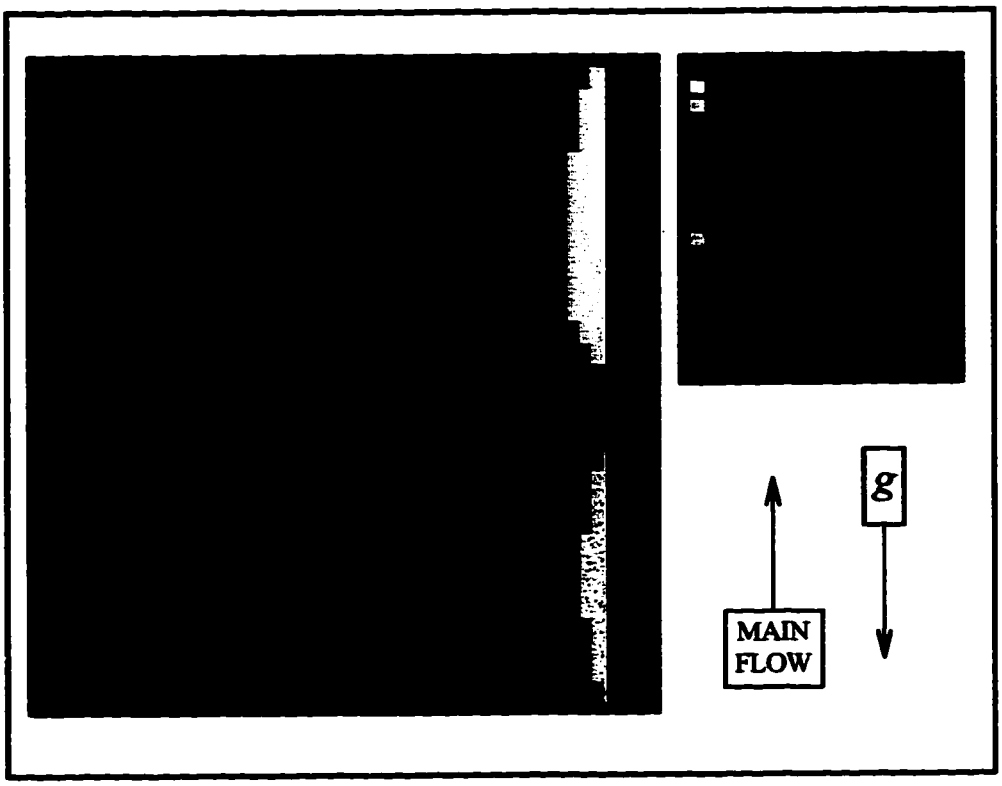

Figure 5.5.12. BSA mass fraction distribution at low BSA loading ($L_p = 6.00 \times 10^{-11}$, $\bar{v} = 25$ cm/s, $t = 3$ h, $C_0 = 0.01$ g/ml, inverted vertical orientation). Horizontal axis is scaled 160 times.

end tends to settle fastest, generating flow back down the fluid column. Concomitantly, a small clockwise eddy forms at the upstream wall. Within about 20 minutes the two small backflow regions develop into the full recirculation patterns of **Fig. 5.5.13**. Development over time of these recirculation patterns and associated BSA mass fraction fields are presented in **Appendix D**. Lastly, the initial BSA polarization effect coupled with a net downstream flow (**Fig. 5.5.14**) results in the different transversely averaged concentration profiles in the channel halves, despite the essentially linear variation in fluid velocity across the membrane. The distinct flow regimes generated in the inverted vertical orientation are not especially surprising in light of the findings of Taylor *et al.* [35] who have reported similar phenomena in HFBRs: after significant protein polarization a stagnant downstream region appears with transmembrane fluid exchange being confined to an upstream region.

At low BSA concentrations buoyancy effects are not expected to be large. Indeed, when compared to the results obtained in the absence of a gravity field, only the inverted vertical orientation generates dramatically different hydrodynamics and protein redistribution. However, it is expected that at high BSA concentrations, gravity will play a more significant role in protein polarization. This is supported by the results of simulations with 10 % BSA solutions, given in **Fig. 5.5.15**.

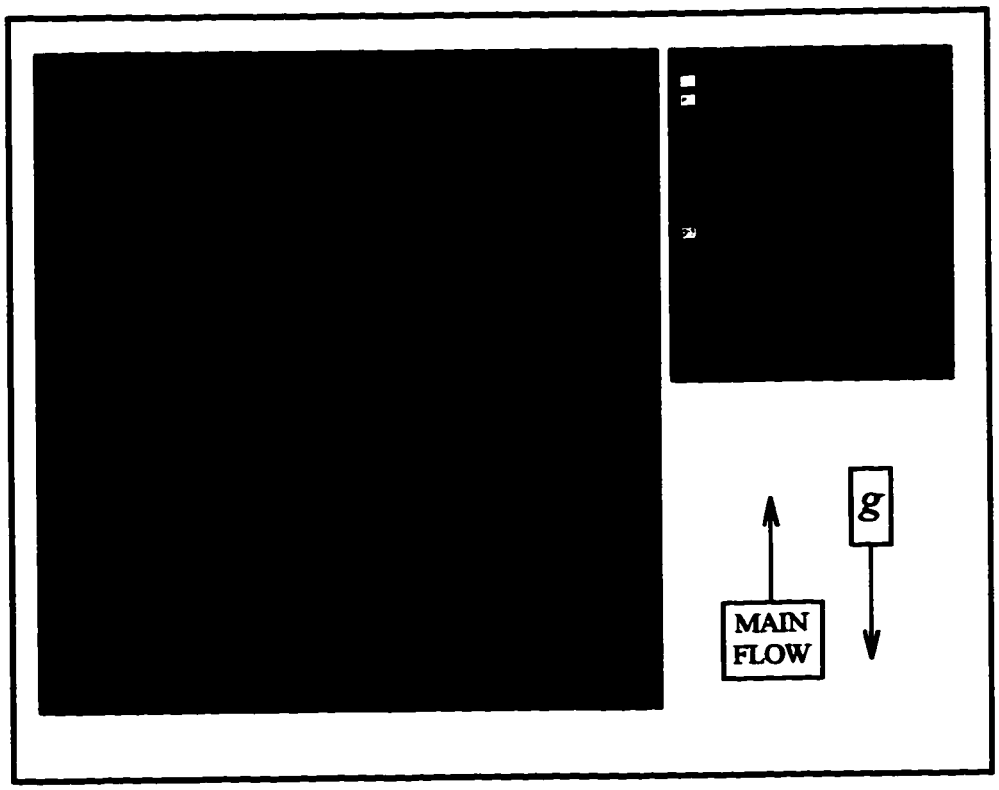

Figure 5.5.13. Velocity vector plot at low BSA loading ($L_p = 6.00 \times 10^{-11}$ cm, $\bar{v} = 25$ cm/s, $t = 3$ h, $C_0 = 0.01$ g/ml, inverted vertical orientation). Horizontal axis is scaled 160 times and velocities units are cm/s.

The most downstream portion of the 'horizontal' curve is nearly 10 % lower than the reference, 'no gravity', curve. This is consistent with BSA settling towards the membrane. This settling, gives rise to greater osmotic pressures, less transmembrane fluid transport and, thus, less BSA polarization. Exactly the same mechanism applies to the inverted horizontal case. BSA settles away from the membrane, accelerating

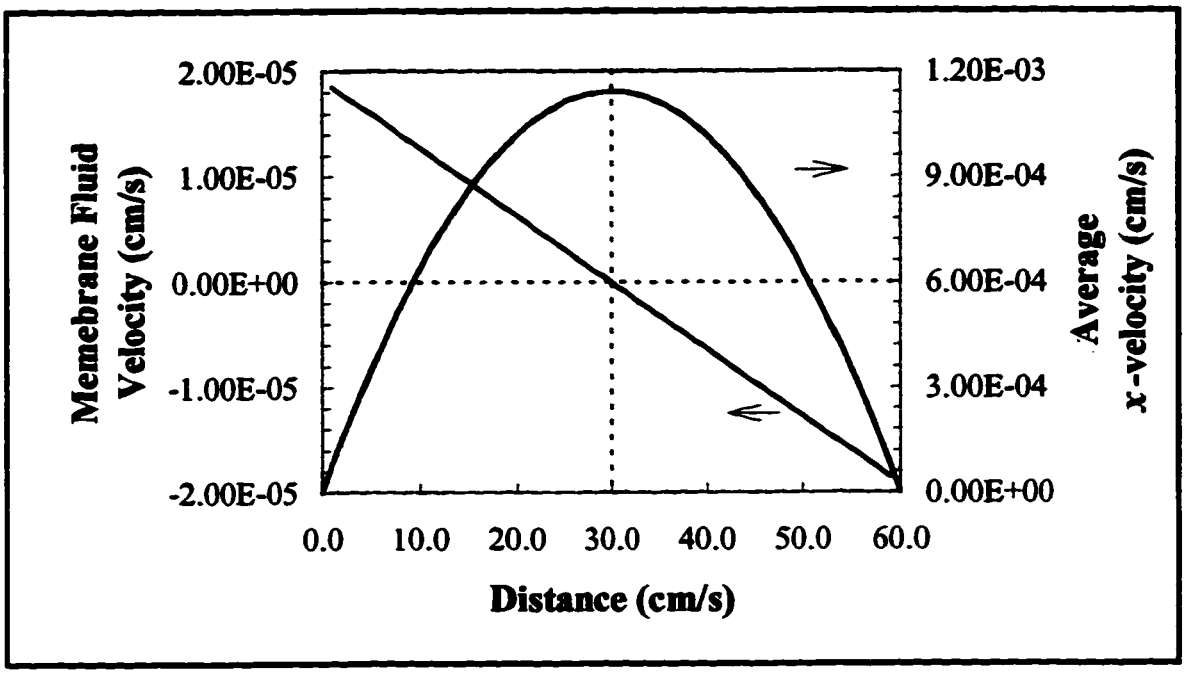

Figure 5.5.14. Membrane fluid and transversely averaged x-velocity profiles at low BSA loading ($L_p = 6.00 \times 10^{-11}$ cm, $\bar{v} = 25$ cm/s, t = 3 h, C_0 = 0.01 g/ml, inverted vertical orientation).

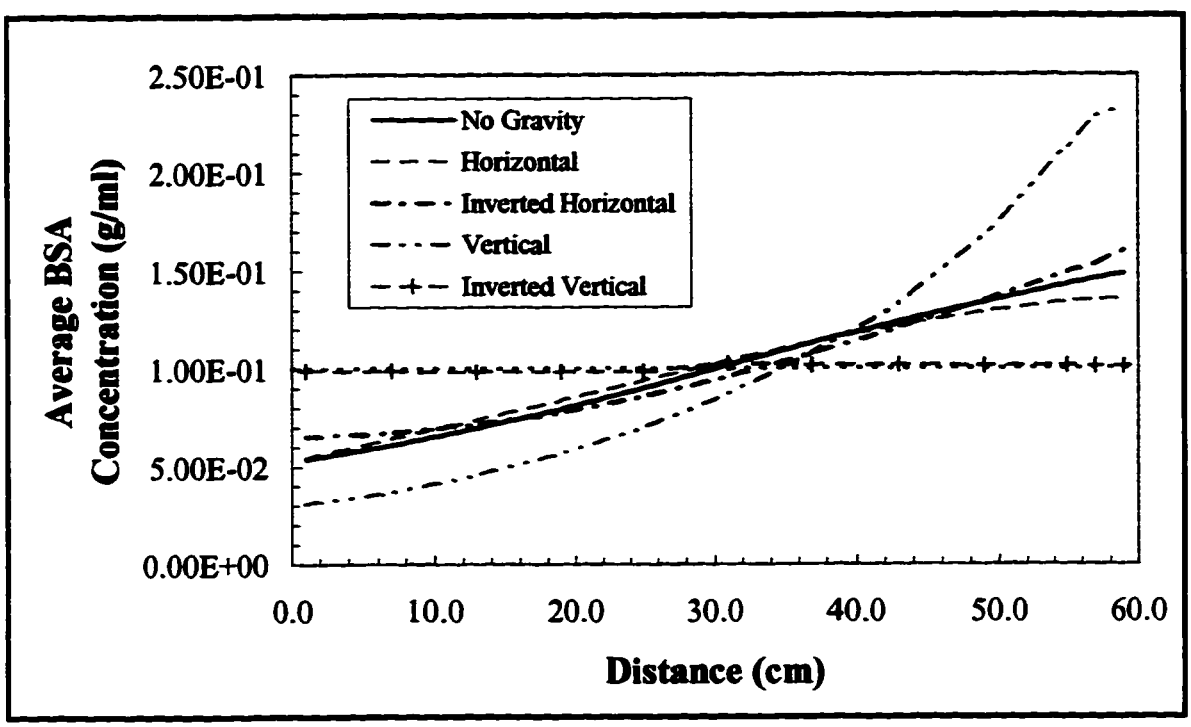

Figure 5.5.15. The effect of gravity on BSA polarization at high BSA loading ($L_p = 6.00 \times 10^{-11}$ cm, $\bar{v} = 25$ cm/s, $t = 3$ h, $C_0 = 0.1$ g/ml).

polarization and enriching the solution below the membrane, giving rise to a positive deflection of about 10 % with respect to the reference curve. For the vertical orientation, BSA polarization is effected by a combination of transmembrane flow and protein settling down the fluid column. The net result is a positive deflection, at the downstream end of the channel, of almost 60 % from the reference curve. Finally, because of the recirculation patterns caused by transmembrane flow and buoyant settling, the inverted vertical orientation gives virtually no longitudinal BSA polarization. Clearly, then, gravity plays a significant role in the redistribution of protein in the rectilinear flow cell. Furthermore, the impact of buoyant forces on BSA polarization increases with the magnitude of the starting protein concentration.

We now direct our attention solely to solute loading and again ignore the effects of gravity. As discussed above, protein polarization can be substantially attenuated by osmotic pressures which counteract transmembrane flow. This has been shown through simulations with elevated BSA concentrations. It should be possible, then, to generate high osmotic pressures by adding other osmotically active species to low concentration BSA solutions, and thereby inhibit BSA polarization. The results of simulations with 1 % BSA solutions with varying amounts of Dextran 70 are plotted in **Fig. 5.5.16**. Transversely averaged Dextran 70 concentration profiles are qualitatively similar to those of BSA and were, therefore, omitted here. As expected, the extent of BSA polarization decreases with increased Dextran 70 loading.

In summary, the 2D model has shown that the membrane permeability, lower channel inlet average velocity, run duration, initial BSA concentration, gravity, and Dextran 70 loading affect BSA polarization within the rectilinear flow cell. Judicious selection of these operating parameters should allow for the significant reduction of protein polarization within HFBRs.

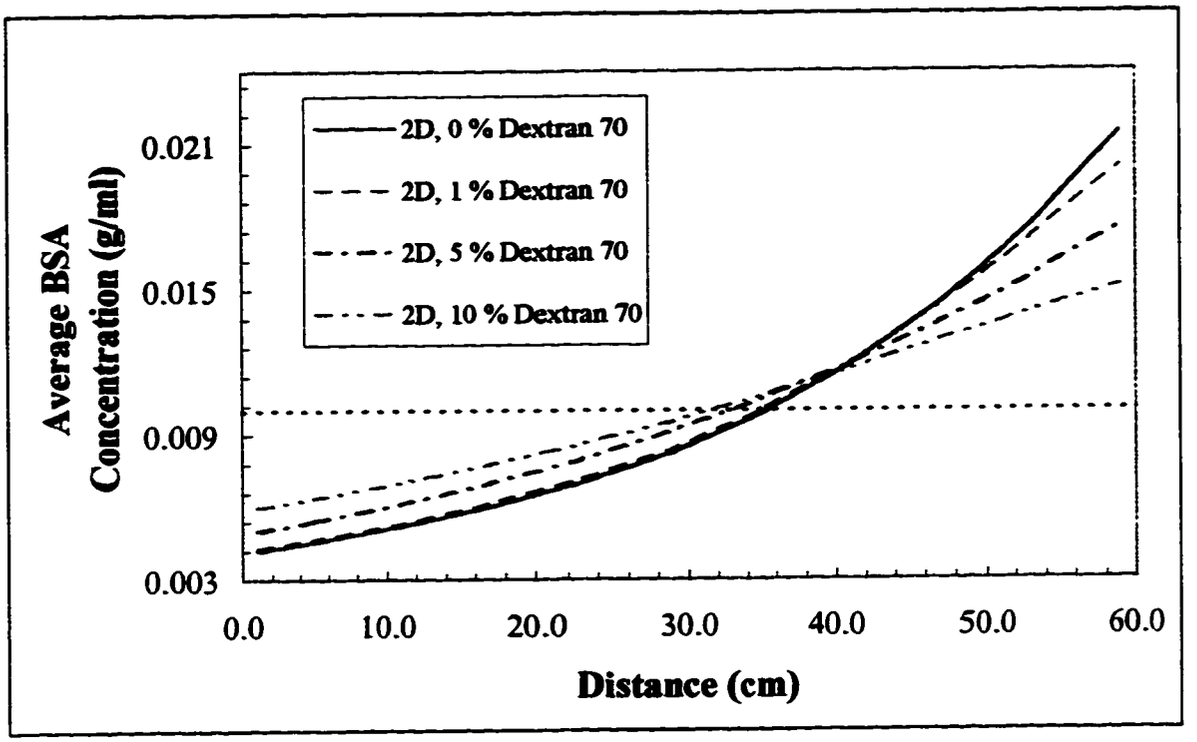

Figure 5.5.16. The effect of Dextran 70 loading on BSA polarization ($L_p = 6.00 \times 10^{-11}$ cm, $\bar{v} = 25$ cm/s, $t = 3$ h, $C_0 = 0.1$ g/ml).

5.6 Numerical Limitations

While the 2D model has served well thus far, it has several limitations. Because of experimental limitations, fairly cursory validation of the model was carried out. Further experimentation, particularly runs with much higher degrees of protein polarization, should allow for more stringent validation.

As noted previously, the pressure and velocity distributions that are numerically generated apply to flow between semi-infinite parallel plates. This is not problematic from a solute polarization standpoint because of the geometric correction applied in the membrane velocity calculation. The calculation of averaged velocity and pressure distributions for duct flows would require additional incorporation of geometric factors.

Alternatively, the model could be extended to three dimensions. In either case, considerably more computational effort and data storage would be required.

This brings us to the fact that the model can be quite slow in generating a solution. This is especially true when highly nonlinear flow and mass fraction fields are obtained. Additionally, very long run times can result in protein mass balances with relative errors greater than 1 %, presumably because the model cannot adequately handle very nonlinear profiles. Even when the error is negligible, small anomalies appear in some solutions. For example, close inspection of the data of **Figs. 5.5.12** and **5.5.13** reveals small eddies and concentration perturbations near the center of the upper channel. It is difficult to say whether these phenomena are physically real, a consequence of mixing of fluid streams, for example, or numerical artifacts resulting from spatial and temporal discretization.

It is expected that the use of finer grids should resolve some of these issues. However, the time required for solution will grow and relaxation techniques may have to be developed to accelerate computation. Another related difficulty is that of the 'low permeability problem' discussed in **section 4.8**, possibly the result of round-off and truncation errors. The use of scaling factors or dimensionless groups may eliminate the need for the work-around that was developed here. However, the ultimate effects of this approach on the final solution accuracy and computational time are not clear.

From an experimental point of view, end effects are not accurately modeled and flow-cycling, shown to reduce protein polarization in HFBRs [3], cannot be practically simulated. These inadequacies could be corrected by recoding the simulator to properly account for the inlet and outlet geometries, and incorporating a flow-switching option. Lastly, averaged concentration and velocity profiles could be added to the program's graphical interface. This would eliminate the need for subsequent raw data manipulations. Lastly, this thesis complete with all the text, graphics files, FORTRAN code, simulations, and experimental data is provided on a CD ROM. Details of the CD's contents may be found in **Appendix E**.

Chapter 6

Conclusions and Recommendations

6.1 Conclusions

On the basis of the experimental and modeling work conducted, the following conclusions may be drawn :

1. As a result of the redesign and rebuild, as well as the development of specific procedures, the cell-free rectilinear membrane flow cell is now fully operational and can be used to obtain meaningful data.

2. *In situ* membrane permeability determinations are now possible and suggest that the cellulose acetate membrane hydrodynamics are essentially unaffected by BSA conditioning.

3. Because of design limitations such as membrane permeability, pump capacity, and flow cell geometry, only low degrees of BSA polarization can currently be obtained.

4. Flow cell sampling errors for BSA concentrations of approximately 0.001 to 0.015 g/ml are expected to be roughly 4 %.

5. A two-dimensional control-volume model using S. V. Patankar's SIMPLER algorithm was constructed and allows for simulation of the hydrodynamics and protein redistribution within the rectilinear flow cell. This numerical model is comprehensive in that it takes into account transience, multiple solutes, gravity, and changes in density, viscosity, diffusivities, and osmotic pressures.

6. Preliminary experimental results and comparisons against a simulator based on a 1D model of the system suggest the validity of the 2D model, and its simulator, respectively.

7. 2D simulations are consistent with theoretical considerations and show that run duration, membrane permeability, lower channel inlet average velocity, gravity, and osmotically active species loading affect the polarization process. Specifically, increasing the run duration, membrane permeability, or average velocity increases solute polarization. Raising osmotically active species concentrations reduces solute polarization. Buoyant effects due to the presence of a gravity field are significant at elevated solute concentrations. Simulations have provided strong evidence that significant reductions in protein polarization come about as a result of buoyancy-induced fluid recirculation patterns when the rectilinear flow cell is operated in the inverted vertical mode (buffer flowing in the lower channel against gravity).

9. 2D simulations indicate that along with longitudinal protein polarization, some transverse polarization always occurs. As transverse polarization increases, agreement between the 1D and 2D models declines.

10. The 2D model has several potentially significant limitations: the model does not adequately describe the flow cell inlet and outlet geometries (end effects), and acceptable computational times and numerical errors may not be possible for highly non-linear systems under certain conditions.

11. As a result of the inlet and outlet geometries, areas of high pressure exist at the ends of the lower channel. It is expected that such a high pressure region at the outlet end of the flow cell is responsible for reduced transmembrane flow, the establishment of a stagnant zone in the upper channel, and a concomitant drop in protein polarization.

6.2 Recommendations

To further the work presented here, the following recommendations are made:

1. Additional validation of the 2D model should be obtained under more rigorous experimental conditions. In particular, greater degrees of BSA polarization under various operating conditions (that is, the factors affecting polarization) are required.

2. To obtain more longitudinal polarization, transmembrane fluid flow must be increased. This could be accomplished by using a more permeable membrane, raising the average inlet velocity by using a higher capacity pump head and/or by reducing the lower channel height, or a combination of the two.

3. The issue of end effects should be reconciled by either recoding the model geometry or moving the sampling ports away from the ends of the upper channel.

4. If, in the future, true duct flow velocity and pressure distributions will be required, wall effects will have to be incorporated into the Navier-Stokes equations, presumably through the introduction of geometric terms.

5. Further optimization of the FORTRAN code and investigation of other solution techniques and the use of relaxation factors should be carried out to improve the performance of the simulator. Additionally, running the code on high performance computers optimized for central processing unit intensive tasks is desirable.

6. To add functionality to the existing code, flow-switching and additional plotting (averaged concentration and velocity profiles) capabilities should be added.

7. The factors affecting the polarization process, fundamentally applicable to HFBRs, allow for the development of strategies to control solute distribution within these devices. A combined heuristic and empirical approach using the results obtained with the 2D model for the rectilinear flow cell should allow for the control of Starling flow and solute polarization in HFBRs.

References

1. Belfort, G., "Membranes and Reactors: A Technical Challenge in Biotechnology," *Biotechnol. Bioeng.*, **33**, 1047-1066 (1989).

2. Heath, C. A., G. Belfort, B. E. Hammer, S. D. Mirer and J. M. Pimbley, :Magnetic Resonance Imaging and Modeling of Flow in Hollow-Fiber Bioreactors," *AIChE J.*, **36**, 547-558 (1990).

3. Piret, J. M. and C. L. Cooney, "Mammalian Cell and Protein Distributions in Ultrafiltration Hollow Fiber Bioreactors," *Biotechnol. Bioeng.*, **36**, 902-910 (1990).

4. Paterson, S. L., "Hollow Fibre Immobilised Cell Bioreactors,' *Chem. Eng. Austral.*, no. 3, 20-21 (1986).

5. Bhola, S., "Effects of Solute Polarization on the hydrodynamics within Membrane-Fluid-Solute Systems, with Special Application to Hollow Fiber Bioreactors," Masters Dissertation, University of Ottawa (1994).

6. Jauregui, H. O., S. Naik, H. Santangini, J. Pan, D. Trenkler and C. Mullon, "Primary Cultures of Rat Hepatocytes in Hollow Fiber Chambers," *In Vitro Cell. Dev. Biol.*, **30A**, 23-29 (1994).

7. Kelsey, L. J., M. R. Pillarella and A. L. Zydney, "Theoretical Analysis of Convective Flow Profiles in a Hollow-Fiber Membrane Bioreactor," *Chem. Engng. Sci.*, **45**, 3211-3220 (1990).

8. Lowrey, D., S. Murphy and R. A. Goffe, "A Comparison of Monoclonal Antibody Productivity in Different Hollow Fiber Bioreactors," *J. Biotechnol.*, **36**, 35-38 (1994).

9. Patkar, A. Y., J. Koska, D. G. Taylor, B. D. Bowen and J. M. Piret, "Protein Transport in Ultrafiltration Hollow-Fiber Bioreactors," *AIChE J.*, **41**, 415-425 (1995).

10. Harbour, C., J. P. Barford and K. S. Low, "Process Development for Hybridoma Cells," *Adv. Biochem. Eng./Biotechnol.*, **37**, 2-37 (1988).

11. Bailey, J. E. and D. F. Ollis, *Biochemical Engineering Fundamentals*, McGraw-Hill Publishing Co., Toronto, 652 (1986).

12. Sardonini, C. and D. DiBiasio, "Design and Operating Criteria for Hollow Fiber Bioreactors," *Bioproc. Engr.*, **15**, 327-330 (1996).

13. Taylor, D.G. and D. Boukouris, "Influencing Hollow Fiber Bioreactor Hydrodynamics through Osmotic Pressures: a Model Study," *Chem. Engng. Sci.*, **50**, 1513-1517 (1995).

14. Gerner, F.-J., "Novel Hollow Fiber Applications in Medicine and Biotechnology," *Membrane Processes in Separation and Purification*, J. G. Crespo and K. W. Böddeker (eds.), Kluwer Academic Publishers, Netherlands, 207-225 (1994).

15. Leonard, E. F., "The Application of Artificial Organs to Biotechnology," Membrane Separations in Biotechnology, W. C. McGregor (ed.), Marcel Dekker, New York, chap. 12 (1986).

16. Cieslinski, D. A. and H. D. Humes, "Tissue Engineering of a Bioartificial Kidney," *Biotechnol. Bioengng.*, **43**, 678-681 (1994).

17. Pillarella, M. R. and A. L. Zydney, "Theoretical Analysis of the Effect of Convective Flow on Solute Transport and Insulin Release in a Hollow Fiber Bioartificial Pancreas," *J. Biochem. Engng.*, **112**, 220-228 (1990).

18. Lombardi, C. P., A. Urso, G. Catapano, G. Careddu, G. Ghirlanda, F. Ceriati, G. Brisinda, R. Bellantone, G. B. Doglietto and F. Crucitti, "Membrane Bioreactors as Hybrid Artificial Pancreas: Experimental Evaluation," *Int. J. Artif. Organs*, **15**, 126-130 (1992).

19. Yang, H., H. Iwata, H. Shimizu, T. Takagi, T. Tsuji and F. Ito, "Comparative Studies of *in Vitro* and *in Vivo* Function of Three Different Shaped Bioartificial Pancreases Made of Agarose Hydrogel," *Biomaterials*, **15**, 113-120 (1994).

20. Ohzato, H., M. Carretta, T. Maki, S. J. Sullivan, K. Borland, T. E. Muller, B. A. Solomon, W. L. Chick and A. P. Monaco, "Use of Xenogeneic Islets in Hybrid Artificial Pancreas for Treatment of Diabetes without Immunosuppression," *Transplant. Proc.*, **24**, 661-662 (1992).

21. Jauregui, H. O., C. J.-P. Mullon, D. Trenkler, S. Naik, H. Santangini, P. Press, T. E. Muller and B. A. Solomon, "*In Vivo* Evaluation of a Hollow Fiber Liver Assist Device," *Hepatology*, **21**, 460-469 (1995).

22. Dixit, V., "Development of a Bioartificial Liver Using Isolated Hepatocytes," *Artif Organs*, **18**, 371-384 (1994).

23. Giorgio, T. D., A. D. Moscioni, J. Rozga and A. A. Demetriou, "Mass Transfer in a Hollow Fiber Device Used as a Bioartificial Liver," *ASAIO J.*, 886-892 (1993).

24. Nyberg, S. L., M. V. Peshwa, W. D. Payne, W.-S. Hu and F. B. Cerra, "Evolution of the Bioartificial Liver: the Need for Randomized Clinical Trials," *J. Am. Surg.*, **166**, 512-521 (993).

25. Sussman, N. L., M. G. Chong, T. Koussayer, D.-E. He, T. A. Shang, H. H. Whisennand and J. H. Kelly, "Reversal of Fulminant Hepatic Failure Using an Extracorporeal Liver Assist Device," *Hepatology*, **16**, 60-65 (1992).

26. Starling, E. H., "On the Absorption of Fluids from the Connective Tissue Spaces," *J. Physiol.*, **19**, 312-326 (1896).

27. Tharakan, J. P. and P. C. Chau, "Operation and Pressure Distribution of Immobilized Cell Hollow Fiber Bioreactors," *Biotechnol. Bioengng.*, **38**, 1064-1071 (1986).

28. Sourirajan, S. and T. Matsuura, *Reverse Osmosis/Ultrafiltration Process Principles*, National Research Council of Canada, Ottawa, 85-87, 583 (1985).

29. Aimar, P., J. A. Howell, M. J. Clifton and V. Sanchez, "Concentration Polariation Build-up in Hollow Fibers: a Method of Measurement and Its Modelling in Ultrafiltration," *J. Membrane Sci.*, **59**, 81-99 (1991).

30. Gill, W. N., D. E. Wiley, C. J. D. Fell and A. G. Fane, "Effect of Viscosity on Concentration Polarization in Ultrafiltration," *AICHE J.*, **34**, 1563-1567 (1988).

31. Moin, P. and J. Kim, "Tackling Turbulence with Supercomputers," *Sci. Am.*, **276**(1), 62-68 (1997).

32. Apelblat, A., A. Katzir-Katchalsky and A. Silberberg, "A Mathematical Analysis of Capillary-Tissue Fluid Exchange," *Biorheology*, **11**, 1-49 (1974).

33. Bruining, W. J., "A General Description of Flows and Pressures in Hollow Fiber Membrane Modules," *Chem. Engng. Sci.*, **44**, 1441-1447 (1989).

34. Salmon, P. M., S. B. Libicki and C. R. Robertson, "A Theoretical Investigation of Convective Transport in the Hollow-Fiber Reactor," *Chem. Engng. Comm.*, **66**, 221-248 (1988).

35. Taylor, D.G., J. M. Piret and B. D. Bowen, "Protein Polarization in Isotropic Membrane Hollow-Fiber Bioreactors," *AIChE J.*, **40**, 321-333 (1994).

36. Labecki, M., J. M. Piret and B. D. Bowen, "Two-Dimensional Analysis of Fluid Flow in Hollow-Fibre Modules," *Chem. Engng. Sci.*, **50**, 3369-3384 (1995).

37. Labecki, M., B. D. Bowen and J. M. Bowen, "Two-Dimensional Analysis of Protein Transport in the Extracapillary Space of Hollow-Fibre Modules," *Chem. Engng. Sci.*, **51**, 4197-4213 (1996).

38. Sigma Chemical Company, Biochemicals, *Organic Compounds for Research and Diagnostic Reagents*, Sigma Chemical Co., St. Louis, 64 (1993).

39. Waterland, L. R., C. R. Robertson and A. S. Michaels, "Enzymatic Catalysis Using Asymmetric Hollow Fiber Membranes," *Chem. Engng. Comm.*, **2**, 37-47 (1975).

40. Cole-Parmer Instrument Company, *Instruments for Research, Industry, and Education Catalog*, Cole-Parmer Instrument Co., Evanston, 1016 (1993-1994).

41. Ohaus Corporation, Precision Plus Electronic Balances Instruction Manual, Ohaus Corp., Belfountain, 55 (1993).

42. Millipore Corporation, *The Waters Chromatography Handbook*, Millipore Corp., Milford, 95-98 (1993-1994).

43. Patankar, S. V., Numerical Heat Transfer and Fluid Flow, Hemisphere Publishing Corp., New York, (1980).

44. Harlow, F. H. and J. E. Welch, "Numerical Calculation of Time-Dependent Viscous Incompressible Flow of Fluid with Free Surface," *Phys. Fluids*, **8**, 2182 (1965).

45. Perry, R. H. and D. Green (eds.), *Perry's Chemical Engineers' Handbook*, sixth ed., McGraw-Hill, Toronto, 3-73-3-76 (1984).

46. White, F. M., *Viscous Fluid Flow*, second ed., McGraw-Hill, Toronto, 120, 565 (1991).

47. Treybal, R. E., *Mass-Transfer Operations*, third ed., McGraw-Hill, Toronto, 35 (1980).

48. Bradley, R., "Design Considerations for Reverse Osmosis Systems," *Reverse Osmosis: Membrane Technology, Water Chemistry, and Industrial Applications*, Z. Amjad (ed.), Van Nostrand Reinhold, New York, (1993).

Appendix A

Raw Data

Table A.1. Pump calibration data.

Apparent Flow Rate (ml/min)	Time (s)	Initial Mass (g)	Final Mass (g)	Dispensed Mass (g)	Dispensed Volume (ml)	Channel Velocity (cm/s)
5.0	300.0	26.334	49.754	23.420	23.49	1.25
5.0	300.0	49.754	73.182	23.428	23.50	1.25
5.0	1500.0	73.182	192.125	118.943	119.30	1.27
10.0	360.0	1.765	63.677	61.912	62.10	2.76
10.0	360.0	63.677	125.311	61.634	61.82	2.75
10.0	300.0	0.000	50.705	50.705	50.86	2.71
15.0	300.0	50.705	129.435	78.730	78.97	4.21
15.0	300.0	0.000	78.750	78.750	78.99	4.21
15.0	240.0	78.750	142.220	63.470	63.66	4.24
20.0	180.0	0.000	63.755	63.755	63.95	5.68
20.0	150.0	63.755	116.874	53.119	53.28	5.68
20.0	150.0	116.874	170.343	53.469	53.63	5.72
25.0	120.0	0.000	53.600	53.600	53.76	7.17
25.0	120.0	53.600	107.404	53.804	53.97	7.20
25.0	120.0	107.404	161.085	53.681	53.84	7.18
30.0	120.0	0.000	64.646	64.646	64.84	8.65
30.0	120.0	64.646	129.617	64.971	65.17	8.69
30.0	90.0	129.617	178.254	48.637	48.78	8.67
35.0	90.0	0.000	56.345	56.345	56.51	10.0
35.0	90.0	56.345	113.118	56.773	56.94	10.1
35.0	90.0	113.118	169.798	56.680	56.85	10.1
40.0	90.0	0.000	64.252	64.252	64.45	11.5
40.0	90.0	64.252	129.179	64.927	65.12	11.6
40.0	70.0	129.179	179.522	50.343	50.49	11.5
45.0	60.0	0.000	47.934	47.934	48.08	12.8
45.0	60.0	47.934	96.274	48.340	48.49	12.9
45.0	60.0	96.274	144.772	48.498	48.64	13.0
50.0	60.0	0.000	53.432	53.432	53.59	14.3
50.0	60.0	53.432	107.078	53.646	53.81	14.3
50.0	60.0	107.078	160.765	53.687	53.85	14.4
53.5	60.0	0.000	56.842	56.842	57.01	15.2
53.5	60.0	56.842	115.263	58.421	58.60	15.6
53.5	60.0	115.263	172.901	57.638	57.81	15.4

Table A.2. Pressure drop along lower chamber (psi).

Head Position	Apparent Flow Rate (ml/min)					
	5.0	10.0	20.0	30.0	40.0	45.0
1	0.006	0.023	0.049	0.064	0.071	0.074
2	0.006	0.023	0.068	0.084	0.095	0.100
3	0.006	0.023	0.100	0.117	0.125	0.130
4	0.006	0.023	0.118	0.147	0.157	0.163
5	0.006	0.023	0.130	0.171	0.187	0.193

Table A.3. Pre-conditioning *in situ* membrane permeability determination.

Apparent Flow (ml/min)	Head Position	Pressure					Permeate Flow Rate (g/min)	Permeate Flow Rate (ml/s)
		Zero Flow (psi)	Average (psi)	Loss (psi)	Corrected (psi)	Corrected (dyne/cm^2)		
5.0	5	0.125	1.091	0.006	0.963	6.64E+04	2.90E-03	4.86E-05
10.0	5	0.125	1.374	0.023	1.237	8.53E+04	3.58E-03	6.01E-05
20.0	5	0.125	1.870	0.130	1.680	1.16E+05	4.11E-03	6.89E-05
30.0	5	0.125	2.575	0.171	2.365	1.63E+05	5.92E-03	9.93E-05
45.0	5	0.125	3.643	0.193	3.422	2.36E+05	7.80E-03	1.31E-04
5.0	4	0.120	1.088	0.006	0.965	6.65E+04	2.07E-03	3.47E-05
10.0	4	0.120	1.379	0.023	1.248	8.60E+04	3.08E-03	5.16E-05
20.0	4	0.120	1.869	0.118	1.690	1.17E+05	3.73E-03	6.25E-05
30.0	4	0.120	2.579	0.147	2.386	1.64E+05	5.55E-03	9.31E-05
45.0	4	0.120	3.246	0.163	3.044	2.10E+05	6.71E-03	1.13E-04
5.0	2	0.120	0.902	0.006	0.779	5.37E+04	1.56E-03	2.62E-05
10.0	2	0.120	1.223	0.023	1.091	7.53E+04	2.34E-03	3.93E-05
20.0	2	0.120	1.917	0.068	1.763	1.22E+05	3.66E-03	6.14E-05
30.0	2	0.120	1.940	0.084	1.778	1.23E+05	4.00E-03	6.70E-05
45.0	2	0.120	1.964	0.100	1.794	1.24E+05	4.13E-03	6.93E-05
5.0	1	0.124	0.898	0.006	0.771	5.31E+04	1.65E-03	2.77E-05
10.0	1	0.124	1.232	0.023	1.096	7.56E+04	2.32E-03	3.89E-05
20.0	1	0.124	1.272	0.049	1.123	7.74E+04	2.22E-03	3.72E-05
45.0	1	0.124	1.250	0.074	1.089	7.51E+04	2.76E-03	4.62E-05
0.0	0	0.122	0.122	0.000	0.000	0.00E+00	0.00E+00	0.00E+00

Table A.4. Post-conditioning *in situ* membrane permeability determination.

Apparent Flow (ml/min)	Head Position	Pressure					Permeate Flow Rate (g/min)	Permeate Flow Rate (ml/s)
		Zero Flow (psi)	Average (psi)	Loss (psi)	Corrected (psi)	Corrected (dyne/cm^2)		
40.0	5	0.114	4.024	0.187	3.816	2.63E+05	8.62E-03	1.45E-04
5.0	4	0.105	3.574	0.006	3.466	2.39E+05	7.90E-03	1.32E-04
40.0	4	0.119	3.361	0.157	3.164	2.18E+05	7.36E-03	1.23E-04
40.0	3	0.119	2.726	0.125	2.544	1.75E+05	6.13E-03	1.03E-04
40.0	2	0.116	2.109	0.095	1.945	1.34E+05	4.44E-03	7.45E-05
40.0	1	0.118	1.494	0.071	1.341	9.24E+04	3.09E-03	5.19E-05
0.0	0	0.116	0.116	0.000	0.000	0.00E+00	0.00E+00	0.00E+00

Table A.5. BSA standards.

Sample Name	Chromatogram Peak Area (μV·s)				BSA Concentration (g/ml)
	1	2	3	Average	
1a	4478684	4415072	4455362	4449706	2.49E-02
1b	4510067	4557270	4836194	4634510	2.49E-02
1c	4528584	4511551	4507834	4515990	2.49E-02
2a	2205683	2189931	2193077	2196230	1.25E-02
2b	2224324	2219901	2225182	2223136	1.25E-02
2c	2225979	2199249	2211248	2212159	1.25E-02
3a	1811181	1833010	1820253	1821481	9.98E-03
3b	1796398	1814790	1825163	1812117	9.98E-03
3c	1820525	1826506	1807669	1818233	9.98E-03
4a	1119552	1108455	1113233	1113747	6.24E-03
4b	1128443	1131599	1133664	1131235	6.24E-03
4c	1128111	1120243	1126607	1124987	6.24E-03
5a	857844	863171	853771	858262	4.99E-03
5b	913989	898299	916893	909727	4.99E-03
5c	910465	921368	919909	917247	4.99E-03
6a	546889	548712	531023	542208	3.12E-03
6b	572232	569077	555621	565643	3.12E-03
6c	557894	560033	566582	561503	3.12E-03
7a	431492	443957	443035	439495	2.49E-03
7b	457854	438817	444227	446966	2.49E-03
7c	457964	438788	453324	450025	2.49E-03
8a	217700	208780	217005	214495	1.25E-03
8b	221033	219016	223614	221221	1.25E-03
8c	211509	213371	217841	214240	1.25E-03
9a	107306	108365	113778	109816	6.24E-04
9b	110275	112812	102617	108568	6.24E-04
9c	104812	111843	105347	107334	6.24E-04
10a	58696	53812	51834	54781	3.12E-04
10b	53830	52227	60176	55411	3.12E-04
10c	49086	54529	53272	52296	3.12E-04
11a	26585	22048	25905	24846	1.56E-04
11b	31375	28696	22292	27454	1.56E-04
11c	28298	23077	22342	24572	1.56E-04

Table A.6. 3 day BSA polarization experiments.†

Run Number	Sample Name	Distance (cm)	Chromatogram Peak Area (μV·s)			Concentration (g/ml)
			1	2	Average	
1	0 h	---	2702238	2690360	2696299	1.49E-02
	Port 1	6.68	2690970	2679891	2685431	1.48E-02
	Port 2	24.92	2682889	2712651	2697770	1.49E-02
	Port 3	38.60	2818066	2810367	2814217	1.56E-02
	Port 4	47.76	2790067	2794929	2792498	1.54E-02
	Port 5	53.06	2853766	2867857	2860812	1.58E-02
	Port 6	57.56	2666241	2666621	2666431	1.47E-02
2	0 h	---	2704462	2691403	2697933	1.49E-02
	Port 1	6.68	2588428	2571310	2579869	1.43E-02
	Port 2	24.92	2714860	2729184	2722022	1.50E-02
	Port 3	38.60	2703689	2699281	2701485	1.49E-02
	Port 4	47.76	2736109	2747669	2741889	1.52E-02
	Port 5	53.06	2791472	2764752	2778112	1.54E-02
	Port 6	57.56	2681478	2690439	2685959	1.48E-02
3	0 h	---	2687849	2687860	2687855	1.49E-02
	Port 1	6.68	2613584	2653376	2633480	1.46E-02
	Port 2	24.92	2630428	2638300	2634364	1.46E-02
	Port 3	38.60	2742507	2760776	2751642	1.52E-02
	Port 4	47.76	2831782	2817342	2824562	1.56E-02
	Port 5	53.06	2848430	2870742	2859586	1.58E-02
	Port 6	57.56	2742507	2760776	2751642	1.52E-02

† Initial BSA concentration = 1.49 %, average velocity = 10.0 cm/s, horizontal orientation

Table A.7. 7 day BSA polarization experiments.†

Run Number	Sample Name	Distance (cm)	Chromatogram Peak Area (μV·s)			Concentration (g/ml)
			1	2	Average	
1	0 h	---	179052	177754	178403	9.86E-04
	Port 1	6.68	130671	132074	131373	7.26E-04
	Port 2	24.92	173319	175518	174419	9.64E-04
	Port 3	38.60	181773	178489	180131	9.96E-04
	Port 4	47.76	194856	189746	192301	1.06E-03
	Port 5	53.06	201728	209162	205445	1.14E-03
	Port 6	57.56	197627	200288	198958	1.10E-03
2	0 h	---	181510	176714	179112	9.90E-04
	Port 1	6.68	137992	138816	138404	7.65E-04
	Port 2	24.92	169535	169733	169634	9.38E-04
	Port 3	38.60	181760	187523	184642	1.02E-03
	Port 4	47.76	196854	198839	197847	1.09E-03
	Port 5	53.06	221803	210695	216249	1.20E-03
	Port 6	57.56	215052	206277	210665	1.16E-03
3	0 h	---	171796	187662	179729	9.93E-04
	Port 1	6.68	142119	144074	143097	7.91E-04
	Port 2	24.92	165973	177020	171497	9.48E-04
	Port 3	38.60	176817	179403	178110	9.84E-04
	Port 4	47.76	192498	201326	196912	1.09E-03
	Port 5	53.06	218647	218677	218662	1.21E-03
	Port 6	57.56	205153	208113	206633	1.14E-03

† Initial BSA concentration = 0.099 %, average velocity = 15.0 cm/s, horizontal orientation

Table A.8. 9 day BSA polarization experiment.†

Run Number	Sample Name	Distance (cm)	Chromatogram Peak Area (μV·s)			Concentration (g/ml)
			1	2	Average	
1	0 h	---	177787	178668	178228	9.85E-04
	Port 1	6.68	155152	159674	157413	1.57E+05
	Port 2	24.92	176289	181309	178799	1.78E+05
	Port 3	38.60	181845	186120	183983	1.83E+05
	Port 4	47.76	195351	194253	194802	1.94E+05
	Port 5	53.06	199958	207186	203572	2.02E+05
	Port 6	57.56	156845	159450	158148	1.57E+05

† Initial BSA concentration = 0.099 %, average velocity = 15.1 cm/s, vertical orientation

Appendix B

Sample Calculations

B.1. Pump Calibration Curve

A pump calibration curve is constructed by measuring the fluid mass output over time. For example, the following data were obtained with the pump set at 5.0 ml/min:

Initial mass	= 26.334 g
Final mass	= 49.754 g
Dispensed mass	= 49.754 g - 26.334 g = 23.420 g
Density of water at 25°C	= 0.997045 g/ml
Dispensed volume	= 23.420 g ÷ 0.997045 g/ml = 23.489 ml
Time	= 300.0 s
Channel height	= 0.25 cm
Channel width	= 0.25 cm
Average fluid velocity:	= 23.489 ml ÷ (300.0 s × 0.25 cm × 0.25 cm)
	= 1.25 cm/s

Linear regression of average channel velocities, v, versus apparent flow rates, Q_{app}, gives the required calibration curve:

$$v = 0.291 Q_{app} - 0.136 \tag{B.1.1}$$

with an r^2 of 0.9997 and a standard error of 0.0784.

B.2. *In Situ* Membrane Permeability Determination

The first step in the calculation of the average membrane permeability consists of determining the volumetric permeate flow rate to average pressure drop ratio. The pressure reading under zero flow and zero head is recorded. Pressure drop and permeate mass measurements, under several flow and head conditions, are acquired through the Visual BASIC program, ACK.BAS. Before the data can be manipulated, stray zero mass readings (presumably due to a minor timing problem) must be filtered out with the Quick BASIC program, FILTER.BAS. The filtered data are then imported into a spreadsheet. For each flow setting and head position, the pressure drop readings in a relatively steady range (±0.02 psi) are averaged. Linear regression is carried out on permeate mass versus time data. The slope of the line obtained, less the evaporation rate, is the permeate mass flow rate. The following data were obtained for head position 5 and a flow setting of 5.0 ml/min (before membrane conditioning):

Zero flow and head pressure reading	= 0.125 psi
Average pressure drop	= 1.091 psi
Permeate mass flow rate	$= 2.90 \times 10^{-3}$ g/min
Density of water at 25°C	= 0.997045 g/ml
Permeate volumetric flow rate	$= 2.90 \times 10^{-3}$ g/min ÷ 0.997045 g/ml
	$= 4.86 \times 10^{-5}$ ml/s

The actual average pressure drop through the membrane can be approximated by assuming a linear decrease along the length of the membrane and correcting with chamber pressure loss terms (due to flow in the chambers):

Lower chamber pressure loss	= 0.006 psi
Upper chamber pressure loss	= 0.000 psi

In all cases the upper chamber pressure loss was found to be zero; this finding is consistent with the magnitude of the fluid flow through the chamber. The pressure loss term is halved to give an average loss along the length of membrane. Thus, the corrected pressure drop through the membrane is:

$$(1.091 - 0.125 - 0.006 \div 2)\ \text{psi} = 0.963\ \text{psi} = 6.64 \times 10^{4}\ \text{dyne/cm}^2$$

Next, the slope of a line drawn through the origin and permeate volumetric flow rate, Q, versus pressure drop, Δp, data is obtained by linear regression. For the cellulose acetate membrane, both pre- and post-conditioning, $Q/\Delta p$ was found to be 5.60×10^{-10} cm^4·s/g with an r^2 of 0.9831 and a standard error of 4.9×10^{-6}.

The cross-sectional area of flow, A, is simply the chamber length multiplied by the chamber width:

$$A = 60.0\ \text{cm} \times 0.25\ \text{cm} = 15\ \text{cm}^2.$$

The viscosity of water at 25°C, μ, is approximately 8.90×10^{-3} poise. Application of Darcy's law allows for the solution of the membrane permeability, L_p:

$$L_p = \frac{\mu}{A}\left(\frac{Q}{\Delta p}\right) = \frac{8.90 \times 10^{-3}}{15} \cdot 5.60 \times 10^{-10}\ \text{cm} = 3.3 \times 10^{-13}\ \text{cm}.$$

Alternatively, the Darcy permeability, κ, may be calculated with the membrane thickness, $H_m = 0.025$ cm:

$$\kappa = H_m L_p = 0.025 \times 3.3 \times 10^{-13}\ \text{cm}^2.$$

B.3. BSA Standard Curve

HPLC analysis generated BSA chromatogram peaks at approximately 3.2 min. The area under each peak is calculated with Waters Millennium software. Linear regression of BSA standard concentrations, C, versus peak areas, A_p, yielded:

$$C = 5.527 \times 10^{-9} A_p \qquad \text{(C.4.1)}$$

with an r^2 of 0.9995 and a standard error of 1.68×10^{-4}.

B.4. Sample BSA Concentrations

Sample peak areas, calculated with Waters Millennium software, are used in **equation C.4.1** to calculate the BSA concentrations of the samples. For example, the port 6 sample of run 1 of the 3 day polarization experiments gave the following peak areas:

Injection 1	2666241 μV·s
Injection 2	2666621 μV·s
Average	(2666241 + 2666621)/2 μV·s = 2666431 μV·s

The BSA concentration of this sample, then, is:

$$C = 5.527 \times 10^{-9} \times 2666431 \text{ g/ml} = 1.47 \times 10^{-2} \text{ g/ml}.$$

Appendix C

Waters HPLC System and Millennium Software

C.1. HPLC System Preparation

The following steps describe the preparation of the HPLC system:

1. The mobile phase is prepared by helium sparging at 100 ml/min for 15 min. During HPLC operation, the sparge rate is reduced to 5 ml/min.
2. The pump is primed as follows:
   i. With the 'silk' option turned off, the pump is set to 0.5 ml/min.
   ii. The metal valve lever is turned to the reference (right) side.
   iii. A plastic syringe is attached to the pump sample port.
   iv. The syringe connection manifold is turned to 'drain'.
   v. Several ml of fluid are drawn into the syringe.
   vi. The manifold is turned to 'inject' and fluid is injected into the system (the fluid should flow out of the open line steadily into a beaker).
   v. The pump flow is ramped gradually (by 1 ml/min increments) to 15 ml/min. Again, steady flow should result.
   vi. The flow rate is ramped gradually back to 0.5 ml/min and the reference valve is closed.
   vii. If at any point unsteady flow is encountered, the procedure is repeated.
3. The autosampler is set up and purged daily as follows:
   i. With the 'silk' option turned off and a carousel in the autosampler, the purge page is selected.
   ii. The purge time should be set to 2 min, with all other settings set to their defaults.
   iii. 'Start purge' is selected from the autosampler control panel. The system is purged and performs a compressibility test.

iv. If the compressed volume is greater than 2 µl, the operation is repeated. If the compressed volume is particularly large, gas is removed from the system by disconnecting the bottom nut of the syringe as it moves down. The syringe rod is then moved up and down to dislodge gas bubbles.

v. Once the purge is completed, the 'silk' option is turned on.

4. The column temperature is set (to 37°C) by pressing the following keys on the refractometer console, in order: '2nd Func', 'ext 1 °C', and 'Set Temp'. The temperature is keyed in and 'Enter' is pressed. If the refractometer is to be used, it is purged daily by pressing '2nd Func' and 'Purge'.

C.2. Data Acquisition and Analysis

Data acquisition and data analysis are conducted through Waters Millennium software. The rudiments are as follows:

1. The Millennium session manager is started under Microsoft Windows 3.1, and the user logs in.
2. The desired project is opened.
3. The 'Quick Set' button is pressed and the appropriate information is entered:

Sample Name	(variable)
Function	Inject Samples
Method Set	pda_metset_recent
Inj Vol (µl)	15
Run Time (min)	6
Other options	(default)

4. One or more samples are selected and the 'Setup Instruments' button is pressed.

5. From the 'File' pop-down menu, the 'Save As Sample Set' option is selected. The desired sample set name is entered and the 'OK' button is pressed.
6. The 'Run Tray or Sample Set' button is pressed and the 'Sample Set' option is selected.
7. Once the analysis of the sample set is completed, the 'Quick Set' window is closed.
8. From the 'View' pop-down menu, the 'Sample Sets' option is selected, and the 'Update' button is pressed.
9. The desired sample set is selected and the 'Process and Report' button is pressed.
10. Once the report generator is finished, the 'Result Sets' option is selected from the 'View' pop-down menu, and the 'Update' button is pressed again.
11. Next, the desired result set is selected and the 'Export Data' option is selected from the 'Database' pop-down menu. In the dialog box, the export method is entered (expo2) and, if desired, the file path and root are specified. The dialog box is closed by pressing the 'OK' button.
12. After the report generator has finished, the project is closed and the Millennium session manager is exited.

Appendix D

Recirculation and Associated BSA Distributions

The following figures have been assembled to show how recirculation regions and the associated BSA distributions develop in the upper channel in the inverted vertical orientation. The following conditions apply:

- membrane permeability, $L_p = 6.00 \times 10^{-11}$ cm,
- average lower channel inlet velocity, $\bar{v} = 25$ cm/s,
- initial BSA concentration, $C_0 = 0.01$ g/ml.

In the figures below, distance x is the length along the flow cell in cm and includes a 15 cm entrance section, and velocities are given in cm/s. Furthermore, the main flow direction is from left to right, with gravity acting in the opposite direction.

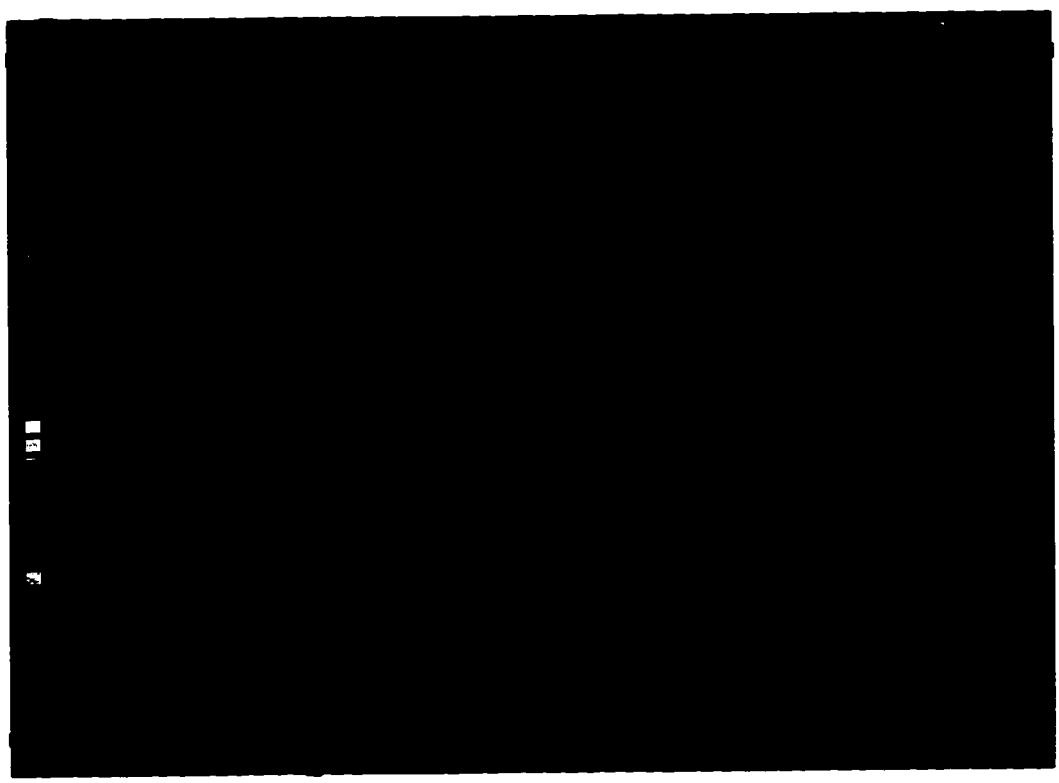

Figure D.1. Velocity vector plot at time zero.

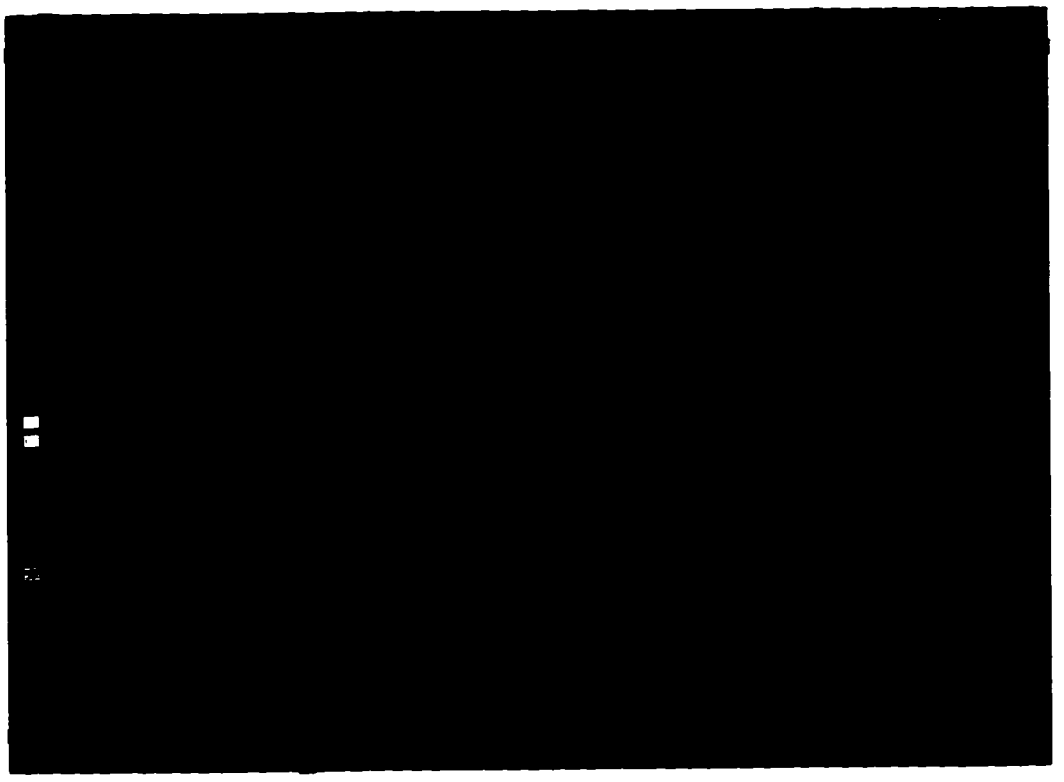

Figure D.2. Velocity vector plot at 60 s.

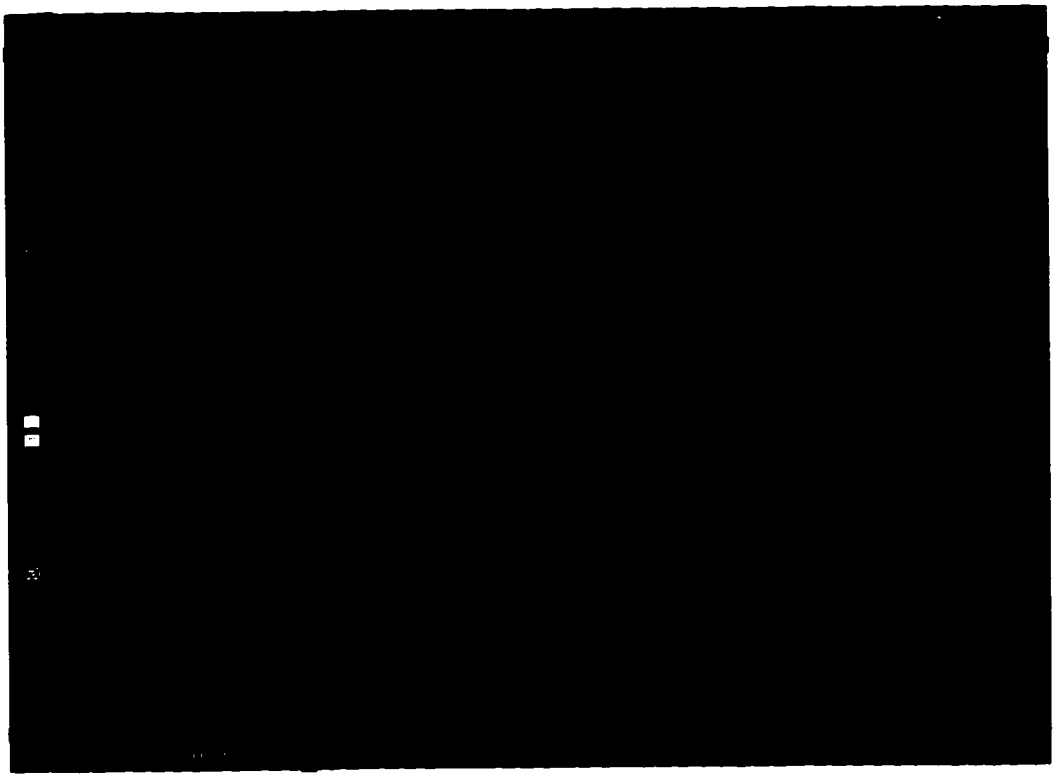

Figure D.3. Velocity vector plot at 90 s.

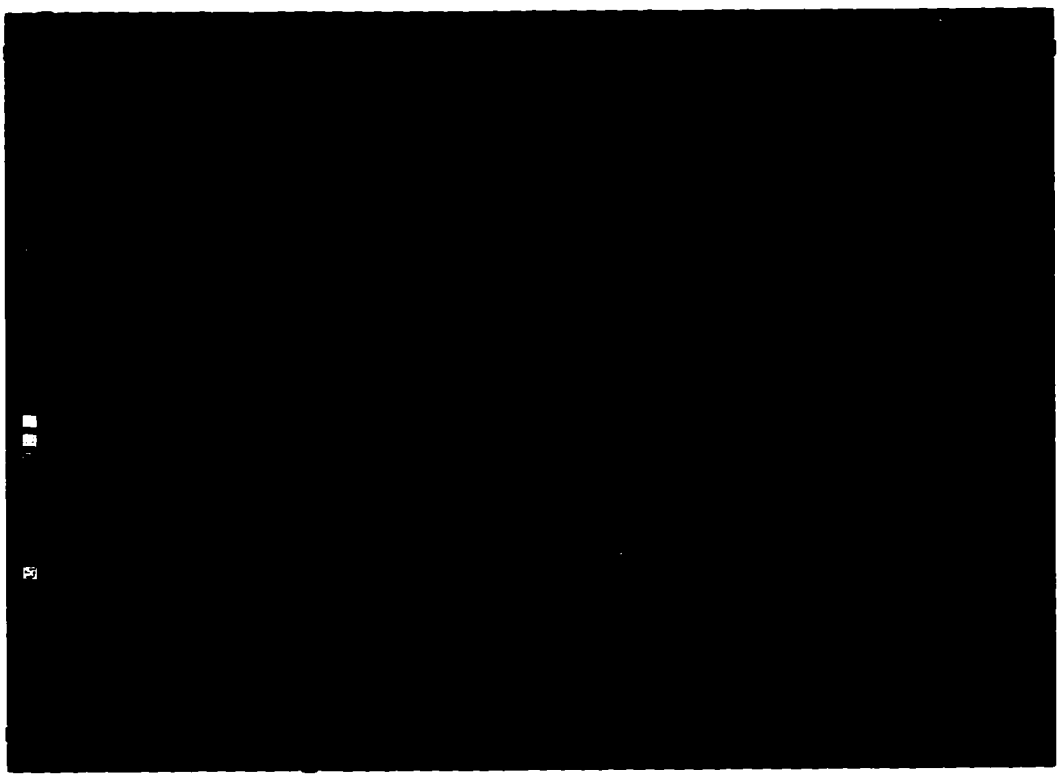

Figure D.4. Velocity vector plot at 2 min.

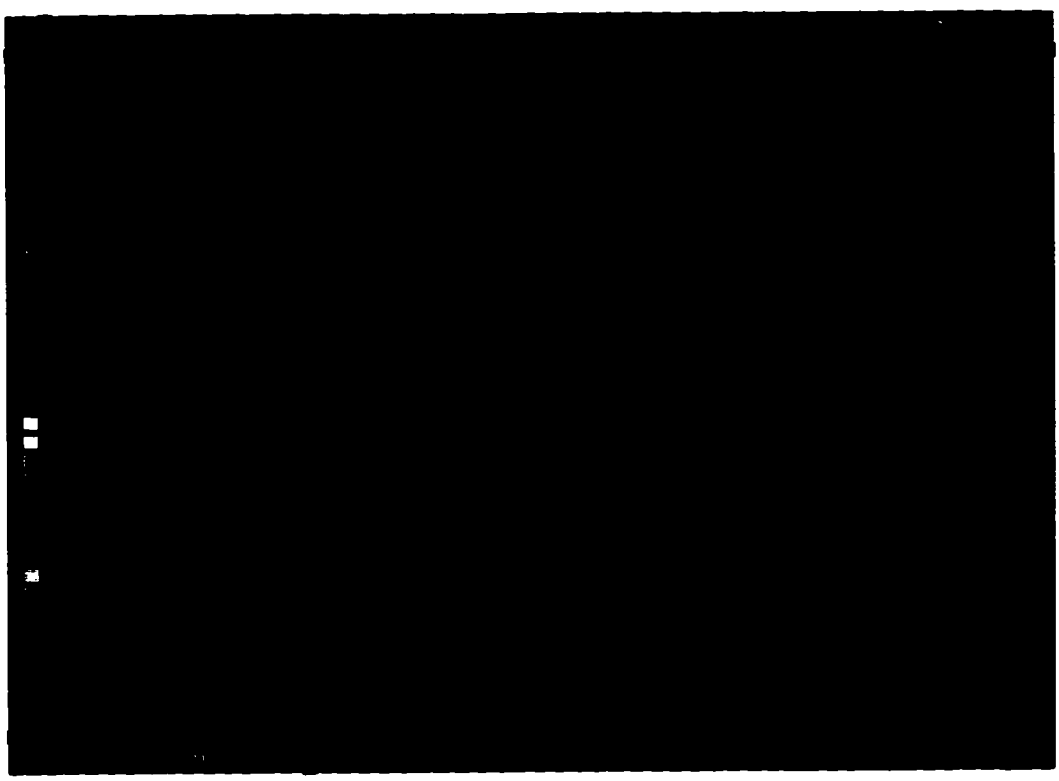

Figure D.5. Velocity vector plot at 3 min.

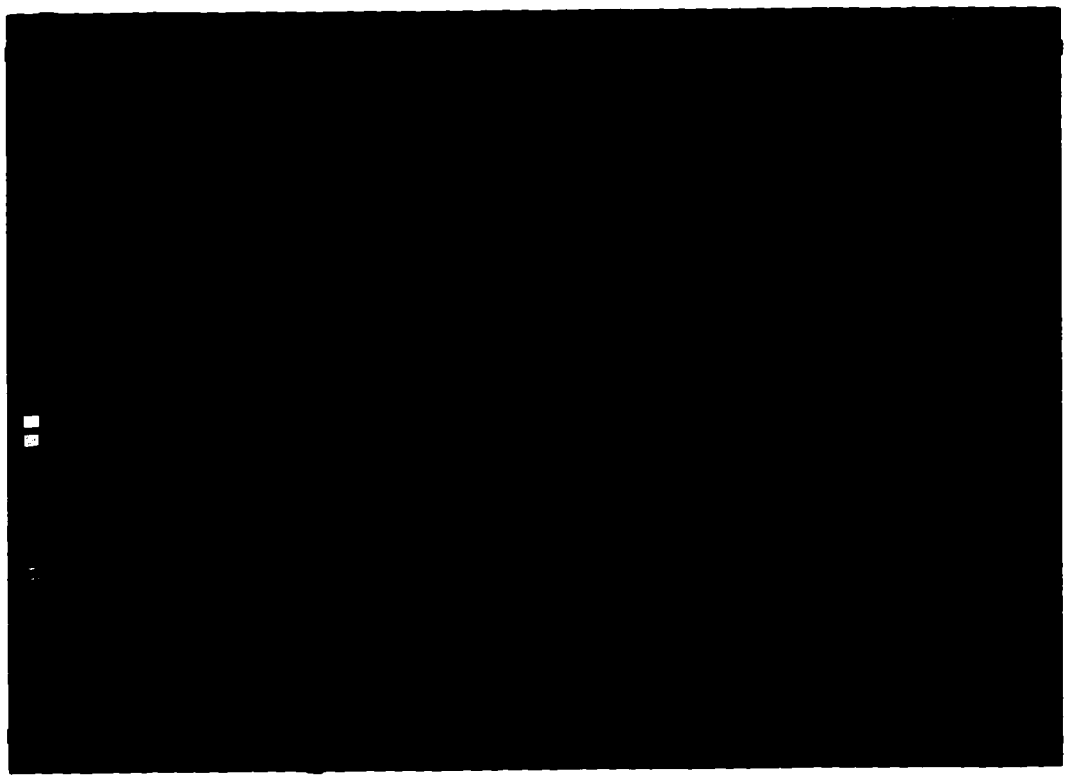

Figure D.6. Velocity vector plot at 5 min.

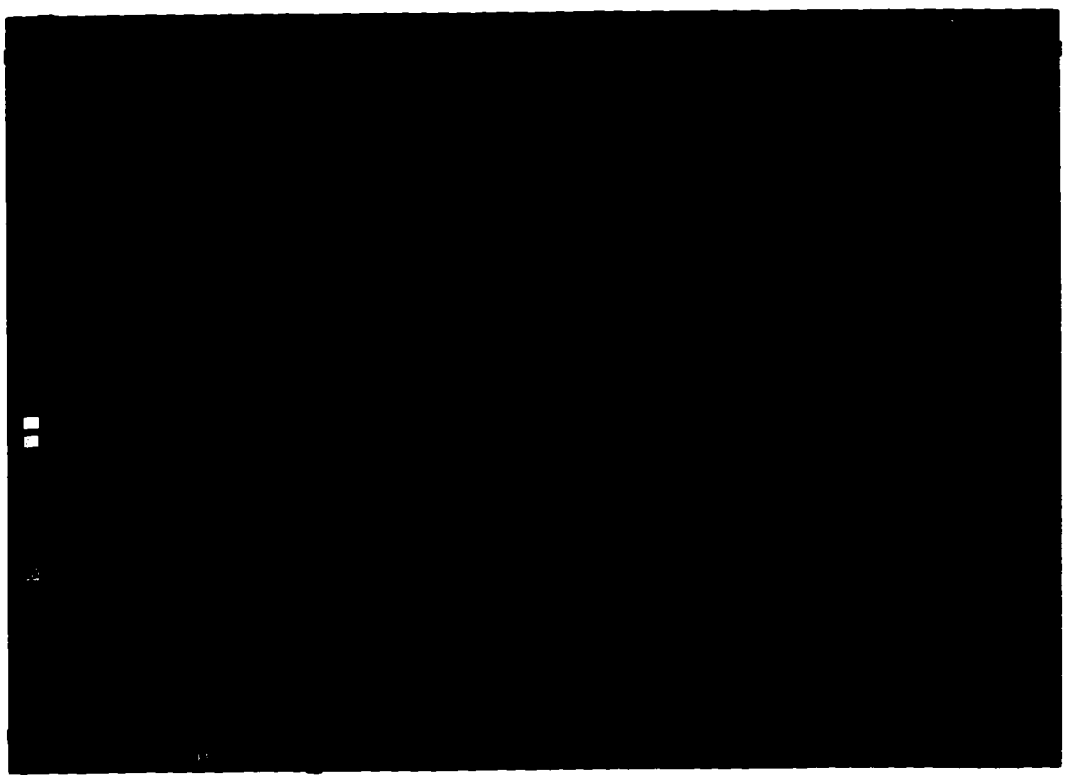

Figure D.7. Velocity vector plot at 10 min.

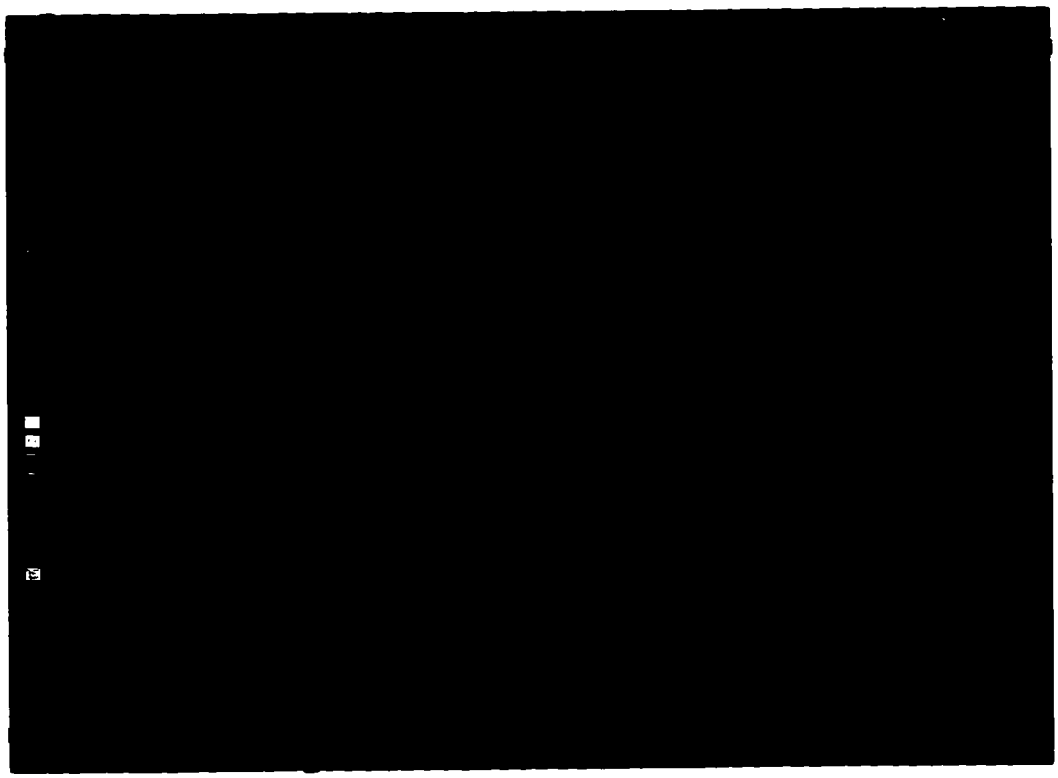

Figure D.8. Velocity vector plot at 15 min.

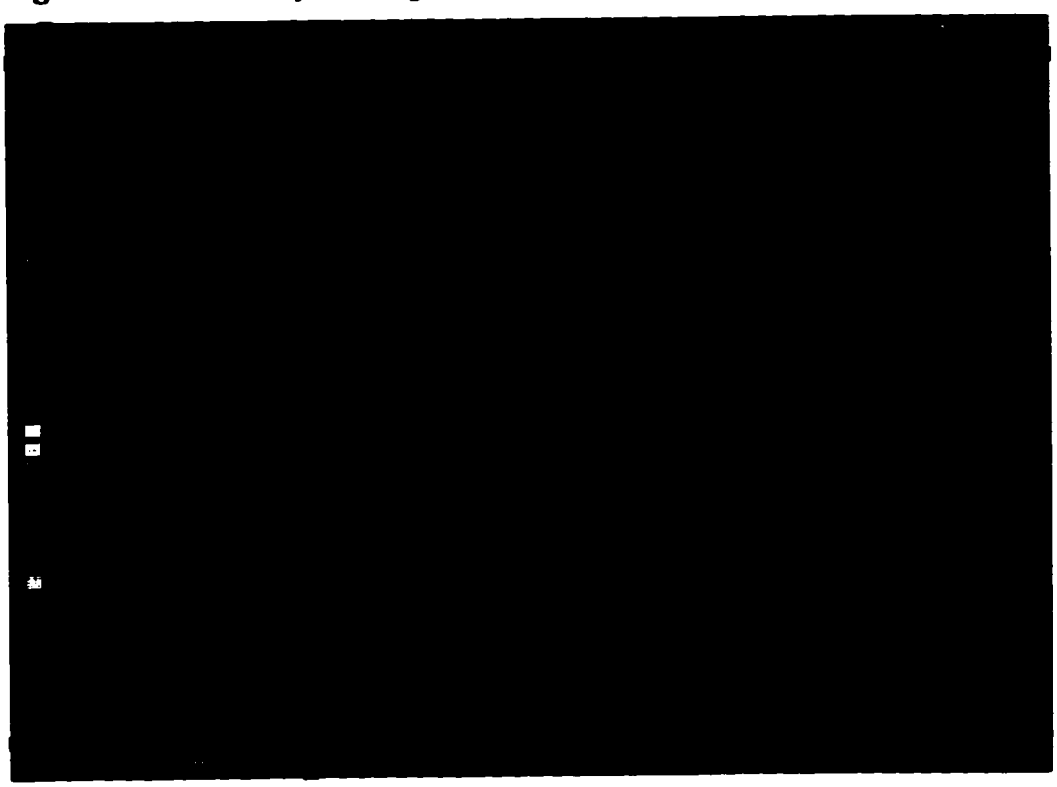

Figure D.9. Velocity vector plot at 20 min.

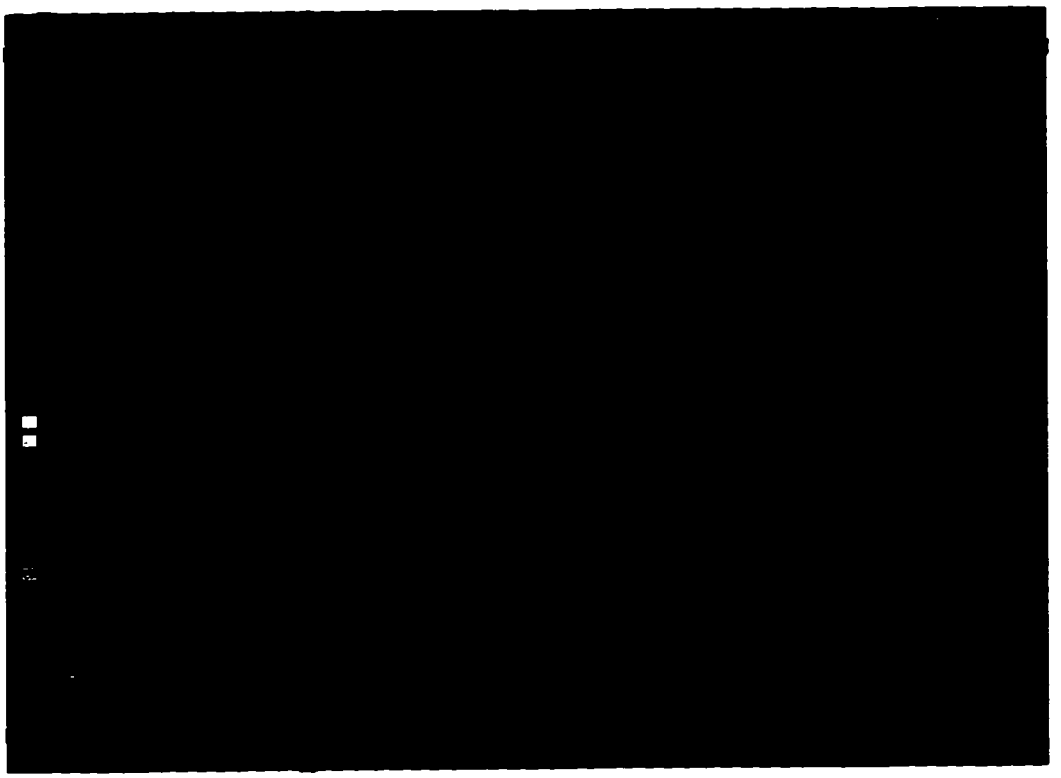

Figure D.10. Velocity vector plot at 3 h.

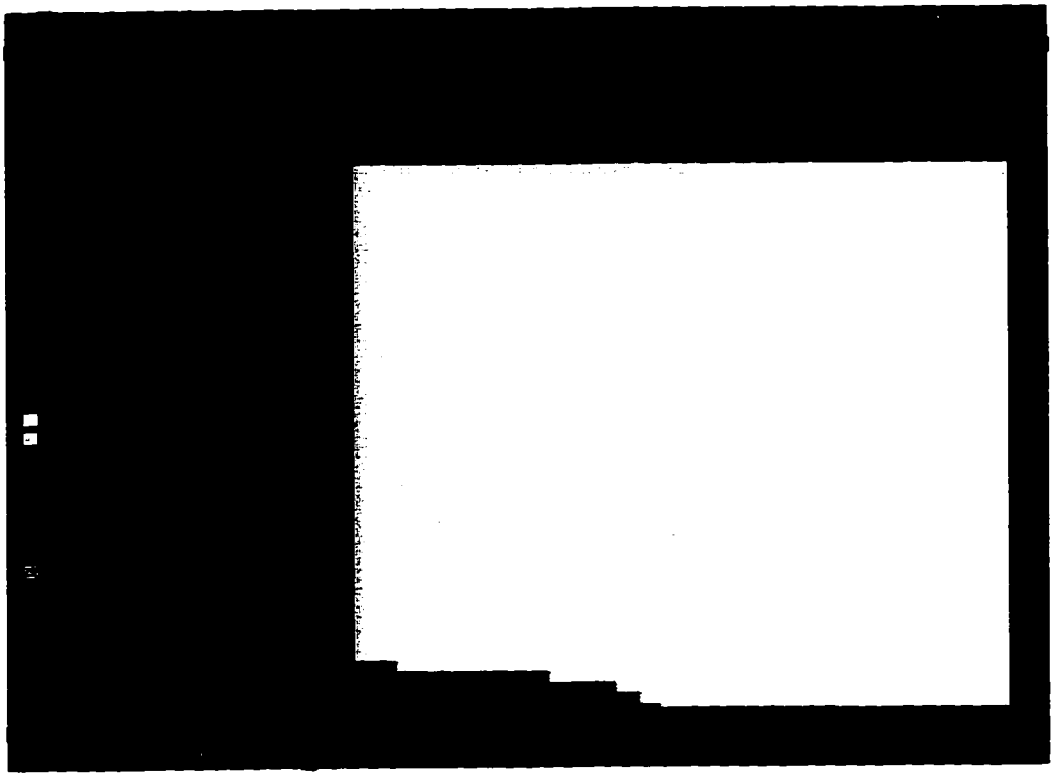

Figure D.11. BSA mass fraction distribution at 60 s.

Figure D.12. BSA mass fraction distribution at 90 s.

Figure D.13. BSA mass fraction distribution at 2 min.

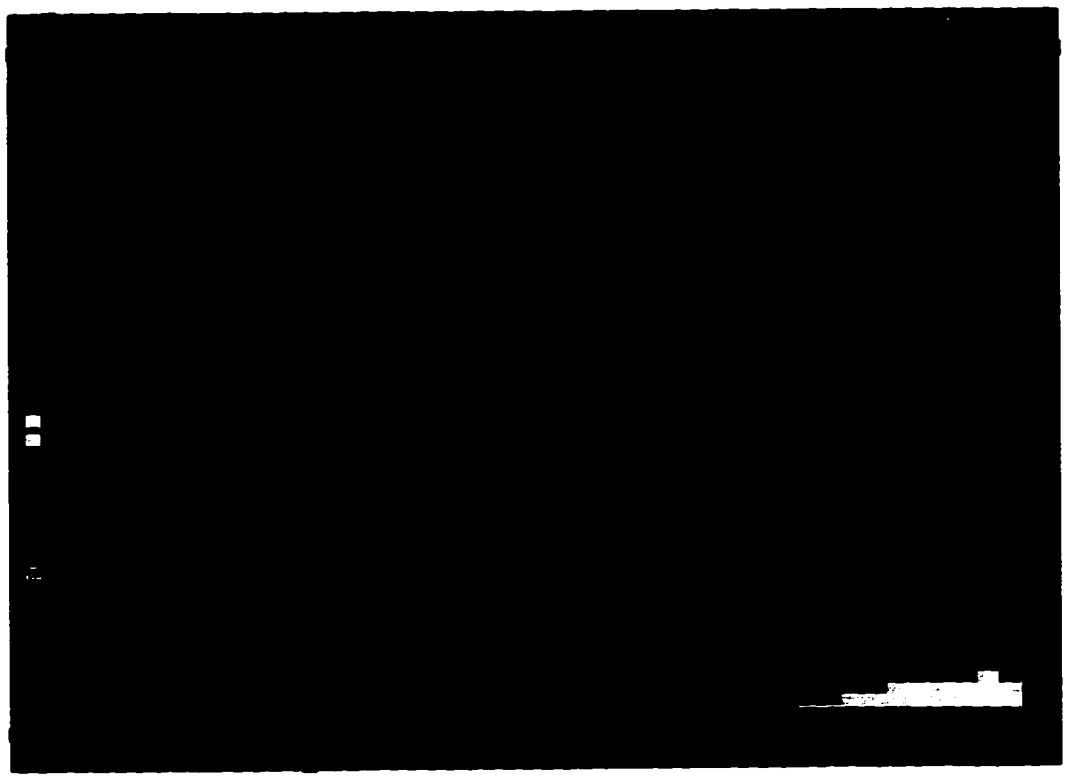

Figure D.14. BSA mass fraction distribution at 3 min.

Figure D.15. BSA mass fraction distribution at 5 min.

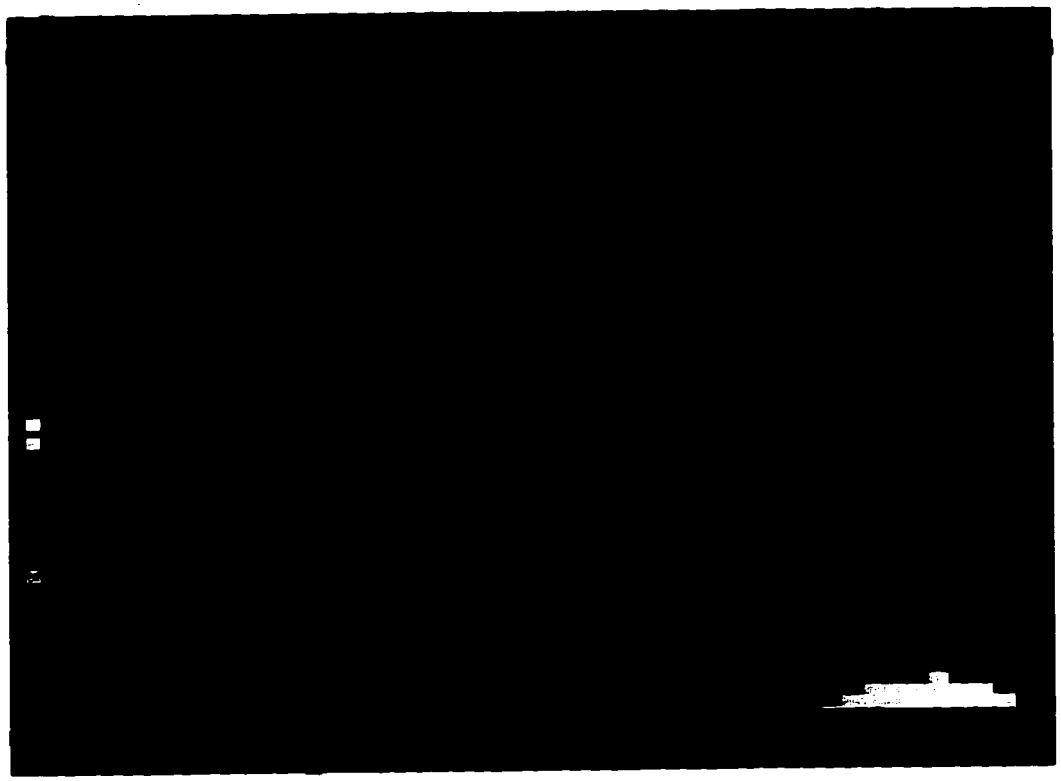

Figure D.16. BSA mass fraction distribution at 10 min.

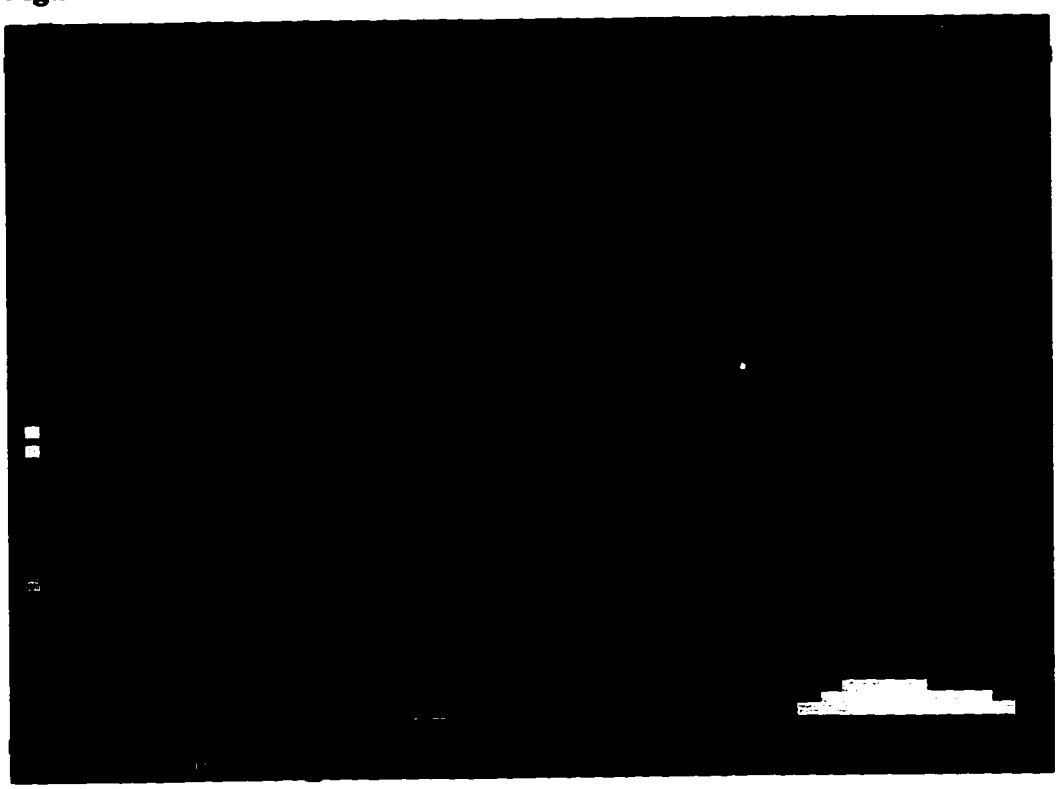

Figure D.17. BSA mass fraction distribution at 15 min.

Figure D.18. BSA mass fraction distribution at 20 min.

Figure D.19. BSA mass fraction distribution at 3 h.

Appendix E

CD ROM Contents

The contents of the CD ROM are as follows:

- Root directory: README.AHA text file that documents the contents of the CD ROM, program features, how to use them, and details of the simulation output files that are included.

- CODE directory: the FORTRAN source code, input files, compiled programs, and the DOS4GW DOS extender. To run a program, type DOS4GW [*program name*] at the DOS prompt.

- DATA directory: experimental (Excel 5 format) and numerical data (text and Excel 5 formats) presented in the thesis. To read a simulation output file into the simulator, simply copy it to the CODE directory prior to running program.

- SEMINAR directory: PowerPoint presentation files.

- SYNOPSIS directory: PowerPoint presentation file.

- THESIS directory: Thesis text (Word 6 format) and graphic files.